Optimization of Ionic Conductivity in Doped Ceria Using Density Functional Theory and Kinetic Lattice Monte Carlo

by

Shahriar Anwar

A Dissertation Presented in Partial Fulfillment
of the Requirements for the Degree
Doctor of Philosophy

Approved April 2011 by the
Graduate Supervisory Committee:

James B. Adams, Chair
Peter Crozier
Stephen Krause

ARIZONA STATE UNIVERSITY

May 2011

ABSTRACT

Fuel cells, particularly solid oxide fuel cells (SOFC), are important for the future of greener and more efficient energy sources. Although SOFCs have been in existence for over fifty years, they have not been deployed extensively because they need to be operated at a high temperature ($\sim 1000^{\circ}$C), are expensive, and have slow response to changes in energy demands. One important need for commercialization of SOFCs is a lowering of their operating temperature, which requires an electrolyte that can operate at lower temperatures. Doped ceria is one such candidate. For this dissertation work I have studied different types of doped ceria to understand the mechanism of oxygen vacancy diffusion through the bulk. Doped ceria is important because they have high ionic conductivities thus making them attractive candidates for the electrolytes of solid oxide fuel cells. In particular, I have studied how the ionic conductivities are improved in these doped materials by studying the oxygen-vacancy formations and migrations.

In this dissertation I describe the application of density functional theory (DFT) and Kinetic Lattice Monte Carlo (KLMC) simulations to calculate the vacancy diffusion and ionic conductivities in doped ceria. The dopants used are praseodymium (Pr), gadolinium (Gd), and neodymium (Nd), all belonging to the lanthanide series. The activation energies for vacancy migration between different nearest neighbor (relative to the dopant) positions were calculated using the commercial DFT code VASP (Vienna Ab-initio Simulation Package). These activation energies were then used as inputs to the KLMC code that I co-developed. The KLMC code was run for different temperatures (673 K to 1073 K) and for different dopant concentrations (0 to 40%). These simulations have resulted in the prediction of dopant concentrations for maximum ionic conductivity at a given temperature.

This dissertation is dedicated to my wife,

Shahriar Alam,

and to my daughter,

Urusa Shahriar Alaan,

for their unconditional love and support.

ACKNOWLEDGEMENTS

Over the years, many people have helped and guide me through my doctoral study at the Materials Science and Engineering program at Arizona State University (ASU).

I would like to express my wholehearted gratitude to my advisor, Dr. James B. Adams, for giving me the opportunity to pursue my studies under his supervision. He has been a great teacher and mentor to me and has always been very supportive and encouraging even when I may have taxed his patience. I couldn't have concluded my doctoral studies without his help and support.

I also thank my committee members Dr. Steve Krause and Dr. Peter Crozier for their help, discussion, and encouragement during the course of my doctoral study.

I gratefully thank Dr. Pratik Dholabhai for helpful collaboration with my research, and for many intriguing suggestions and discussions. I look forward to a life long friendship and professional relationship.

I also thank other faculty and staff of the ASU Materials Engineering program and SEMTE, and particularly Ms. Yolanda Ruiz Murphy for her support and assistance during the course of my study.

I thank my parents for their support and prayers and wish my father was here to savor the culmination of my studies.

Finally, but most importantly, I would like to thank my wife, Shahriar Alam, and my daughter, Urusa Shahriar Alaan, for their continuous love and encouragement. I particularly thank my wife for her understanding, guidance, patience, sacrifice, and unending support, and for always having faith in me.

TABLE OF CONTENTS

LIST OF TABLES

LIST OF FIGURES

Chapter 1

INTRODUCTION

1.1 Why this Topic is Important

With the accelerating demands of energy usage by developing countries such as China and India, in addition to those of the developed countries, there is a renewed impetus to find cleaner and more efficient engines that may lead to reduction in our dependence on fossil fuel. Fuel cells, because of their higher efficiencies, much quieter technology, and significantly lower pollution production, are promising replacements for the internal combustion engines, if their cost can be lowered. Fuel cells, particularly solid oxide fuel cells (SOFCs) are viewed as important to the future of greener and more efficient energy sources. Although SOFCs have been in existence for decades, they have not been deployed extensively because they need to be operated at high temperatures ($> 900^{\circ}$C), are expensive, and have slow response to changes in energy demands.

One of the important components of a fuel cell is the electrolyte. Ideal electrolytes should have high ionic conductivity, but low electronic conductivity. Ceria (CeO_2) is one of the oxides with a cubic fluorite structure that is a good solid electrolyte when it is doped with cations of lower valence than the host cations [1]. The doped ceria has a high ionic conductivity thus making it an attractive electrolyte for solid oxide fuel cells. In the electrolyte of a solid oxide fuel cell, whose schematics are shown in Fig. 1.2 on page 6, the current is carried by oxygen ions that are transported by oxygen vacancies. These vacancies are introduced in order to compensate for the lower charge of the dopant cations. The ionic conductivity in ceria depends on the oxygen-vacancy formation and migration properties.

Although solid electrolytes are critical in the SOFC, optimization of such materials are often done by trial and error. The choice of the dopants (or co-dopants) and their optimal concentrations to maximize the ionic conductivity can however be systematically searched using computer simulation. Density functional theory (DFT) calculations can be utilized to study oxygen diffusion in doped ceria. In our study, we have determined the

oxygen vacancy migration in ceria and the different diffusion pathways in doped ceria via a vacancy hopping mechanism by calculating the activation energies using DFT. We then used these rates as inputs to a kinetic lattice Monte Carlo (KLMC) code that we developed in order to rigorously determine the ionic conductivity as a function of temperature and dopant concentration. The thrust of this research is not only to find the optimal type of dopants and the best dopant concentrations that maximize ionic conductivity but also to understand how the choice of dopant improves the ionic conductivity.

1.2 Fuel Cell Technology

Fuel cells were first invented in the middle of the nineteenth century by Sir William Grove and are one of the oldest known electrical energy conversion technologies. However, they did not get wide acceptance in use, and lagged behind steam and internal combustion engines due to economic factors, materials problems, and inadequacies in their operational cost and durability [2]. Currently there are different types of fuel cells and they are, a) the alkaline fuel cell (AFC) that was used in the Apollo space program, b) the proton exchange membrane fuel cell (PEMFC), c) the direct methanol fuel cell (DMFC), d) the phosphoric acid fuel cell (PAFC), e) the molten carbonate fuel cell (MCFC), and f) the solid oxide fuel cell (SOFC). The main components of all the fuel cells are an electrolyte sandwiched between an anode and a cathode, similar to the schematics shown in Fig. 1.1 on page 3, with catalytic layers between the electrodes and the electrolyte. The MCFC and SOFC operate at high enough temperatures that the catalytic activity of the electrode materials are sufficient to forgo the need of the catalyst layers. The differences between the various types of fuel cells, due to the choices of the electrode and electrolyte materials are a) the operating temperature, b) the fuel and gases fed to the electrodes, c) the catalysts, d) the by-products of the reactions, and e) the reactions that take place. The AFC, PEMFC, and PAFC require relatively pure hydrogen gas for their operation. This hydrogen has to be externally generated from fossil fuels or from other sources to be fed to the anode of these types of fuel cells. This not only increases the complexity of these systems but also reduces their efficiencies. However, the higher operating temperatures of the MCFC and SOFC mean that

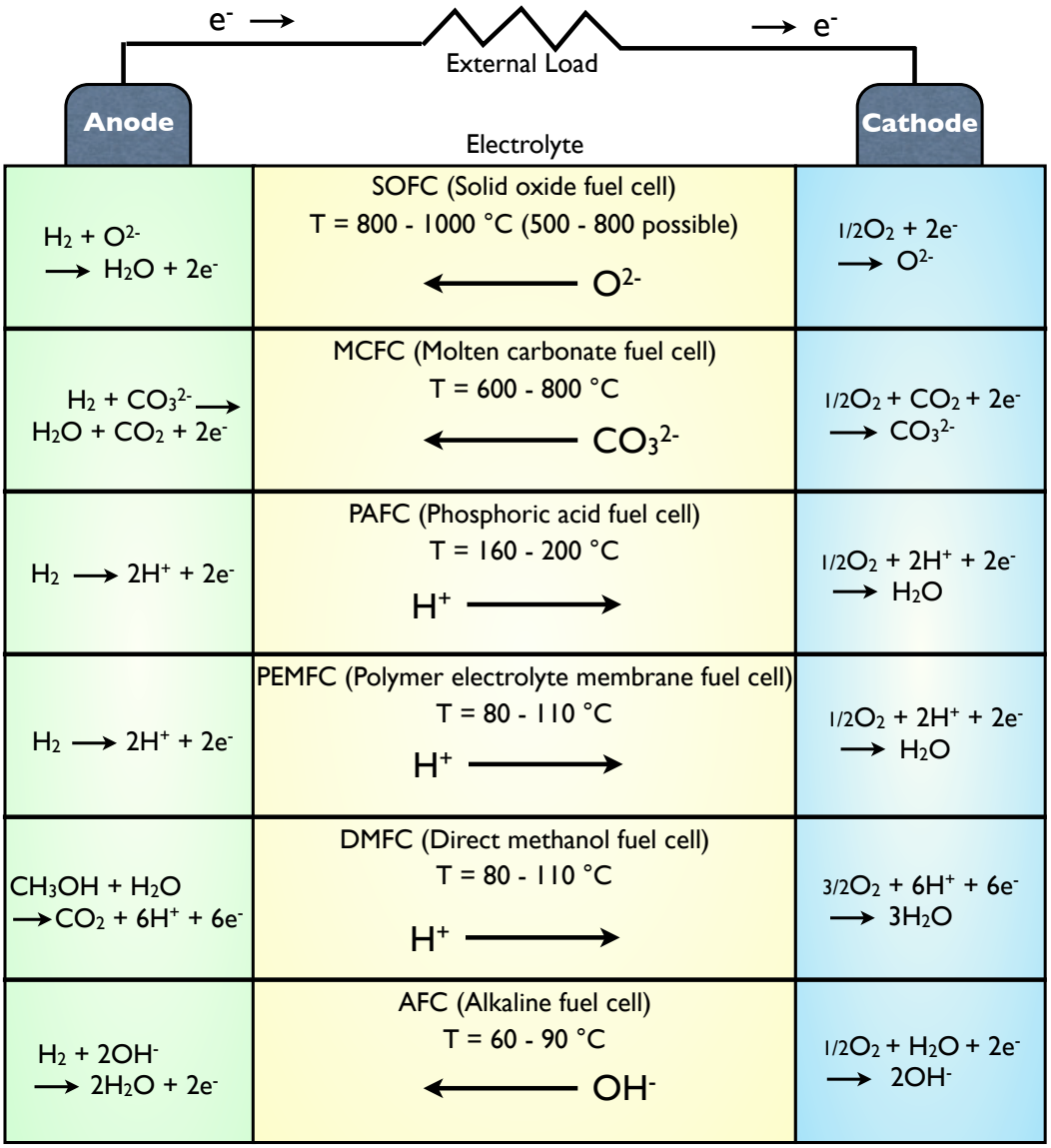

Figure 1.1: Schematics and overview of the different types of fuel cells, with operating temperatures, along with the anodic and cathodic reactions. The ion types and their direction of transfer are also indicated. The electrons liberated during the anodic reaction travel along an external path, driving an external load, to arrive at the cathode to participate in the cathodic reaction. Excepting for the SOFC and the MCFC all the other types of fuel cells also have a catalytic layer between the anode and the electrolyte and another layer between the cathode and the electrolyte; these layers are not shown. The MCFC and SOFC operate at high enough temperatures such that the catalytic activity of the electrode materials are sufficient to forgo the need of the catalyst layers. It should also be noted that in addition to the electricity being generated another by-product of these reactions is heat that can be recycled to provide heating or to generate electricity. Adapted from Steele and Heinzel [3] with data from Carrette, Friedrich, and Stimming [2].

they can electrochemically oxidize H_2 and CO at the anode. This, combined with integrated reformers, can push MCFC and SOFC to efficiencies of $\sim 50\%$ [4].

The AFC has the advantage of being simple in design but has the disadvantage of not being CO_2 tolerant. The PEMFC has the advantage of having a fast start-up time and there being no leaking of electrolytes. The DMFC is simple to operate and usually uses a 3% mixture of methanol and water that is easy to store and transport. However, both the PEMFC and DMFC have the disadvantage that they are not CO tolerant and since their membranes have to be maintained at certain humidity levels they have water management issues. The DMFC also has issues with methanol cross-over. The CO poisoning issue is alleviated in the PAFC due to its higher operating temperature but is plagued with liquid electrolyte leakage and lower phosphoric acid conductivity. It is possible to achieve high efficiency with the MCFC, particularly when combined with gas turbine. It is also possible to combine internal reforming with the molten carbonate fuel cell and it is CO and CO_2 tolerant. The major disadvantages of the MCFCs are that they need a long start-up time and electrolyte creep is possible whence the NiO cathode can creep and cause short circuit. Although the solid oxide fuel cell has a long start-up time like the MCFC, it has no electrolyte creeping problem. It too has the possibility of internal reforming and high efficiency is attainable through co-generation. However, another drawback of the SOFC is that because of the typical high operating temperature (800 - 1000 °C) materials degrade faster and conformal sealing is difficult to maintain.

Of these different types of fuel cells the solid oxide fuel cell (SOFC) (Fig. 1.2) is very promising for use in automobiles and power sources for buildings due to the following advantages of solid oxide fuel cells: a) SOFCs have high efficiency, b) they have no corrosive issues, c) they need no handling of hazardous liquid electrolytes, and d) they allow fuel flexibility by the integration of an internal reformer [5]. The most widely used electrolytes in SOFCs are ceria, and Yttria-Stabilized Zirconia (YSZ). Ceria, or cerium dioxide (CeO_2), is a material of great use and interest in solid oxide fuel cells owing to the fact that it has high oxygen ion conductivity at temperatures of ($\sim 1000\,^{\circ}$C). Using Yttria-Stabilized

Zirconia (YSZ), coupled with thin (10–15 micron) films, the operating temperature for optimal ionic conductivity may be reduced to $\sim 700\ ^{\circ}\mathrm{C}$ [3]. Technical difficulties preclude further reduction in the film thickness. One advantage of such very high operating temperature is that relatively impure fuels may be used. However, it also means the efficiency is reduced, more expensive materials are needed, and the response time to energy demand is slow (because it takes time to heat the system up to the required operating temperatures of $\approx$ 800-1000 °C). These points make pure ceria and YSZ unfeasible in automotive applications. It is imperative that we find SOFC electrolytes that can be operated at much lower temperatures.

One way to attain lower operating temperatures is to use doped ceria. In doped ceria oxygen vacancies are formed relatively easily facilitating ionic diffusion. By substituting a fraction of the ceria with dopants, such as those from the rare earth lanthanide series (Fig. 4.5 on page 62), we can introduce oxygen vacancies in the crystal without adding charge carriers. This results in increased ionic conductivity in the SOFC and results in a better electrolyte. As Steele and Heinzel [3] point out, doped ceria based electrolytes should lower the operating temperature of an SOFC to around 500 °C. At elevated temperatures, Ce^{4+} ions can be reduced to Ce^{3+} under the fuel-rich conditions that exist in the anode compartment. The efficiency and performance of the fuel cells are significantly degraded by the associated increase in electronic conductivity. Thus the lowering of the temperature has the added benefit of achieving smaller electronic conduction thus attenuating the internal short circuits in the positive-electrolyte-negative (PEN) components [3]. At around 500 °C the electronic conductivity is small and can be neglected under typical operating conditions of the cell [4]. The most promising candidates for doping ceria appear to be those from the lanthanide series. However, the origin of the differences in ionic conductivity between different dopants still remain poorly understood [5]. Our goal is to find out which dopants or co-dopants are best in reducing the operating temperature, what are the optimal dopant concentrations, and to explain the process of ionic conductivity from our model.

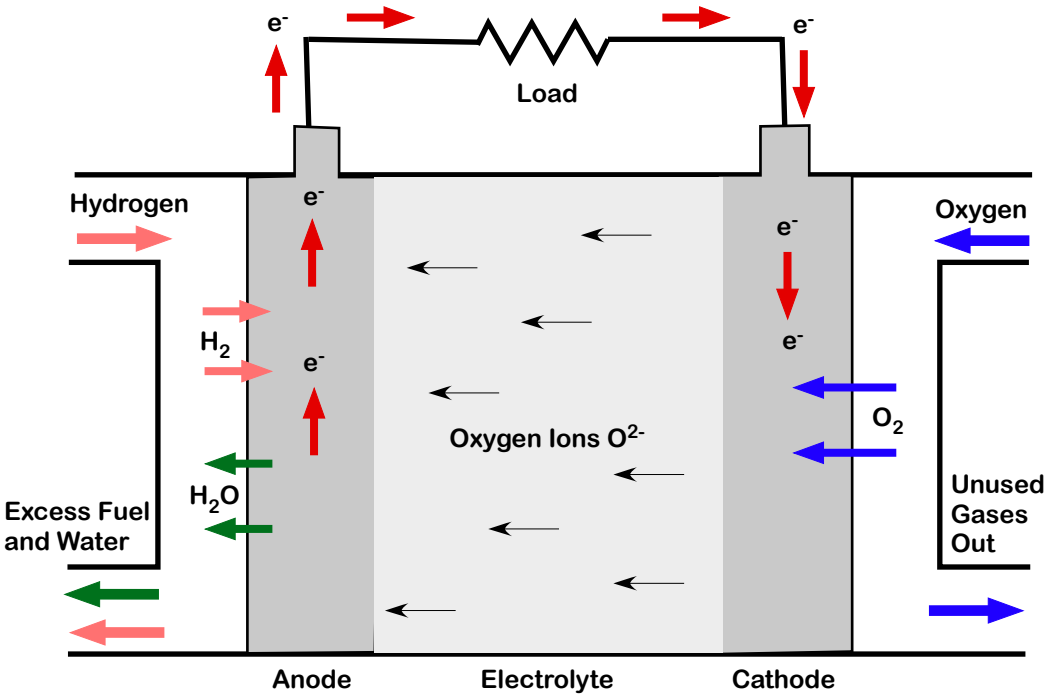

Figure 1.2: Schematics of the solid oxide fuel cell (SOFC). The charge carrier in the SOFC is the oxygen ion (O^{2-}). At the cathode, the oxygen molecules from the air are split into oxygen ions with the addition of four electrons. The oxygen ions are conducted through the electrolyte and combine with hydrogen at the anode, releasing four electrons. The electrons travel an external circuit providing electric power and producing by-product heat.

1.3 Literature Review—Experimental

Cerium dioxide (CeO_2) has found a number of applications in industry. It is critical in three-way catalysis in the removal of vehicular exhaust gases [6]. CeO_2 has also been used as a catalyst for the removal of SO_x from fluid catalytic cracking flue gases [6]. CeO_2 has also been studied and is used in the inner coating of self-cleaning ovens as an oxidizing agent. A number of recent publications [3–15] have addressed the role of ceria and doped ceria due to their importance in oxygen vacancy migration in possible automotive applications of solid oxide fuel cells (SOFC). Although not directly relevant to this study, a number of studies [16–24] have applied the density functional theory, that we used in this dissertation work, to the study of the CeO_2 surface.

Ceria (CeO_2) crystallizes in the fluorite structure. It has a face-centered cubic unit cell with space group $Fm\bar{3}m$ with $a = 5.4113$ Å. This structure can be regarded as a ccp array of cerium ions with eight oxygen ions occupying all the tetrahedral holes for a total of 12 atoms per unit cell (Fig. 1.3. In this structure each cerium cation is coordinated by eight equivalent nearest-neighbor oxygen anions and each anion is tetrahedrally coordinated by four cations. This structure may also be viewed as a simple cubic oxygen sublattice with the cerium ions occupying alternate cube centers as shown in Fig. 1.4.

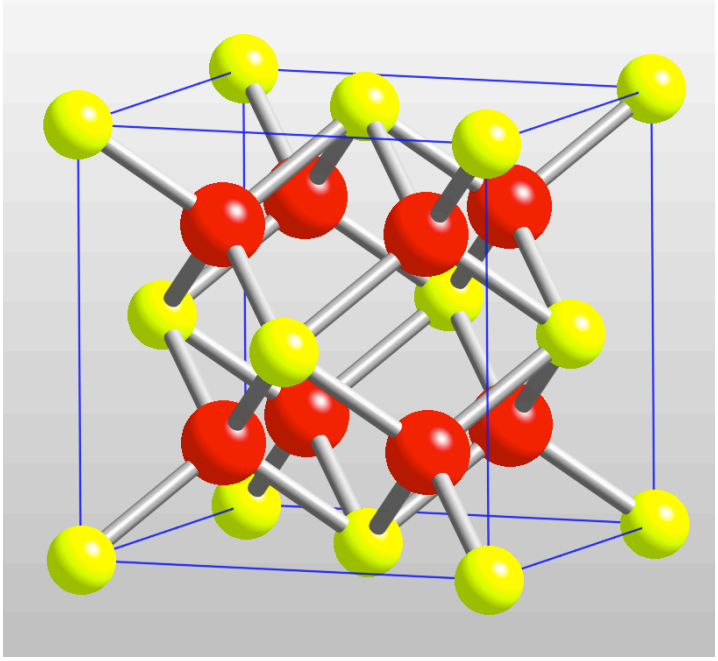

Figure 1.3: CeO_2 unit cell viewed as a ccp array of cerium atoms (yellow or light) with eight oxygen atoms (red or dark) occupying the tetrahedral sites. False ionic radii are used for clarity. Model created in CrystalMaker.

Three important properties make ceria very useful as an electrolyte in solid oxide fuel cells and as oxygen sensors. First, the open fluorite structure of CeO_2 allows the oxygen anions to migrate through the lattice with relative ease [25]. Second, CeO_2 can also show large deviations from stoichiometry under reducing conditions with little phase change. Under such conditions the Ce^{4+} ions are reduced to Ce^{3+}. Although in most material the resulting electron during the reduction process is not truly localized at a single

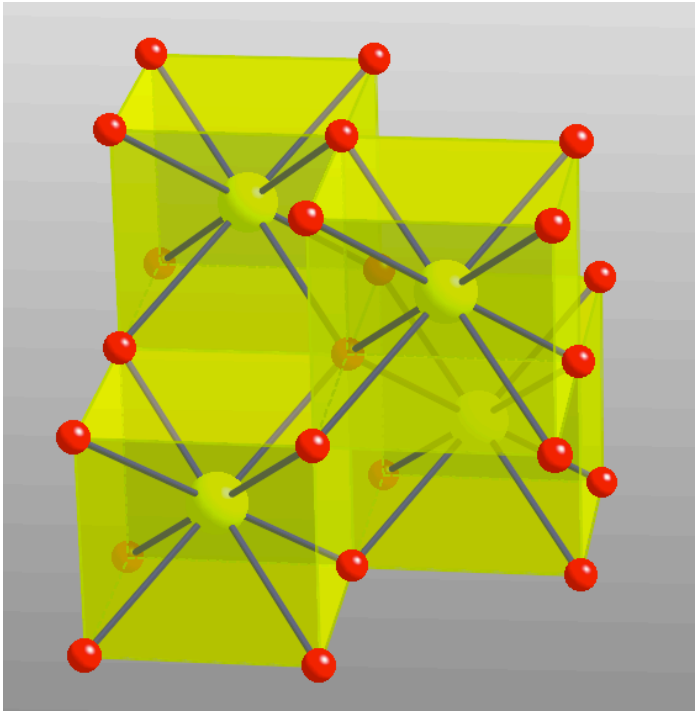

Figure 1.4: CeO_2 unit cell viewed as a primitive array of oxygen ions (red or dark) occupying the eight corners of tetrahedral polyhedra centered on cerium ions (yellow or light colored). False ionic radii are used for clarity. Model created in CrystalMaker.

cation site, the resulting reduction of Ce^{4+} to Ce^{3+} does result in the electron in existing as a small polaron[1] [26]. This was determined by Tuller and Norwick in 1975 who investigated the electrical properties of reduced ceria, CeO_{2-x}, carried out on single crystals, and determined that CeO_{2-x} provided one of the clearest examples of hopping conduction and the small polaron mechanism [26]. The presence of the polaron is charge compensated by the formation of an oxygen vacancy. The third reason that ceria is an important material as an SOFC electrolyte is that oxygen ion conductivity goes up significantly when doped with trivalent cations because of the increase in the vacancy concentration [27–30]. Catlow [31] explained that oxygen vacancy migration in ceria and doped-ceria takes place through a

[1] "A small polaron is a defect created when an electronic carrier becomes trapped at a given site as a consequence of the displacement of adjacent atoms or ions. The entire defect (carrier plus distortion) then migrates by an activated hopping mechanism. Small polaron formation can take place in materials whose conduction electrons belong to incomplete inner (*d* or *f*) shells which, due to small electron overlap, tend to form extremely narrow bands." Ref. [26]

simple hopping mechanism. The likely migration events involve an oxygen ion hopping to a vacant site in a first nearest neighbor or to a second nearest neighbor position.

In one of the earliest studies of ionic conductivity, Tuller and Nowick [25] studied ionic conductivity as a function of temperature in yttrium-doped ceria. They found that, compared to pure ceria, doped ceria showed higher conductivity, lower activation energy for anion vacancy migration, and absence of polarization effects to lower temperatures. This led them to predict that doped ceria would be ideal candidates for lower temperature SOFCs. Bourneau and Carniato [32], in noting that the theoretical calculations of formation energies provide values larger than expected from thermodynamic data, speculated that the reasons may be because the interactions between oxygen vacancies are very complex.

Electrical conductivity is measured using DC four-probe method on sintered ceramic samples [9]. However, this method can introduce errors due to the grain boundaries and electrodes and may mask the true behavior of the bulk. This uncertainty can be removed by the use of the complex plane impedance analysis. Bulk and grain boundary contributions can also be individually resolved using AC impedance spectroscopy as reported by Stephens and Kilner [33]. Inaba and Takagawa have plotted the electrical conductivities of different fluorite structures (Fig. 1.5) using data from B. C. H. Steele [13] that show that the very high conductivity of the ceria doped oxides make them attractive candidates for use as the electrolyte in solid oxide fuel cells. Although Bi_2O_3 and yttria-stabilized Bi_2O_3 are the most conductive, they are structurally not stable and are easily reduced thus making them unsuitable for use as an SOFC electrolyte. The δ-Bi_2O_3 structure is monoclinic at low temperatures and becomes cubic with ionic conduction at high temperature but is easily reduced at low oxygen partial pressures [34] making it unsuitable to be used as an SOFC electrolyte. Eguchi et al. measured the ionic conductivities of doped ceria with several rare earth elements [27]. They found that in general the ionic conductivity went up with the increase in dopant radius (Fig. 1.6).

Trovarelli [14] has listed experimental values for activation energies of ceria that range from 3.6–24.8 Kcal/mol (0.16–1.08 eV) for experiments conducted in the temperature

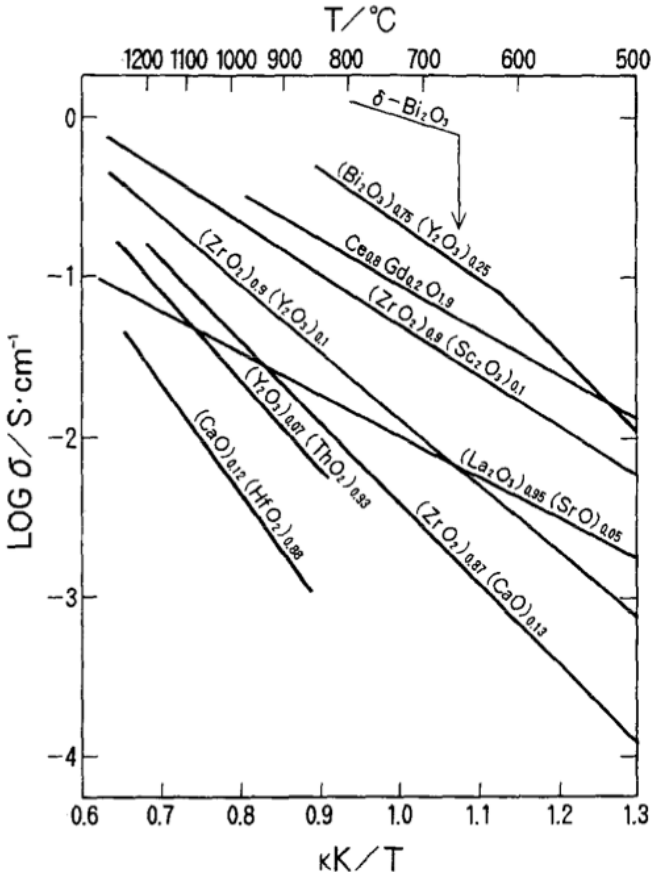

Figure 1.5: Electrical conductivity of fluorite oxides. Although Bi_2O_3 and yttria-stabilized Bi_2O_3 are the most conductive, they are structurally not stable and are easily reduced thus making them unsuitable for use as an SOFC electrolyte. Of the other choices doped ceria is clearly the most promising. From Inaba and Tagagawa [9] with data from Steele [13].

range of 1123–1423 K. Trovarelli notes that the activation of stoichiometric ceria is higher than that of CeO_{2-x} due to the decrease in the energy needed to create a defect in CeO_{2-x} compared to CeO_2. B. C. H. Steele [4] report the activation energy of Gd^{3+} doped ceria ($Ce_{0.9}Gd_{0.1}O_{1.95}$) to be 0.64 eV and that for Sm^{3+} doped ceria ($Ce_{0.9}Sm_{0.1}O_{1.95}$) to be 0.66 eV. They also report a value of $E_a = 0.87$ eV for Y^{3+} doped ceria $Ce_{0.887}Y_{0.113}O_{1.9435}$ which is the same as reported by Kamiya et al. [35]. These experimental values and those obtained by others for ceria and doped ceria are summarized in Table 1.1 that shows that the oxygen ion conductivity of ceria-based oxides is strongly dependent on the type and concentration of the dopant.

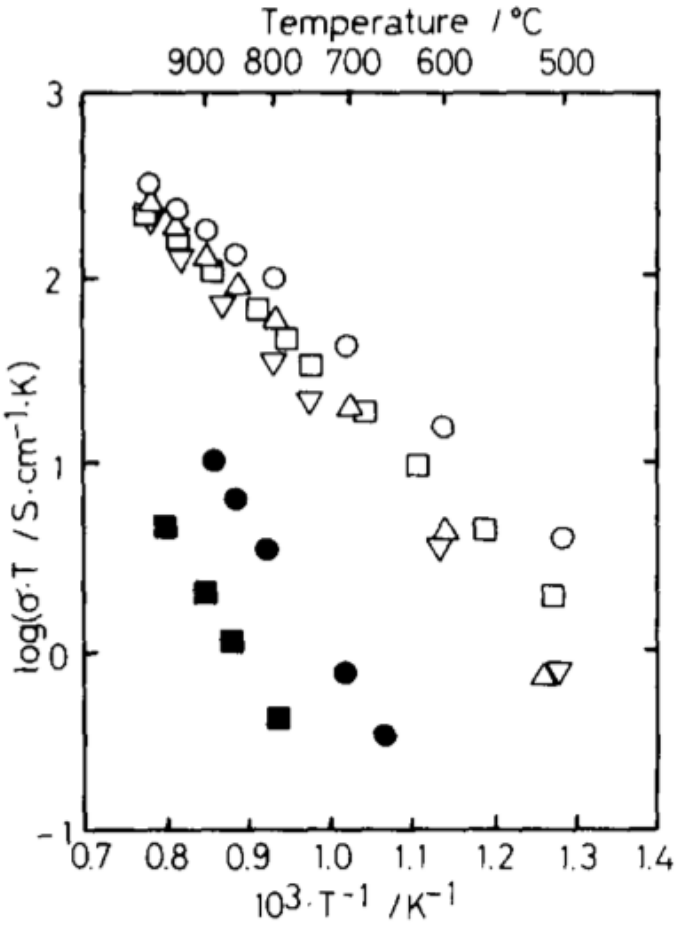

Figure 1.6: Arrhenius plot of ionic conductivity of ceria based rare-earth oxides. ○: $(CeO_2)_{0.8}(SmO_{1.5})_{0.2}$; △: $(CeO_2)_{0.8}(GdO_{1.5})_{0.2}$; ▽: $(CeO_2)_{0.8}(YO_{1.5})_{0.2}$; □: $(CeO_2)_{0.8}(CaO_{1.5})_{0.2}$; ■: CeO_2; ●: $(ZrO_2)_{0.85}(YO_{1.5})_{0.15}$; From Eguchi et al. [27].

1.4 Literature Review—Theoretical

First principles studies of the CeO_2 structure were carried out by Yang et al. [22,39] who report calculated lattice constant values of 5.45 Å and 5.48 Å respectively. Pornprasertsuk et al. [40] studied the ionic conductivity of yttria-stabilized zirconia (YSZ) and calculated the activation energies using density functional theory. Then they used kinetic Monte Carlo simulations using Boltzmann probabilities mechanism to determine the dopant concentration dependence of the oxygen self-diffusion coefficient for varying amounts of Y_2O_3. Their finding was that maximum conductivity occurs at 7-9 mol% Y_2O_3 at 600–1500 K.

Table 1.1: Experimentally observed activation energy E_a values for oxygen vacancy migration in ceria and doped ceria. For references with data involving doped ceria, the activation energy values for the lowest dopant concentration are quoted. Table from Ref. [8].

Material	E_a (eV)	Material	E_a (eV)
Ceria[a]	0.49	Gd-doped ceria[b]	0.75
Ceria[c]	0.52	Gd-Pr-doped ceria[b]	0.76
Ceria[d]	0.76	Gd-doped ceria[e]	0.64
Y-doped ceria[a]	0.99	Sm-doped ceria[e]	0.66
Y-doped ceria[d]	0.76	Y-doped ceria[f]	0.87
CaO-doped ceria[d]	0.91	Pr-doped ceria[g]	0.42
Nd-doped ceria [f]	0.54	Pr-doped ceria[h]	0.37

[a] Reference [36]
[b] Reference [37]
[c] Reference [38]
[d] Reference [26]
[e] Reference [4]
[f] Reference [35]
[g] Reference [29]
[h] Reference [30]

However, this and a number of other studies show that to make the ionic conductivity of YSZ useable high operating temperatures ($\sim 1{,}000\ ^\circ$C) is needed.

The ionic conductivity σ of any material is given by an Arrhenius type expression

$$\begin{aligned} \sigma T &= \sigma_o \exp\left(\frac{-E_a}{k_B T}\right) \\ E_a &= E_f + E_m \end{aligned} \tag{1.1}$$

where E_a is the activation energy for oxygen vacancy diffusion, T is the temperature in Kelvins, k_B is the Boltzmann constant, and σ_o is a constant independent of the temperature. E_a is the sum of the vacancy formation energy E_f and the migration energy E_m. This equation tells us that in order to lower the operating temperature while keeping the ionic conductivity high we need to find materials with lower activation energies E_a. Inaba and Takagawa in their review article [9] mention several studies that point out that the rare-earth doped-ceria are prime candidates for lowering the activation energy barrier. Kilner and Brook [41] remark that "it appears likely that the strain energy term is generally the

most important part of the association enthalpies," so that dopants should be chosen in order to minimize the lattice strain.

Andersson et al. in their 2006 paper [1] show, using DFT calculations, that there is a clear minimum (Fig. 1.7) for the activation energy E_a for oxygen vacancy diffusion in ceria doped with elements from the lanthanide series with the ideal dopant having an effective atomic number between 61 (Pm) and 62 (Sm). Their results also show "a remarkable correspondence between vacancy properties at the atomic level and the macroscopic ionic conductivity." When ceria is doped with lower valence cations oxygen vacancies are intro-

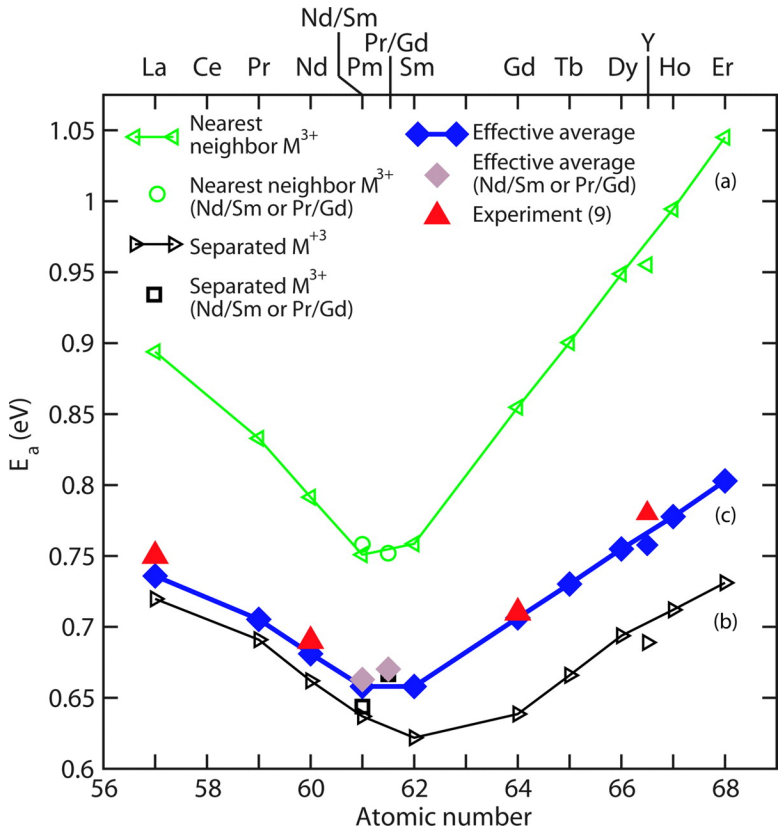

Figure 1.7: E_a for dopants sitting next to each other (a) and separated from each other (b) and an effective average of the former two (c). The results were obtained within the $3 \times 2 \times 2$ supercell, which implies a dopant concentration of 4.2%. Figure from Ref. [1].

duced in order to maintain charge neutrality. These extra vacancies in doped ceria increase the ionic conductivity. Andersson et al. mention that because of interactions the dopants

and vacancies form associates with a certain binding energy that they call the association energy E_{ass} which prevents the vacancies from being mobile (also Ref. [42]). In doped ceria E_{ass} plays a similar role to that played by E_f in pure ceria in determining the number of mobile vacancies, so we can write $E_a = E_{ass} + E_m$. Although at high temperatures most vacancies will be dissociated, at low to intermediate temperature solid oxide fuel cells (IT-SOFC) the goal is then to find dopants and dopant concentrations that minimize E_{ass} in order to minimize E_a. They showed how E_f is dependent on the local configuration of dopants and vacancies with "small" ions preferring to have vacancies in the nearest neighbor (NN) position and the "large" ions preferring to have them in the next nearest neighbor (NNN) position.

In another paper [43] Andersson et al. studied the electronic structure and thermodynamic properties of CeO_2 and Ce_2O_3 from first principles (LDA, GGA, LDA+U)[2]. They explored how the properties of CeO_2 and Ce_2O_3 are affected by the choice of U as well as the choice of exchange-correlation potential, i.e., the LDA or GGA. They also studied the reduction of CeO_2, leading to formation of Ce_2O_3 and Ce_2O_{2-x}, and its dependence on U and exchange-correlation potential. Their results show that by choosing an appropriate U it is possible to consistently describe structural, thermodynamic, and electronic properties CeO_2, Ce_2O_3 and Ce_2O_{2-x}, which enables modeling of redox processes involving ceria-based materials. They report finding $U \approx 6$ eV for LDA and $U \approx 5$ eV for GGA.

Yang et. al. [44] report on the oxygen vacancy formation energy E_{vac} in Pd-doped ceria using DFT+U method, that is, first principles density functional theory calculations with the inclusion of on-site Coulomb interaction, using similar U as above. They found that E_{vac} is lowered in Pd-doped ceria compared to pure ceria by 3 eV. The Pd dopant was found to have significant effects on the reduction properties of ceria.

In two separate papers in 2010 Dholabhai et al. [7, 8] studied oxygen vacancy migration in ceria, praseodymium-doped ceria, and gadolinium-doped ceria using density

[2]These acronyms refer to different approximations to the density functional theory and is discussed in the next chapter.

functional theory. These papers report on the activation energies for vacancy formation and migration in pure ceria and for different pathways in doped ceria. They found that for Pr-doped ceria the second nearest neighbor was the most favorable vacancy formation site. On the other hand, for Gd-doped ceria the first nearest neighbor to the dopant was found to be the most favorable site for the formation of an oxygen vacancy. They explained that this was due to the comparable ionic radii of the Gd^{3+} and the host Ce^{4+} ions.

Adams et al. [45] described the kinetic lattice Monte Carlo (KLMC) method to model dynamic processes over long time periods. This method only deals with problems dealing with atoms on bulk lattice sites and their migration from site to site in the crystal structure. In this method the atom sits on atomic sites and the code simulates the motion (kinetics) between lattice sites. The jump events are randomly picked one at a time according to some weighted probability. The input to the KLMC method may be the activation energies calculated from atomic level simulations [46]. We will be using a variant of the KLMC method in determining oxygen vacancy diffusion in doped ceria.

Monte Carlo methods have also been used by others [36, 40, 47–50] to study electrolyte applications in solid oxide fuel cells. One of these studies [47] used semi-empirical potentials while the others [36, 40, 48–50] used density functional theory (DFT) methodology to determine the energetics for oxygen vacancy diffusion in oxides (yttria-stabilized zirconium and yttria-doped ceria). Among the studies performed using DFT methodology, some [36, 40, 48, 49] of the studies determined activation energies from static calculations, and one [50] study determined energetics from *ab initio* molecular dynamics. The resulting activation energies were used as input into KLMC models of oxygen vacancy diffusion. However, none of these models included the effect of vacancy-vacancy interaction, which we investigate in our work. Overall, these earlier calculations demonstrate that kinetic Monte Carlo is a powerful technique for investigating oxygen vacancy diffusion (and hence ionic conductivity) in doped oxides.

Using percolation theory and neglecting the Coulomb repulsion between vacancies, Meyer et al. [51] deduced that for systems with the fluorite structure there are many

percolating paths for vacancy diffusion for low dopant concentrations. They interpreted that at higher dopant concentration, many diffusion pathways are blocked due to attraction of vacancies to the dopants leading to a decrease in ionic conductivity. Other calculations used Monte Carlo approaches to analyze oxygen mobility in complex oxide systems such as CeO_2-ZrO_2 and $CeO_2-ZrO_2-La_2O_3$ in platinum catalysts [52]and determined the equilibrium composition profile across a coherent interface in Sm-doped ceria [53]. Hull et al. [54] performed analysis of the total scattering using reverse Monte Carlo modeling of anion deficient ceria. They showed that the oxygen vacancies preferentially align as pairs in the (111) cubic directions as the degree of nonstoichiometry increases.

Molecular dynamics simulations have been used earlier to identify the trends in ionic conductivity as a function of dopant concentration. Hayashi et al. [55] used molecular dynamics simulations to investigate oxygen diffusion and the microscopic structure of ceria-based solid electrolytes with different dopant radii. Inaba et al. [56] studied oxygen diffusion in Gd-doped ceria using molecular dynamics simulations. They attributed the larger size of the trivalent Gd dopant ion to the higher calculated diffusion constant as compared to Y-doped ceria. An issue with molecular dynamics simulations is that they are performed over a very short time frame that can lead to insufficient statistical sampling of various configurations.

In the literature survey above we have discussed the importance of doped ceria as the electrolytic material for solid oxide fuel cells, the experimental findings of activation energies and ionic conductivities, and some studies that have used first principles calculations in order to determine the type of doped electrolyte that would increase the ionic conductivity. Some other studies have also used molecular dynamics methods to investigate oxygen vacancy diffusion in doped ceria. However, most of the past studies have investigated only part of the diffusion pathway, and may have missed the true rate-limiting jump events and have not explored the full complex dopant–vacancy and vacancy–vacancy interactions.

1.5 Goals of This Study

Currently vigorous efforts are underway to experimentally characterize bulk diffusion mechanisms and to develop optimal doped ceria electrolytes. However, they do not lend to an understanding of the mechanism of ionic conduction at the atomic level. This understanding is important in order to develop better ionic conductors such as by the use of suitable co-dopants. The goals of this dissertation is to develop a fundamental understanding of defect migration at the atomic level for both doped and pure ceria. In this research we have considered several elements of the lanthanide series as dopants. We have explored the different pathways for oxygen vacancy migration in doped ceria via vacancy hopping mechanisms for varying dopant concentrations and temperatures. Since the introduction of the dopants affects vacancy formation and migration we have investigated the effects on the first three nearest neighbors, having determined that the effects on more distant neighbors are negligible. We have used density functional theory (DFT+U) calculations to calculate the energies and have chosen the *ab initio* total-energy and molecular-dynamics program VASP (Vienna *ab initio* simulation program) to carry out our calculations. To model the diffusion mechanism of the transport of the charge carriers I have co-developed a novel random events code, the Kinetic Lattice Monte Carlo (KLMC) program, to carry out our simulations.

In the next chapter I discuss the principles of the density functional theory, followed by a chapter discussing the diffusion and ionic conductivity in doped ceria. In Chapter 4, I discuss how the DFT calculations are carried out in VASP and discuss the results obtained for neodymium doped ceria. In Chapter 5, I discuss the KLMC code and in the following chapters I discuss the calculations and results of using the KLMC code to simulate the ionic conductivity in praseodymium, gadolinium and neodymium doped ceria. The contents of praseodymium and gadolinium doped ceria have been published (or are being published) in two papers that I co-authored (with Pratik Dholabhai being the first author).

Chapter 2

PRINCIPLES OF DENSITY FUNCTIONAL THEORY

In this chapter I discuss in brief the principles of the density functional theory (DFT) and use these concepts to simulate doped ceria in Chapter 4. I have opted to use the density functional theory for calculating oxygen vacancy formation and migration in doped ceria because it yields results that are better than those employing, say, empirical potentials.

Shortly after Erwin Schrödinger's epoch-making 1926 publication [57] on wave mechanics, Paul Dirac[1] boldly pronounced [58] that "The general theory of quantum mechanics is now almost complete .... The underlying physical laws necessary for the mathematical theory of a large part of physics and the whole of chemistry are thus completely known, and the difficulty is only that the exact application of these laws leads to equations much too complicated to be soluble. It therefore becomes desirable that approximate practical methods of applying quantum mechanics should be developed, which can lead to an explanation of the main features of complex atomic systems without too much computation." The density functional theory (DFT) is an exact method in principle that is "an alternative approach to the theory of electronic structure, in which the electron density $\rho(\vec{r})$, rather than the many-electron wavefunction, plays a central role" [59]. However, solutions to the the DFT require some approximations.

2.1 The Schrödinger Equation for a Many-Body System

As a prelude to describing the describing the density-functional theory we first discuss the rudimentary wave-function theory. The central equation that describes the interaction of the electrons and the nuclei of a many-body system is the Schrödinger equation. The time-independent, non-relativistic form of the Schrödinger equation was first written as an elegant eigenvalue equation by Dirac [58] as

$$\mathscr{H}\Psi = E\Psi \tag{2.1}$$

[1] P. Dirac and E. Schrödinger were jointly awarded the Noble prize in Physics in 1933.

where $\mathscr{H}$ is the Hamiltonian operator, the eigenstates Ψ are a set of solutions that are the wave-functions, with associated eigenvalues E that are the energies of the system. What this equation, originally developed to describe the equation of motion in classical mechanics, says is that for a given Hamiltonian operator operating on a set of wavefunctions that satisfies this equation, we get the same wavefunctions back multiplied by a measurable quantity, that is the energy of the system. The Ψ with the lowest energy is the ground state eigenstate whereas the other solutions corresponds to the higher energy eigenstates. Although Eq. 2.1 is quite innocuous looking, difficulty arises in dealing with the many-body terms that comprise the Hamiltonian as we shall see in Eq. 2.9, and judicious approximations need to be made in solving this equation of motion. For atomic systems the Hamiltonian operator consists of five terms that describe the motions and interactions of the electrons and the nuclei. They are 1) the kinetic energy operator for the nuclei (T_N), 2) the kinetic energy operator for the electrons (T_e), 3) the electron-electron interaction (V_{ee}) operator, 4) the electron-nucleus interaction (V_{Ne}) operator, and 5) the nucleus-nucleus (V_{NN}) interaction operator. If we let the spatial coordinates of the n electrons be represented by $\vec{x} \equiv \vec{x}_1, \ldots, \vec{x}_n$, let s represent the spin, let $\vec{r} = \vec{r}(\vec{x}, s)$ represent the full set of electronic positions and spin variables, and let the coordinates of the N nuclei by $\vec{R} \equiv \vec{R}_1, \ldots, \vec{R}_N$, then the above Hamiltonian can be written as

$$\mathscr{H} = T_N + T_e + V_{ee}(\vec{r}) + V_{Ne}(\vec{R}, \vec{r}) + V_{NN}(\vec{R}) \tag{2.2}$$

and the full Schrödinger equation can be written, as

$$\left[T_N + T_e + V_{ee}(\vec{r}) + V_{Ne}(\vec{R}, \vec{r}) + V_{NN}(\vec{R}) \right] \Psi(\vec{r}, \vec{R}) = E\Psi(\vec{r}, \vec{R}). \tag{2.3}$$

2.2 Components of the Hamiltonian

The kinetic energy operator of the N nuclei is given by

$$T_N = \sum_{I=1}^{N} \left(-\frac{\hbar^2}{2M_I} \nabla^2_{\vec{R}_I} \right) \tag{2.4}$$

where $\hbar = h/2\pi = 1.05457 \times 10^{-34}$J s $= 6.58212 \times 10^{-16}$eV s, h is the Planck constant, M_I is the mass of the I-th nucleus at positions $\vec{R}_I$. Similarly, the kinetic energy operator of the

n electrons of mass m_e each at positions $\vec{r}_i$ is given by

$$T_e = \sum_{i=1}^{n} \left(-\frac{\hbar^2}{2m_e} \nabla^2_{\vec{r}_i} \right). \tag{2.5}$$

The ∇^2 operator basically measures the curvature of the wavefunction. Rapidly varying wavefunctions have high kinetic energy. Since the interactions between the charged particles are Coulombic in nature, we can write the electron-electron repulsive energy operator, avoiding double counting, as

$$V_{ee}(\vec{r}) = \sum_{i>j} \frac{e^2}{|\vec{r}_i - \vec{r}_j|}. \tag{2.6}$$

We note that this term couples all the electrons in the system and is quite formidable in the *many*-body Schrödinger equation.

The electron-nucleus attractive energy operator between the electrons of charge e at positions $\vec{r}_i$ and the nuclei of charges eZ_I at positions $\vec{R}_I$ can be written as

$$V_{Ne}(\vec{R}, \vec{r}) = -\sum_{i=1}^{n} \sum_{I=1}^{N} \frac{Z_I e^2}{|\vec{R}_I - \vec{r}_i|} \tag{2.7}$$

The nucleus-nucleus repulsive energy operator is similarly given, again avoiding double counting, by

$$V_{NN}(\vec{R}) = \sum_{I>J} \frac{Z_I Z_J e^2}{|\vec{R}_I - \vec{R}_J|}. \tag{2.8}$$

The full Hamiltonian of the many-body system can then be written as

$$\mathscr{H} = -\sum_{I=1}^{N} \frac{\hbar^2}{2M_I} \nabla^2_{\vec{R}_I} - \sum_{i=1}^{n} \frac{\hbar^2}{2m_e} \nabla^2_{\vec{r}_i} + \sum_{i>j} \frac{e^2}{|\vec{r}_i - \vec{r}_j|} - \sum_{i=1}^{n} \sum_{I=1}^{N} \frac{Z_I e^2}{|\vec{R}_I - \vec{r}_i|} + \sum_{I>J} \frac{Z_I Z_J e^2}{|\vec{R}_I - \vec{R}_J|}. \tag{2.9}$$

The Schrödinger equation for this full Hamiltonian is inextricable for all but the simplest cases such as the hydrogen or helium atoms. Therefore, we need to make appropriate approximations and develop techniques so that we are able to come up with meaningful solutions to this equation for many-body systems.

The biggest impediment to solving the Schrödinger equation is the electron-electron interaction term (Eq. 2.6). Unlike the other terms that contain the coordinate of one electron at a time, this term means that we have to solve for all the electrons in the system all at once. We can, however, solve the one-electron problems iteratively to approach the true solution

of the many-body Schrödinger equation. Two popular approaches are used to tackle this issue. One is the Hartree-Fock (HF) method and the other is the density functional theory (DFT) method. In the Hartree-Fock method an approximate many-electron wavefunction is constructed from one-electron wavefunctions in an appropriate effective potential. However, the Hartree-Fock methods are computationally demanding, limiting their applications to small molecules. In the density functional theory method the many-electron problem is transformed to a one-electron problem in an unknown effective potential.

2.3 The Born-Oppenheimer Approximation

Since the nuclear masses are many times larger than the electronic mass ($M_I/m_e \gg 1$), we can consider the kinetic energy term for the nuclei to be much smaller than the kinetic energy term for the electrons and can thus safely drop the first term from the Hamiltonian in Eq. 2.9. This is reasonable for all cases except for the very lightest elements like hydrogen where the ions have to be treated like quantum mechanical particles [60]. The Born-Oppenheimer approximation then basically considers the nuclei to be at fixed positions and the electrons to be moving in the field of this set of nuclei, thus treating the electrons and nuclei as separate mathematical problems. Therefore, we can separate the wavefunction into an electronic part $\Psi_{\mathscr{E}}(\vec{r},\vec{R})$ and a nuclear part $\Psi_N(\vec{R})$

$$\Psi(\vec{r},\vec{R}) = \Psi_{\mathscr{E}}(\vec{r},\vec{R})\Psi_N(\vec{R}). \tag{2.10}$$

Dropping the kinetic energy term for the nuclei, we can then write the electronic Hamiltonian as [61]

$$\mathscr{H}_{\mathscr{E}}(\vec{r},\vec{R}) = T_e + V_{ee}(\vec{r}) + V_{Ne}(\vec{R},\vec{r}) + V_{NN}(\vec{R}). \tag{2.11}$$

Therefore, with this approximation the electronic Schrödinger equation reduces to

$$\left[-\sum_{i=1}^{n}\frac{\hbar^2}{2m_e}\nabla^2_{\vec{r}_i} + \sum_{i>j}\frac{e^2}{|\vec{r}_i-\vec{r}_j|} - \sum_{i,I}\frac{Z_I e^2}{|\vec{R}_I-\vec{r}_i|} + \sum_{I>J}\frac{Z_I Z_J e^2}{|\vec{R}_I-\vec{R}_J|}\right]\Psi_{\mathscr{E}}(\vec{r},\vec{R}) = E\Psi_{\mathscr{E}}(\vec{r},\vec{R}) \tag{2.12}$$

We next realize that the ion-ion interaction term $\sum(Z_I Z_J e^2/|\vec{R}_I-\vec{R}_J|)$ is independent of the electronic degrees of freedom and may be considered a constant. It can therefore be calculated separately and later added to the total energy. The Schrödinger equation for the

time-independent, non-relativistic case, with the Born-Oppenheimer (or adiabatic) approximation then further reduces to

$$\left[-\sum_{i=1}^{n}\frac{\hbar^2}{2m_e}\nabla^2_{\vec{r}_i}+\sum_{i>j}\frac{e^2}{|\vec{r}_i-\vec{r}_j|}-\sum_{i,I}\frac{Z_I e^2}{|\vec{R}_I-\vec{r}_i|}\right]\Psi(\vec{r},\vec{R})=E\Psi(\vec{r},\vec{R}). \tag{2.13}$$

We emphasize here that since, as mentioned before, the coordinates $\vec{r}=\vec{r}(\vec{x},s)$ represent the full set of electronic positions and spin variables, the set of eigenfunctions $\Psi(\vec{r},\vec{R})$ of the Schrödinger equation are solved subject to the constraint that the wavefunctions are antisymmetric. That is, the $\Psi(\vec{r},\vec{R})$ change sign if the coordinates of any two electrons are interchanged. It is still quite an inextricable equation. We need to consider two other properties of the electrons. One is the *exchange* property that is a consequence of the Pauli exclusion principle. The exchange property stipulates that when two electrons of the same spin interchange positions then the sign of the wavefunction Ψ must change sign. The other is the *correlation* property of the electrons. This is a consequence of every electron being influenced by the motion of every other electron in the system.

2.4 The Hartree-Fock Approximation

The Hartree-Fock method is one of the approaches in which one tries to construct an approximate many-electron wavefunction from one-electron wavefunctions, determined in some approximate effective potential. Higher order variants of the Hartree-Fock methods are usually only applied to small molecules since they are computationally very demanding.

In his approximation Hartree [62] totally neglected the electron–electron interaction. If we let h_i denote the the Hamiltonian for electron i then the total Hamiltonian of the electrons can be written as

$$H=\sum_{i=1}^{N}h_i. \tag{2.14}$$

For each electron the Hamiltonian equation

$$h\phi=E\phi \tag{2.15}$$

is satisfied by the *spin orbitals* ϕ. Each of this single electron Hamiltonian equation is satisfied by multiple eigenfunctions, so this defines a set of spin orbitals $\phi_j(\vec{r}_i\ (j=1,2,\ldots)$

where $\vec{r}_i$ are the vectors of coordinates that define the position of electron i and its spin state. Since for the non-interacting electrons the total Hamiltonian can be written as a sum of the one-electron operators h_i, we can write the eigenfunctions of H as the products of the one-electron spin orbitals known as the Hartree product:

$$\Psi(\vec{r}_1,\ldots,\vec{r}_N) = \phi_{j_1}(\vec{r}_1)\phi_{j_2}(\vec{r}_2)\ldots\phi_{j_N}(\vec{r}_N). \tag{2.16}$$

The problem with the Hartree product is that it does not satisfy all the important criteria for wavefunctions [63], such as the antisymmetry principle. Since electrons are fermions, the wavefunction must change sign if two electrons change places with each other, but the Hartree product does not change sign if two electrons exchange positions. A better approximation to the wavefunction is achieved by using Slater [64] determinants[2]. Using the Slater determinant the eigenfunction is written as

$$\Psi(\vec{r}_1,\ldots,\vec{r}_N) = \frac{1}{(N!)^{1/2}}\begin{vmatrix} \phi_1(\vec{r}_1) & \phi_1(\vec{r}_2) & \phi_1(\vec{r}_3) & \ldots \\ \phi_2(\vec{r}_1) & \phi_2(\vec{r}_2) & \phi_2(\vec{r}_3) & \ldots \\ \phi_3(\vec{r}_1) & \phi_3(\vec{r}_2) & \phi_3(\vec{r}_3) & \ldots \\ . & . & . & \ldots \\ . & . & . & \ldots \end{vmatrix} \tag{2.17}$$

where the coefficient $\frac{1}{(N!)^{1/2}}$ is a normalization factor. It is perhaps easier to see the antisymmetry property by examining the case for a two-electron system. Then the Slater determinant becomes

$$\begin{aligned}\Psi(\vec{r}_1,\ldots,\vec{r}_N) &= \frac{1}{\sqrt{2}}\begin{vmatrix} \phi_1(\vec{r}_1) & \phi_1(\vec{r}_2) \\ \phi_2(\vec{r}_1) & \phi_2(\vec{r}_2) \end{vmatrix} \\ &= \frac{1}{\sqrt{2}}[\phi_1(\vec{r}_1)\phi_2(\vec{r}_2) - \phi_2(\vec{r}_1)\phi_1(\vec{r}_2)].\end{aligned} \tag{2.18}$$

The physical description of the electron exchange is explicitly built into this construction since this changes sign if two electrons are exchanged. Also, this construction does not

[2]Dirac in his original 1926 article [65] pointed out that the wavefunctions for non-interacting electrons of a given spin (up or down) can be written as a determinant of one-electron orbitals. Slater later showed that the wavefunction including spin can be written as a determinant of "spin orbitals" [66].

distinguish between electrons and disappears if two of the one-electron wavefunctions are the same or if two electrons have the same coordinates. Thus the Slater determinant satisfies the Pauli exclusion principle.

Of course, in any real system the electrons interact with each other. The simplest wavefunction based approach to approximate these interactions is the Hartree-Fock (HF) method. In the Hartree-Fock method the positions of the atomic nuclei are kept fixed and the wavefunctions of the N-interacting electrons are determined.

In the HF method the Schrödinger equation of each electron is written as

$$\left[-\frac{\hbar^2}{2m}\nabla^2 + V(\vec{r}) + V_H(\vec{r})\right]\phi_j = E_j\phi \tag{2.19}$$

where the second term is the interaction between the electron and the collection of atomic nuclei, and the third term is the Hartree potential

$$V_H(\vec{r}) = \int \frac{\rho(\vec{r}')}{|\vec{r}-\vec{r}'|}d\vec{r}' \tag{2.20}$$

where $\rho(\vec{r})$ is the density of the electrons at the position $\vec{r}$. This means that each electron experiences the effect of other electrons only as an average and not as instantaneous interactions. In order to solve the single-electron equation the exact spin orbitals are approximated as a linear combination of functions $\varphi_i(\vec{r})$:

$$\phi_j(\vec{r}) = \sum_{i=1}^{K} \alpha_{j,i}\varphi(\vec{r}) \tag{2.21}$$

where the set of functions $\varphi_1(\vec{r}), \varphi_2(\vec{r}), \ldots, \varphi_K(\vec{r})$ is called the *basis set*. The larger the basis set (that is, the larger the K), the more accurate is our calculation, although it also increases the computational efforts. Also, the judicious choice of basis sets that approach the spin orbitals of real materials also increases the accuracy of the HF calculations. The average charge density is given by

$$\rho(\vec{r}) = \sum_{j=1}^{N} |\phi_j(\vec{r})|^2 \tag{2.22}$$

where, in the ground state, the summation is over the N lowest eigenvalues. In the Hartree-Fock method the spin orbitals depend on the charge density and the charge density itself

depends on the spin orbitals. Therefore, the calculations are done in a self-consistent iterative way [67]. We first start with a trial charge density $\rho(\vec{r})$, construct the Hartree potential $V_H(\vec{r})$ in Eq. 2.21, solve for ϕ_j, and then recalculate $\rho(\vec{r})$ from Eq. 2.22. If this charge density differs from the initial guess by some convergence criteria then we iterate until it is.

One drawback of the Hartree approach is the lack of accounting for electron correlation, or how electrons influence each other. Therefore, this method overestimates the electrostatic energy between the electrons [68]. The poor scaling of Hartree-Fock ($\sim N^4$) limits its application to large systems and is better suited for small molecules and can be directly solved only in special cases such as spherically symmetric atoms and the homogeneous electron gas [66]. Higher levels of theory, such as CI (configuration interaction), MP (Møller-Plesset perturbation theory), and QCI (quadratic configuration interaction), have been introduced [63] to incorporate correlation approximation into Hartree-Fock. The level of theory defines the approximations that are made to describe the electron–electron interactions. However, in order for the wavefunction based methods to converge to the true solution of the Schrödinger equation, these higher levels of theory need to be used in conjunction with larger basis sets necessitating[3] calculation operations to scale as $\sim N^7$. Therefore, these calculations are limited to individual molecules consisting of 10–30 atoms.

2.5 The Hohenberg-Kohn Theorems

The density functional theory (DFT) is an alternative method to the theory of electronic structure, such as the Hartree-Fock method, for solving Schrödinger type equations in which the electron density distribution $\rho(\vec{r})$, rather than the many-electron wavefunction, play a central role [59]. It allows the treatment of 100–1000 atoms on current computer systems as it scales as N^2–N^3, where N is the number of atoms. It is based on two remarkable theorems by Hohenberg-Kohn [69, 70] (later simplified and extended by Levy [71]).

[3]Using a basis set with more functions requires more computational effort since the numerical coefficients defining the magnitude of each function's contribution to the net function in Eq. 2.21 must be calculated.

1. All aspects of the electronic structure of a system of *interacting* electrons, in the *ground state*, in an 'external' potential $v(\vec{r})$, are completely determined by the electronic charge density $\rho(\vec{r})$.
2. The ground state energy of the interacting electron gas is a *unique* functional of the charge density $\rho(\vec{r})$.

The difficulty is that unfortunately, the functional is not known! However, whatever the functional is, it acquires a minimum value when the charge density $\rho(\vec{r})$ is the correct (true) $\rho(\vec{r})$. Practically, a variation principle is used to find the charge density.

Mathematically, the second theorem above states that the total energy functional[4] $E[\rho(\vec{r})]$ of interacting electrons in an external potential is given exactly as a functional of the ground state electronic density $\rho(\vec{r})$. By using an *reductivo ad absurdum* approach [69] Hohenberg and Kohn showed that the true ground state density is the density that minimizes $E[\rho(\vec{r})]$. In the Hohenberg-Kohn formulation the ground state energy of an interacting inhomogeneous electron gas in a static potential $v_{ion}(\vec{r})$ is written as

$$E[\rho(\vec{r})] = \int v_{ion}(\vec{r})\rho(\vec{r})d\vec{r} + \frac{1}{2}\int\int \frac{\rho(\vec{r})\rho(\vec{r}')}{|\vec{r}-\vec{r}'|}d\vec{r}d\vec{r}' + F[\rho(\vec{r})] \tag{2.23}$$

where $F[\rho(\vec{r})]$ is a universal functional of the charge density (that we mentioned above) and is valid for *any* number of particles and *any* external potential. The functional $F[\rho(\vec{r})]$ is expressed entirely in terms of the correlation energy and linear and higher order electronic polarizabilities of a uniform electron gas [69]. It is important to note here that this formulation is *exact* if $F[\rho(\vec{r})]$ is known.

2.6 The Local Density Approximation

In 1965 Kohn and Sham [70] [KS] derived approximation methods, that are somewhat analogous to the conventional Hartree and Hartree-Fock equations, for treating the Hohenberg-Kohn [HK]equation (Eq. 2.23), but maintains the major part of exchange and correlation.

[4] In contrast to a function that accepts a variable as its input and produces a number as its output, a *functional* accepts a function as its argument and produces a number as its output.

They first wrote the functional F as

$$F[\rho(\vec{r})] = T_s[\rho(\vec{r})] + E_{xc}[\rho(\vec{r})] \tag{2.24}$$

where $T_s[\rho(\vec{r})]$ is the kinetic energy of a system of non-interacting electrons with density $\rho(\vec{r})$ and $E_{xc}[\rho(\vec{r})]$ is the exchange and correlation energy of an interacting system with density $\rho(\vec{r})$. For a sufficiently slowly varying charge density $\rho(\vec{r})$ Kohn and Sham show that the exchange-correlation energy can be written as

$$E_{xc}[\rho(\vec{r})] = \int \rho(\vec{r})\varepsilon_{xc}(\rho(\vec{r}))d\vec{r} \tag{2.25}$$

where $\varepsilon_{xc}(\rho(\vec{r}))$ is the exchange and correlation energy per electron of a homogeneous, interacting electron gas of the same density $\rho(\vec{r})$. This approximation is known as the local density approximation (LDA). We make this explicit by adding a superscript

$$E_{xc}^{LDA}[\rho(\vec{r})] = \int \rho(\vec{r})\varepsilon_{xc}(\rho(\vec{r}))d\vec{r}. \tag{2.26}$$

We note that the charge density is a function of only three variables and that the 'external' potential is the set of nuclear potentials. We emphasize that the theory holds for the ground state but the band gaps are off for the excited states. According to Hohenberg-Kohn, then, we need to only know the electronic charge density to determine the ground state properties of the system. It is much simpler to deal with charge density $\rho(\vec{r})$ than the many-electron wavefunction.

In the Kohn-Sham self consistent formalism we start with an initial estimated charge density, which is usually a superposition of atomic densities $\rho(\vec{r})$. Fig. 2.1 shows a flow chart implementing this method. We then construct the Hartree potential

$$V_H(r) = \int \frac{\rho(\vec{r'})}{\mid \vec{r} - \vec{r'} \mid} d\vec{r}. \tag{2.27}$$

The effective potential is then given by

$$V_{eff}(\vec{r}) = V_H(\vec{r}) + V_N(\vec{r}) + V_{XC}(\vec{r}) \tag{2.28}$$

where V_N is the potential due to the nuclei and V_{XC} is the exchange-correlation potential, the latter being a purely quantum mechanical phenomena.

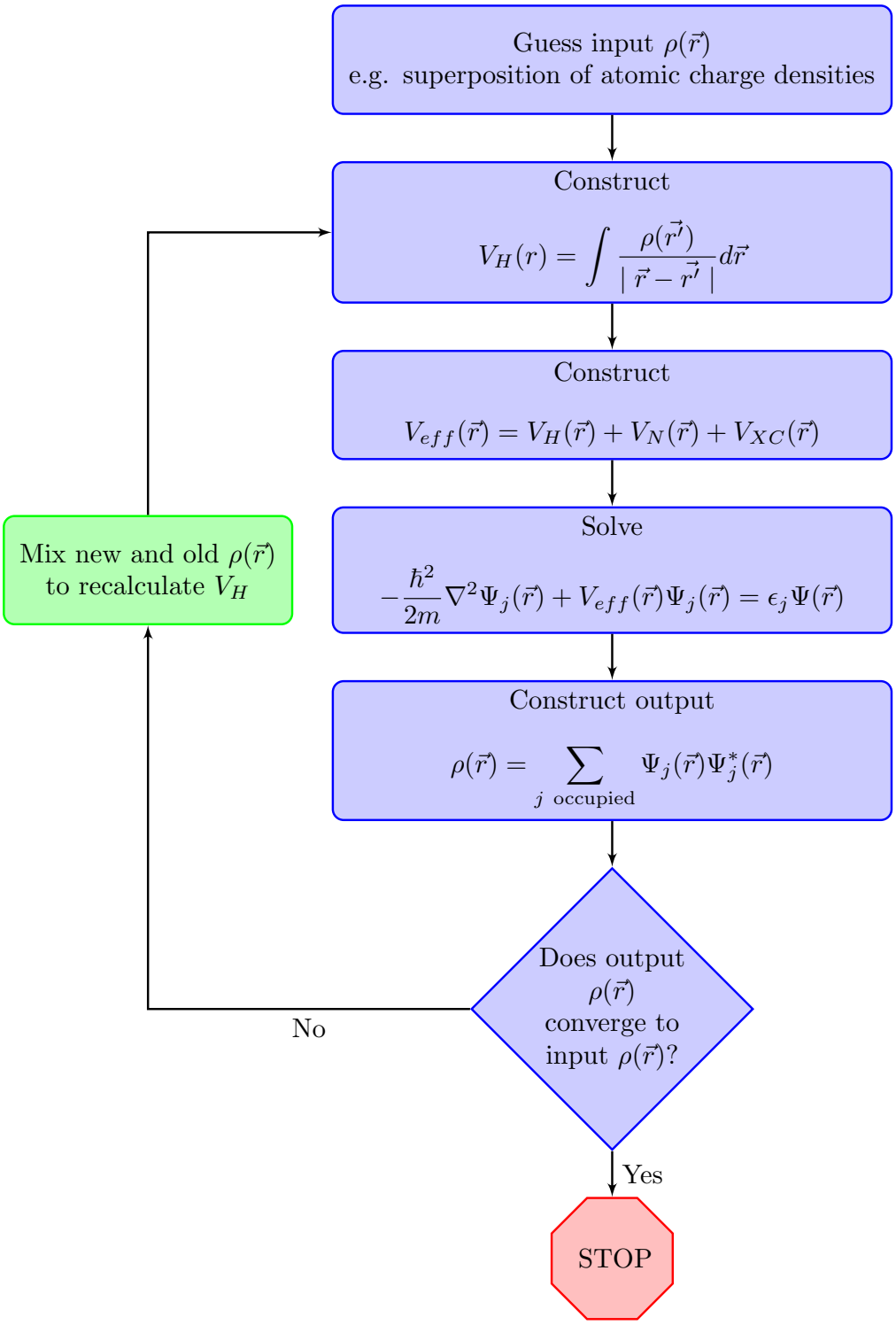

Figure 2.1: Flow chart of a self consistent calculation in the local density approximation (LDA) implementation of the density functional theory (DFT).

We then solve the Schrödinger equation

$$-\frac{\hbar^2}{2m}\nabla^2\Psi_j(\vec{r})+V_{eff}(\vec{r})\Psi_j(\vec{r})=\varepsilon_j\Psi(\vec{r}) \tag{2.29}$$

and use the generated wavefunctions to construct an output charge density

$$\rho(\vec{r})=\sum_{j \text{ occupied}}\Psi_j(\vec{r})\Psi_j^*(\vec{r}). \tag{2.30}$$

If this output is not the same as the input then we modify our initial guess for the charge density and repeat the calculations again. This is called the self-consistent field (SCF) calculation.

It is remarkable that LDA reasonably predicts many measurable quantities such as the ground state geometries, vibration and phonon frequencies, and moments of the density [72]. LDA gives ionization energies of atoms, dissociation energies of molecules, and cohesive energies with accuracies of 10-20% and bond lengths and geometries of solids and molecules with an accuracy of $\sim 1\%$ [59]. Although the solution of the Kohn-Sham equation is much easier than the Hartree-Fock equations, its accuracy for exchange energy is off by as much as 10% and correlation energy is typically overstated by a factor of 2, although these errors partially cancel each other out [59].

One important case where the LDA (and its extension to systems with unpaired electrons, LSDA) fails are systems that are dominated by electron-electron interaction effects, such as the heavy fermion systems. This is because such systems lack any resemblance to noninteracting electron gases [59]. Other shortcomings are that the LDA systematically underestimates excited state energies, and in particular, the band gaps in semiconductors and insulators[5]; overestimates the cohesive energies as mentioned above; gives the wrong ground state of some magnetic materials; and fails to appropriately describe the Van der Walls interactions [73].

One way to improve on the LDA is to incorporate the local gradient as well as the density by replacing $\varepsilon_{xc}(\rho(\vec{r}))$ in the Eq. 2.26 by $\varepsilon_{xc}(\rho,|\nabla\rho|)$. We then get what is known as

[5]This is reasonable to expect since the density functional theorem is based on the ground state only.

the generalized gradient approximation (GGA) [74–78] which is another approximation to the Kohn-Sham functional. The basic premise of the GGA is that since the electron densities of real materials are not uniform we can get a better functional by including the spatial variation in the electron density. Inclusion of the gradient corrections to ε_{xc} has led to better results for dissociation energies, improved cohesive energies, and more accurate predictions of magnetic properties. However, in some cases GGA overcorrects the deficiencies of the LDA and leads to an underbinding [73]. There are many different ways to include electron density gradient in a GGA functional leading to many distinct GGA functionals [79] and more detail can be found in Ref. [76]. Two widely used non-empirical GGA functionals are the Perdew-Wang functional (PW91) and the Perdew-Burke-Ernzerhof functional (PBE). These so-called "hybrid" functionals, that mix the exact results for the exchange part of the functional with approximations of the correlation part, are the most commonly used functionals in DFT calculations based on spatially localized basis functions [63]. The most popular functionals of this kind is the B3LYP functional, where B stands for Becke, who worked on the exchange part of the problem, the LYP stands for Lee, Yang, and Parr, who developed the correlation part of the functional, and the 3 describes the particular way that the results are mixed together [80, 81]. B3LYP employs a elaborate functional with three parameters and has the form

$$E_{xc}^{B3LYP} = E_{xc}^{LDA} + a_o(E_X^{HF} - E_x^{LDA}) + a_x(E_x^{GGA} - E_x^{LDA}) + a_c(E_c^{GGA} - E_c^{LDA}) \qquad (2.31)$$

with parameters $a_o = 0.20$, $a_X = 0.72$, and $a_C = 0.81$; E_{xc} is the exchange-correlation energy, E_x is the exchange energy, and E_c is the correlation energy. Although the form of the exact exchange results mean that they can be efficiently utilized for applications based on spatially localized functions, and not for applications using periodic functions [63], it is interesting to note that Baranek et al [82] and Kullgren, et al [83] were able to use the B3LYP functionals for the calculations of CeO_2 and Ce_2O_3, although B3LYP did not give results as good as that obtained by DFT+U, discussed below.

2.7 The DFT + U Approximation

Notwithstanding the successes of DFT there are cases where DFT (within the LDA and GGA approximations) fails even to give a correct qualitative description, for example by predicting a known insulator to be metallic [84, 85]. The main reason for this is due to the approximation of the exchange-correlation functionals. The failure of the DFT-LDA in strongly correlated electron materials, such as the transition metal oxides and the actinides, that contain many electrons in partially filled d or f shells, is because the d and f shells are inherently localized on each atomic site resulting in strong Coulombic repulsion between the electrons [84].

Since the self-interaction errors are cancelled exactly in the Hartree-Fock scheme, one can address the case of the strongly correlated electron materials by making a judicious combination of Hartree-Fock type approach for the localized states with DFT for the rest. This is the essence of the DFT+U methods [84, 86]. In the DFT+U method a correction to the DFT energy is introduced to correct for the electron self-interaction. This is done by introducing a single numerical parameter $U_{eff} = U - J$ where U is the Coulomb self-interacting term and and J is the exchange self-interaction term. *Ab intio* calculations can be carried out on test systems to determine the bounds on U_{eff}, but in practice this term is evaluated with a parametrized Hamiltonian instead of an explicit HF calculation. For example, the bulk modulus of a perfect crystal can be calculated and the value of $U - J$ that gives the best fit to the known bulk modulus is determined.

2.8 Basis Sets, Plane-waves, and Energy Cutoffs

As mentioned earlier, a judicious choice of basis sets for the expansion of the single-particle wavefunctions $\phi_j(\vec{r})$ (Eq. 2.21) is important for the solution of the Kohn-Sham equations. Two of the choices for the basis sets are the atomic orbitals[6] (AO) (also known as the spatially localized functions) and the plane-waves (PW) (the spatially periodic func-

[6] An excellent review of the selection of basis sets for molecular calculations can be found in Ref. [87].

tions). In quantum chemical calculations where localized bondings exist, such as for atoms, molecules, and clusters, the atomic orbitals basis sets are more efficient. Since the molecular orbital shapes often resemble those of the atomic orbitals, only a small number of basis functions are needed in the expansion of the wavefunctions. One of the common atomic orbital basis sets are the minimal basis sets STO-nG, where n is an integer that represents the number of Gaussian primitive functions comprising a single basis function [88]. In these basis sets, the same number of Gaussian primitives comprise the core and valence orbitals.

There have been a number of improvements over the minimal energy basis sets (that are fixed and are unable to adjust to different molecular environments), such as the split-valence basis sets. The idea behind these is that since it is the valence electrons that primarily participate in bonding then it is more prudent to represent valence orbitals by more than one basis function (each of which can in turn be composed of a fixed linear combination of primitive Gaussian functions). Examples of split-valence basis sets are the Pople basis sets and the correlation-consistent basis sets, such as cc-pVDZ and cc-pVTZ that been been carefully developed to be numerically efficient for molecular calculations [63]. One major issue with atomic orbital basis sets is that it is difficult to ensure the completeness of an AO basis set [89]. The completeness is important because it determines if properties such as the total energy are converged with respect to the number of basis sets [90].

Plane-wave basis sets are the method of choice for extended crystalline systems, particularly those containing metallic phases. Two of the advantages of plane-wave basis sets are that they are a set of orthogonal and complete functions. The accuracy of the basis can be systematically improved by simply increasing the number of basis functions thus facilitating the check for convergence. The essence of the PW method is that in the solution of the Schrödinger equation for a periodic system, the solution must satisfy Bloch's theorem [91], which states that the solution can be expressed as a sum of terms of the form

$$\psi_{n\vec{k}}(\vec{r}) = e^{i\vec{k}\cdot\vec{r}} u_{n\vec{k}}(\vec{r}), \tag{2.32}$$

where $e^{i\vec{k}\cdot\vec{r}}$ is a plane wave and the function $u_{n\vec{k}}(\vec{r})$ is periodic in space with the same peri-

odicity as the supercell (Bravais lattice), i.e.,

$$u_{n\vec{k}}(\vec{r}+\vec{R}) = u_{n\vec{k}}(\vec{r}). \tag{2.33}$$

The index n is known as the *band index* and occurs because for a given $\vec{k}$ (in reciprocal space) there are many independent eigenstates. Combining the last two equations Bloch's theorem can also stated in the alternate form: The eigenstate of the Hamiltonian $\mathscr{H}$ can be chosen so that for each wave-function ψ there is a wave vector $\vec{k}$ such that

$$\psi(\vec{r}+\vec{R}) = e^{i\vec{k}\cdot\vec{r}}\psi(\vec{r}) \tag{2.34}$$

for every $\vec{R}$ in the Bravais lattice [91]. It is important to note that this theorem means that it is possible to try and solve the Schrödinger equation independently for each value of $\vec{k}$. This also applies to quantities derived from the solutions to the electron density equations [63].

In carrying out DFT calculations lot of the calculations reduce down to evaluating integrals in the reciprocal space of the form

$$\bar{g} = \frac{V_{cell}}{(2\pi)^3}\int_{BZ} g(\vec{k})d\vec{k} \tag{2.35}$$

that spans over all possible values of $\vec{k}$ in the Brillouin zone (BZ). There have been many attempts at solving equations of this form efficiently and the most popular one (and the one that we have used in our calculations) is the Monkhorst-Pack scheme [92]. To use this in VASP all we need to do is to specify the number of k-points that we want to use in each direction in the reciprocal space. Although it can be expected that the larger the number of k-points the greater the accuracy of our calculations, in practice one needs to use enough k-points to ensure that the energy converges to within 10^{-3} eV. Also, it is important to take the symmetry of the system into consideration so that the calculations can be carried out in a small portion of the zone and then extend to fill the rest of the Brillouin zone. This reduced zone in k space is called the *irreducible Brillouin zone* (IBZ). For example, for a perfect fcc crystal using a $10\times10\times10$ Monkhorst-Pack sampling of the BZ, only 35 distinct points of the k-space that lie within the IBZ need to be used compared to the 1,000 that would need to be used if symmetry was not taken into consideration, thus greatly reducing the computational effort [63].

Other difficulties that are encountered in condensed matter simulations arise due to the fact that the wavefunctions are nearly infinite in extent and because we are confronted with dealing with a very large number of electrons. These issues are dealt with by introducing periodic boundary conditions (PBC) [93] in which a "supercell" is replicated throughout space. We can then use Bloch's theorem (Eq. 2.34) thus allowing the periodic part of the wavefunction $u_{n\vec{k}}(\vec{r})$ to be expanded in a discrete set of plane-waves whose wave vectors are the reciprocal lattice vectors $\vec{G}$ of the crystal structure

$$\psi_{n\vec{k}}(\vec{r}) = e^{i\vec{k}\cdot\vec{r}} u_{n\vec{k}}(\vec{r}) = \sum_{\vec{G}} c_{n,\,\vec{k}+\vec{G}}\, e^{i(\vec{k}+\vec{G})\cdot\vec{r}}. \tag{2.36}$$

Of course it would not be possible to evaluate this summation over all the (infinite) values of $\vec{G}$. We first note that functions in the above equation are solutions to the Schrödinger equation with kinetic energy

$$E = \frac{\hbar^2}{2m}|\vec{k}+\vec{G}|. \tag{2.37}$$

Since solutions with lower energies are physically more important it is prudent to truncate the infinite sum to include only solutions with kinetic energies less than some value

$$E_{cut} = \frac{\hbar^2}{2m} G_{cut}^2. \tag{2.38}$$

where E_{cut} is known as the *cutoff energy*. Then Eq. 2.36 reduces to

$$\psi_{n\vec{k}}(\vec{r}) = \sum_{|\vec{G}+\vec{k}|<G_{cut}} c_{n,\,\vec{k}+\vec{G}}\, e^{i(\vec{k}+\vec{G})\cdot\vec{r}} \tag{2.39}$$

and is more manageable. One important point to note when doing DFT calculations for multiple systems (such as an alloy) is to use the same energy cutoff E_{cut} in all calculations, preferably the one with the highest cutoff energy among the different species.

2.9 Psuedopotentials

With the use of pseudopotentials we can, by treating only the valence electrons, further improve the efficiency and accuracy of planewave-based DFT calculations [94]. In the pseudopotential approximation the electronic potential is separated between a core region and a valence region. The strong core potential that includes the Coulombic attraction, the Hartree

potential due to the core charge, and a component of the exchange-correlation potential related to the valence-core interaction, is replaced by a pseudopotential whose ground state wavefunction φ^{PS} mimics the all electron valence wavefunction outside the selected core radius. Thus, both the core states and the orthogonalization wiggles in the valence wavefunctions are removed [78] as shown in Fig. 2.2. The resulting pseudo-wavefunctions $\varphi^{PS}(r)$ are

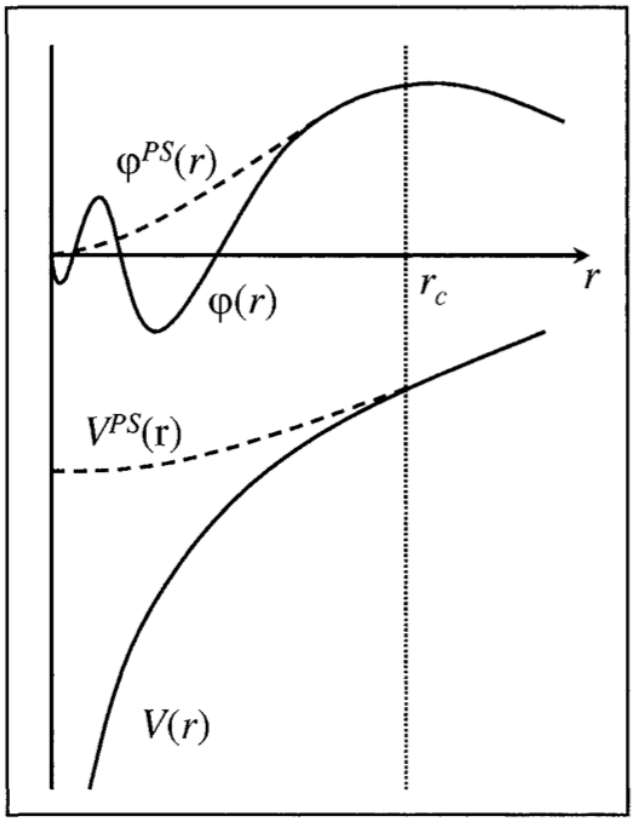

Figure 2.2: Schematics of the replacement of the actual all-electron wavefunction $\varphi(\vec{r})$ and the actual core potential $V(\vec{r})$ by a pseudo-wavefunction $\varphi^{PS}(\vec{r})$ and pseudopotential $V^{PS}(r)$ inside some core radius $\vec{r_C}$. *From Singh and Nordström* [78].

node-less and quite smooth inside some core radius $\vec{r_C}$ for many elements and may be well represented using only a much smaller basis set of $\vec{G}$ planewaves thus saving substantial amount of computational resources.

The main advantages of using pseudopotentials are that a) we need fewer wavefunctions since we are omitting the core electrons and that b) by avoiding the nodes by

using a smooth pseudo-wavefunction for the core region we can expand the wavefunction using far fewer basis functions. The accuracy compromise is negligible since most properties of solids depend on the valence electrons. Additionally, the precision required to determine energy differences for a pseudopotential calculation is much smaller than that for the all-electron calculation. This is because the energy difference between the different ionic and bonding configurations is due to the differences in the valence electrons and since the total energy of the valence-only system is much smaller than the energy of an all-electron system.

The pseudopotentials that we have used in this work are the *ab initio* pseudopotentials, as distinguished from *empirical pseudopotentials* in which pseudopotentials are parametrized by fitting to experimental data, such as a band structure. In generating modern pseudopotentials we have to reconcile some conflicting goals [78]. 1) The pseudopotentials must be as soft as possible, i.e., the valence pseudo-wavefunctions should be expanded using a minimum of planewaves. 2) The pseudopotential must be transferable so that a pseudopotential generated for a given atomic configuration should be useable to other cases, such as dimers, bulk, and surfaces. 3) The pseudo-charge density should reproduce the valence charge density as faithfully as possible. These conflicting goals are greatly alleviated by using the *norm conserving* pseudopotentials [95, 96]. In this scheme the potentials and the pseudo-wavefunctions outside some core radius r_C are constructed to be equal to those of the actual potential and pseudo-wavefunction. Although inside r_C the pseudo-wavefunctions differ from the true wavefunctions, their norm is constrained to be invariant. That is [78],

$$\int_0^{r_C} dr\, r^2 \varphi^{PS\,*}(r)\varphi^{PS}(r) = \int_0^{r_C} dr\, r^2 \varphi^{*}(r)\varphi(r). \tag{2.40}$$

This ensures that the charge density for both all-electron and pseudo-wavefunctions is the same.

2.10 Concluding Remarks

In this chapter we have discussed the essence of the density functional theory. Using DFT we can predict optimal design of materials rather than conducting expensive and time consuming trial and error experimental procedures. As we have discussed in the literature survey in Chapter 1, DFT has been used by others to find bulk properties of ceria in good agreement with experimental data. Density functional theory (DFT) is also a very good first principles tool for calculating oxygen vacancy formation and migration in doped ceria because it yields results that are better than those employing, say, empirical potentials and aspects of it has been been explored by others. In chapter 4 of this dissertation we will discuss in detail the actual implementation of DFT in calculating oxygen vacancy formation and migration in doped ceria and present the results of our calculations.

Chapter 3

DIFFUSION AND IONIC CONDUCTIVITY IN DOPED CERIA

Having discussed the basics of the density functional theory in the last chapter we now discuss the structure and defect structure of ceria and how it affects ionic conduction.

3.1 Structure of Ceria

Cerium with a $4\,f^2 5\,d^0 6\,s^2$ electron configuration can exhibit both the +3 and +4 oxidation states, and intermediate oxides whose composition is in the range $Ce_2O_3-CeO_2$ can be formed[1]. It can be seen from the thermodynamic data presented in Table 3.1 that cerium metal is unstable in the presence of oxygen and that CeO_2 and Ce_2O_3 are easily formed, the final stoichiometry being dependent on temperature and oxygen pressure.

As mentioned earlier, Ceria (CeO_2) crystallizes in the fluorite structure with space group $Fm\bar{3}m$ with $a = 5.4113$ Å. This structure can be regarded as a *ccp* array of cerium ions with eight oxygen ions occupying all the tetrahedral holes for a total of 12 atoms per unit cell (Fig. 3.1). In this structure each cerium cation is coordinated by eight equivalent nearest-neighbor oxygen anions and each anion is tetrahedrally coordinated by four cations. That is, each cerium atom occupies the (0, 0, 0) position in the *fcc* lattice and the oxygen atoms occupy the interstitial positions of the type $(\frac{1}{4}, \frac{1}{4}, \frac{1}{4})$. This structure may also be viewed as a simple cubic oxygen sublattice with the cerium ions occupying alternate cube centers as shown in Fig. 3.2. By redrawing the elementary cell as a primitive cubic array of oxygen ions, in which the eight coordination sites are alternately empty and occupied by a cation, we can clearly see that there are large vacant octahedral holes in the structure. This octahedral holes play a significant role in the movement of ions through the defect structure. In order to discuss the defect structures we first visit the Kröger-Vink notation.

[1]This exposition in this chapter is mainly based on materials from Trovarelli [14], Kilner [97, 98], Stephen and Kilner [33], and Tilley [99].

Table 3.1: Some thermodynamic properties of Ce and Pr oxides. Adapted from Ref. [14].

Reaction	ΔH°_{298} (kJ/mol)	ΔG°_{298} (kJ/mol)	S°_{298} (J/K-mol)
$Ce + O_2 = CeO_2$	-1089	-1025	61.5
$2\,Ce + 1.5O_2 = Ce_2O_3$	-1796	-1708	152
$CeO_{1.5} + 0.25O_2 = CeO_2$	-191	-172	-
$Pr + O_2 = PrO_2$	-958	-899	79.9
$2\,Pr + 1.5O_2 = Pr_2O_3$	-1810	-1735	159
$PrO_{1.5} + 0.25O_2 = PrO_2$	-44	-31.5	-

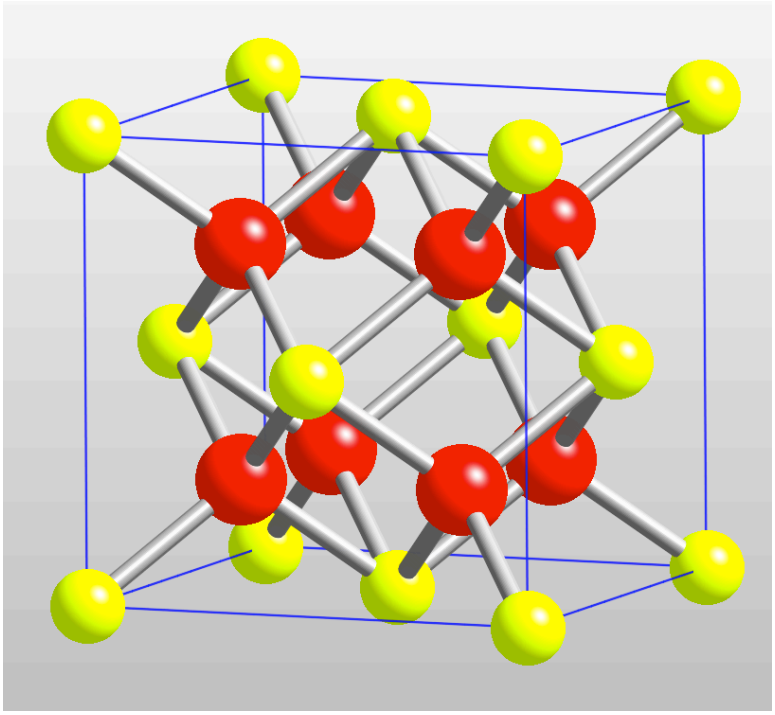

Figure 3.1: CeO_2 unit cell viewed as a *ccp* array of cerium atoms (yellow or light) with eight oxygen atoms (red or dark) occupying the tetrahedral sites. False ionic radii are used for clarity. Model created in CrystalMaker.

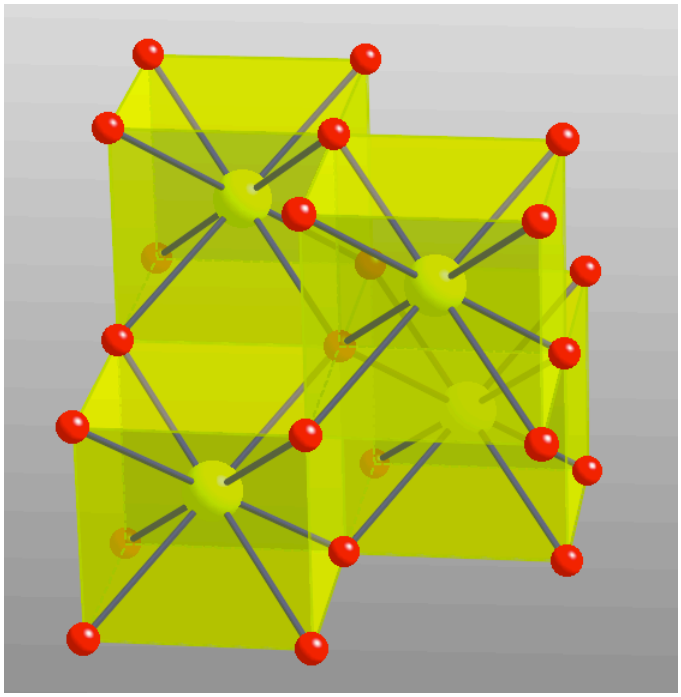

Figure 3.2: CeO_2 unit cell viewed as a primitive array of oxygen ions (red or dark) occupying the eight corners of tetrahedral polyhedra centered on cerium ions (yellow or light colored). False ionic radii are used for clarity. Model created in CrystalMaker.

Kröger-Vink Notation

Point defects fundamentally affect the physical and chemical properties of materials. In order to describe the point defects Kröger and Vink in 1956 developed a set of notations for point defects in crystals, The Kröger-Vink notation [100] facilitates incorporation of defect formation into chemical equations and thus use chemical thermodynamics methods to treat defect equilibria [99]. In the Kröger-Vink notation vacancies are represented by the symbol V. The atom that is missing from a normally occupied site is indicated by a subscript. For example, in CeO_2 the symbol V_O represents an oxygen atom vacancy and V_{Ce} represents a cerium atom vacancy. A defect that has been substituted for another atom in the structure is indicated by a subscript that is the chemical symbol of the atom normally occupying the site occupied by the defect impurity atom. For example, a Pr atom on a Ce site in CeO_2 is written as Pr_{Ce}. Interstitial positions are denoted by a subscript i. If one or more lattice

defects associate with each other, for example a defect in which a vacancy on a metal site and a vacancy on a nonmetal site associate as a vacancy pair then this defect is written as ($V_M V_Y$). These are summarized in Table 3.2.

Table 3.2: Kröger-Vink notation for defects in crystals.

Defect Type	Notation
Metal vacancy at metal (M) site	V_M
Impurity metal (A) at metal (M) site	A_M
Interstitial metal (M)	M_i
Neutral metal (M) vacancy	$V_M^{\times}$
Metal (M) vacancy with negative effective charge	$V_M^{'}$
Interstitial metal (M) with n positive effective charge	$M_i^{n\bullet}$
Free electron	$e^{'}$
Associate pair (vacancy pair)	$(V_M V_Y)$

Adapted from Ref. [99].

3.2 Defect Structure in Ceria

Defects in ceria can be of the intrinsic or the extrinsic type. Intrinsic defects can arise from thermal disorder or from redox type reactions. There are three types of thermally generated defects [14], one is of the Schottky type (Eq. 3.1) and the other two are of the Frenkel types (Eq. 3.2 and 3.3), here represented using the Kröger-Vink notation discussed above, with ΔE values from Ref. [101].

$$Ce_{Ce} + 2O_o \leftrightarrow V_{Ce}^{''''} + 2V_O^{\bullet\bullet} + CeO_2 \qquad \Delta E = 3.53\ \text{eV} \tag{3.1}$$

$$Ce_{Ce} \leftrightarrow Ce_i^{\bullet\bullet\bullet\bullet} V_{Ce}^{''''} \qquad \Delta E = 11.11\ \text{eV} \tag{3.2}$$

$$O_O \leftrightarrow O_i^{''} + V_O^{\bullet\bullet} \qquad \Delta E = 3.2\ \text{eV} \tag{3.3}$$

where O_O and Ce_{Ce} represent oxygen and cerium at their respective lattice sites, $V_O^{\bullet\bullet}$ indicates an oxygen vacancy, $V_{Ce}^{''''}$ indicates a cerium vacancy, $Ce_i^{\bullet\bullet\bullet\bullet}$ represents a cerium ion in an interstitial position, and $O_i^{''}$ represents an oxygen ion in an interstitial position. The effective charge (that is, the charge expressed in terms of the charge normally present in

the same position in the host lattice) is indicated by a dot (•) for each positive charge and a prime ($'$) for each negative charge. In this case, O_i'' indicates a doubly negative oxygen interstitial and $V_O^{\bullet\bullet}$ indicates a doubly positive-charged oxygen vacancy.

From variations in ΔE we can see that the predominant defect category is the anion Frenkel type (Eq. 3.3) that leads to the formation of pairs of oxygen vacancies and oxygens in interstitial positions. Although these defects are generally present in low concentrations and do not much alter the stoichiometry, exposure to reducing gaseous atmospheres can produce high defect concentrations in ceria. Upon reduction CeO_2 has excess metal composition compared to its anion content and the main way that it can accommodate the variation in composition is by the oxygen vacancy method [38]. In this method oxygen vacancies compensate the holes formed on reduction. If the oxygen is removed, the bulk material ends up with an overall positive charge. Therefore, two electrons need to be introduced for each removed oxygen ion in order to retain the charge neutrality of the crystal. These electrons are associated with two cerium atoms that changes the charge from +4 to +3. The effective charge of the anion vacancies is positive, thus neutralizing the negatively charged holes and the process is represented by [14]:

$$CeO_2 \leftrightarrow CeO_{2-x} + \frac{x}{2}O_2(g) \qquad (x < 0.5). \tag{3.4}$$

The oxygen vacancies are mobile at elevated temperatures making ceria an excellent oxygen ion conductor. In neodymium doped ceria, the charge compensation that occurs upon solution of the lower valent oxide, in which Nd added to CeO_2 results in the formation of material with the general formula $Ce_{1-x}Nd_xO_{2-x/2}$ is given by

$$Nd_2O_3 \xrightarrow{CeO_2} 2Nd'_{Ce} + 3O_O^{\times} + V_O^{\bullet\bullet}. \tag{3.5}$$

Thus, for doped ceria, the concentration of vacancies depends primarily on the concentration of ionized dopants. For Nd, $V_O^{\bullet\bullet} \approx \frac{1}{2}Nd'_{Ce}$. Although the generic formula for the reduced phases is CeO_{2-x}, at low temperatures these phases show ordering of oxygen vacancies in a regular fashion, generating a homologous series of phases which have compositions of the form Ce_nO_{2n-2m} [14].

3.3 Conduction in Ceria

The use of materials as solid oxide electrolytes depends on transport properties such as the electrical conduction and oxygen diffusion of such oxides. The conduction and diffusion are determined by the concentration and mobility of lattice defects. The total electrical conductivity in a solid σ_t is the sum of the conductivities of each of the charge carriers present in the solid:

$$\sigma_t = \sum_j \sigma_j \tag{3.6}$$

where the charge carriers may be electronic (electrons, e, or holes, h) or atomic (cation or anion defects). The conductivities of each of these species is given by

$$\sigma_j = n_j q_j \mu_j \tag{3.7}$$

where σ_j is the partial conductivity measured in Scm^{-1} (1 Siemens = 1 ohm^{-1}, n_j is the carrier concentration(per cm^3), q_j is the charge (Coulombs), and μ_j is the mobility (cm^2/Vs).

Ceria is a mixed conductor showing both electronic and ionic conduction and its properties are strongly dependent on temperature, on oxygen partial pressures, and on the presence of dopants or impurities. All of these affect the charge carrier concentrations, and this together with the carrier mobility determines electrical conductivity. In cerium oxide electronic conduction does not happen through the band model but occurs instead through the formation of small polarons [26] where the electron is self-trapped at a given lattice site (Ce^{3+}) and can move only to an adjacent site by an activated hopping process similar to ionic diffusion [14]. This strongly reduces electron mobilities and can be two orders of magnitude less than the ionic mobility. This is what makes doped ceria an ideal candidate for use as the electrolyte in SOFCs where we want to maximize the ionic conductivity through the electrolyte but want minimal electronic conductivity so that most of the electronic conduction takes place through a circuit driving an external load.

From the Arrhenius expression for the ionic conductivity[2]

$$\sigma = \frac{\sigma_o}{T} \exp\left(\frac{-E_a}{k_B T}\right) \tag{3.8}$$

we see that two parameters determine the ionic conductivity. One is the pre-exponential factor σ_o and the other is the activation energy E_a. The activation energy is a very important factor since at low activation energies we can sustain high ionic conductivities at lower temperatures. The activation energy E_a consists of two parts, the enthalpy of migration for the oxygen vacancy, ΔH_m, and another term ΔH_a due to the interaction of the vacancy with other point defects. Kilner [98] says that for dilute solutions of the trivalent cation the interaction term may be due to the formation of defect associates, or dimers, of the oxygen vacancy with the solute cation of the type, for example for Nd-doped ceria:

$$\mathrm{Nd}'_{\mathrm{Ce}} + \mathrm{V}_{\mathrm{O}}^{\bullet\bullet} \leftrightarrow (\mathrm{Nd}'_{\mathrm{Ce}}\mathrm{V}_{\mathrm{O}}^{\bullet\bullet})^{\bullet} \qquad \Delta H_a \tag{3.9}$$

Kilner points out that for the simple associated defect pair shown above the concentration of ionized cations is double that of the oxygen vacancies produced. He asserts that this means there is a high probability of forming large clusters as the solute concentration increases. If only simple associated pairs were formed then $E_a = \Delta H_a + \Delta H_m$.

Faber et al. [102] determined the activation energy of conduction as a function of dopant cation concentration in ceria solid solutions with trivalent rare earths. They found that there is a minimum in the activation energy E_a for conduction (Fig. 3.3) that depends on the nature of the rare earth solute and attributed this to the type of interactions between the dopant cation and the mobile oxygen vacancies [14]. Kilner [98] cites Wang et al. [103] as explaining the minima by the interplay of competitive defect interactions. In the dilute range (solute concentrations $\approx 1\%$) there is a weakening of the association energy due to Coulombic interactions between the associated pair and the unassociated solute cations, which have opposite effective charges in the lattice. In the high concentration range they

[2]This equation is sometimes written as $\sigma = \sigma_o \exp\left(\frac{-E_a}{k_B T}\right)$ in which case the temperature T is incorporated in the pre-exponential factor. However, the form presented in Eq. 3.8 is preferred because it explicitly shows the temperature dependence of the pre-exponential factor.

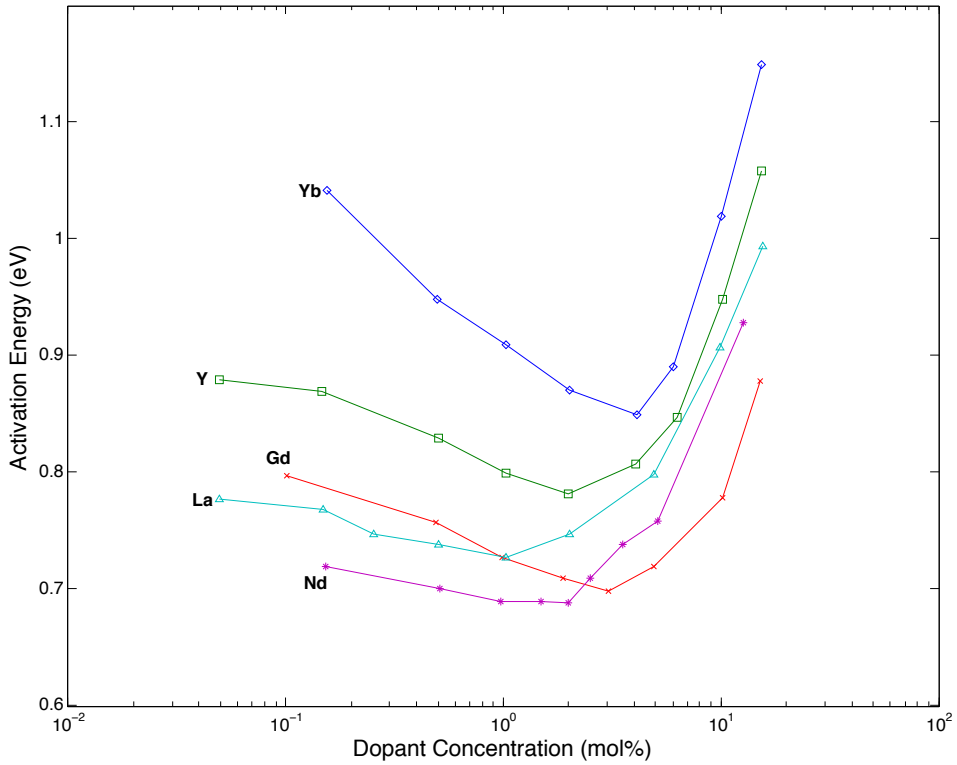

Figure 3.3: Concentration dependence of the activation energy for oxygen ion conduction in ceria solid solutions. Data from Ref. [102].

attributed the increase in E_a, and the associated decrease in the conductivity σ, to the presence of vacancy traps (of large clusters) that limit vacancy mobility, thus rendering the concept of free vacancy invalid at high dopant concentrations. By analyzing the data of Faber et al. and Wang et al., Kilner found that there is actually a global minima that is dependent on both solute size and concentration (Fig. 3.4). From this he concluded that the association energy must contain two terms, 1) a Coulombic term that reflects the electrostatic attraction between the components (that is independent of the solute type) and 2) an elastic term representing the size mismatch of the solute with the host lattice.

Minervini et al. [101] carried out atomistic simulations[3] based on energy minimization techniques (with a Born-like description of the lattice to generate the various structures)

[3]In their procedure Minervani et al. created a crystal structure using periodic boundary conditions an then minimized the total energy by allowing the ions in the unit cell and the lattice vectors to relax to zero strain.

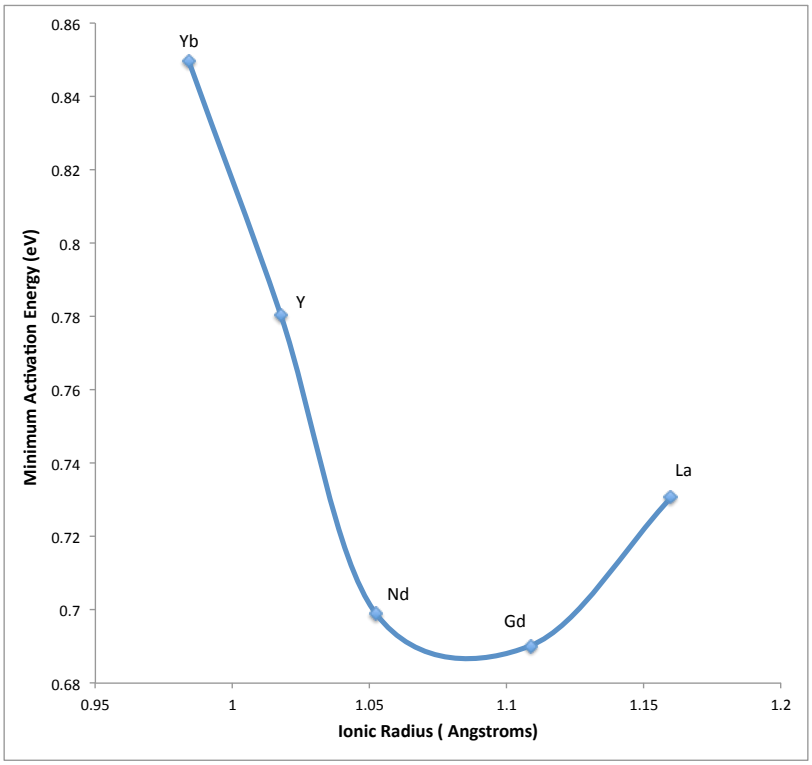

Figure 3.4: Minimum activation energy for each ceria solid solution plotted against ionic radius of the solute. From Ref. [98].

to understand the minimum near Gd^{3+} in activation energy with the ionic radius in Fig. 3.4. Their results showed that the binding energy of an oxygen vacancy to one or two substitutional cations is a strong function of dopant cation radius. That is, small dopant ions prefer to occupy first neighbor sites, large dopant ions prefer second neighbor sites and that this crossover happens near Gd^{3+}, thus confirming the finding by Kilner. Andersson et al. [1] used density functional theory and found confirmation of this solute size trend for ceria, and have found that the energy difference for the vacancy between the first and the second neighbor sites is minimal. They explained that this is because of a balancing act in the optimal electrolyte between the repulsive elastic and the attractive electronic interactions. Andersson et al. concluded that the ideal dopant should have an effective atomic number between 61 (Pm) and 62 (Sm), and that codoped combinations such as Nd/Sm and Pr/Gd have higher conductivity as compared with that for each element alone.

Dholabhai et al. [8] using density functional calculations also confirmed the correspondence between the dopant radius and the binding energy of the oxygen vacancy. For example, for Pr-doped ceria, where the Pr^{3+} has an (eight-coordinated) ionic radius[4] of 1.266 Å that is much larger than Ce^{4+} (1.11 Å), they found that the second nearest neighbor site to be the most favorable vacancy formation site. On the other hand, in another DFT study Dholabhai et al. [7] report that due to the comparable (eight-coordinated) ionic radii of Gd^{3+} (1.193 Å) and host Ce^{4+} (1.11 Å) ions, the first nearest neighbor site with respect to the dopant cation is the most favorable oxygen vacancy formation site.

3.4 Conclusion

In this chapter we have discussed the structure of ceria and pointed out that the large octahedral holes in this structure play significant role for ionic diffusion. We have also discussed the defect structure of ceria and have discussed how the introduction of dopants creates vacancies in the structure. These vacancies facilitates ionic conductivity through doped ceria.

[4] All ionic radii mentioned here are the Shannon ionic radii for 8-coordinate M(III) ions, except for Ce which is an 8-coordinate M(IV) ion, as listed in `webelements.com`. The ionic radii given in Kilner [98], on the other hand, are 0.97 Å for Ce^{4+}, 1.11 Å for Gd^{3+}, and 1.05 Å for Nd^{3+}.

Chapter 4

DENSITY FUNCTIONAL THEORY CALCULATIONS USING VASP

In earlier chapters we have discussed the density functional theory and the role that it plays in designing materials with optimal properties. In this chapter we discuss the implementation of the DFT code in detail and discuss how we have used it to calculate the properties of pure ceria and neodymium doped ceria, We also compare our results with those of others.

4.1 The VASP Code

In order to calculate the activation energies of ceria and doped ceria we have carried out the DFT calculations using the Vienna Ab-initio Simulation Package[1] (VASP) which is a software package developed by researchers in the Universität Wien, Austria for performing *ab initio* quantum-mechanical molecular dynamics (MD) simulations using pseudopotentials or the projector-augmented wave method and a plane wave basis set [104–107]. Here we reproduce the salient points of the VASP software as described in the VASP manual.

> The Vienna Ab initio Simulation Package (VASP) is a computer program for atomic scale materials modelling, e.g. electronic structure calculations and quantum-mechanical molecular dynamics, from first principles.
>
> VASP computes an approximate solution to the many-body Schrödinger equation, either within density functional theory (DFT), solving the Kohn-Sham equations, or within the Hartree-Fock (HF) approximation, solving the Roothaan equations. Hybrid functionals that mix the Hartree-Fock approach with density functional theory are implemented as well. Furthermore, Green's functions methods (GW quasiparticles, and ACFDT-RPA) and many-body perturbation theory (2nd-order Møller-Plesset) are available in VASP.
>
> In VASP, central quantities, like the one-electron orbitals, the electronic charge density, and the local potential are expressed in plane wave basis sets. The interactions between the electrons and ions are described using

[1] `http://cms.mpi.univie.ac.at/marsweb/`

norm-conserving or ultrasoft pseudopotentials, or the projector-augmented-wave (PAW) method.

To determine the electronic ground state, VASP makes use of efficient iterative matrix diagonalization techniques, like the residual minimization method with direct inversion of the iterative subspace (RMM-DIIS) or blocked Davidson algorithms. These are coupled to highly efficient Broyden and Pulay density mixing schemes to speed up the self-consistency cycle.

To reiterate, the single particle Kohn-Sham wavefunctions are expanded using plane-wave basis sets in VASP. Pseudopotentials, as discussed above, are used to approximate the computationally expensive electron-ion interactions [108]. The use of ultra-soft Vanderbilt pseudopotentials (US-PP) or the projector-augmented wave (PAW) method allows for a considerable reduction of the number of plane-waves per atom for transition metals and first row elements. Forces and the full stress tensor can be calculated with VASP and used to relax atoms into their instantaneous ground-state. Because of this implementation, the VASP manual claims, no more than 100 plane waves (PW) per atom are required to describe bulk materials and in most cases even 50 PW per atom are sufficient for a reliable simulation.

The VASP program requires a number of input files that the user has to specify in order to initiate density functional calculations. Four of these input files are critical for carrying out the DFT calculations for ceria and doped ceria systems. They are the POSCAR, POTCAR, KOINTS, and the INCAR files and are shown schematically in Fig. 4.1.

1. The POSCAR file contains structural information such as the Bravais lattice vectors and the coordinates of the atoms.
2. The POTCAR file contains the description of the pseudopotentials and is generated by concatenating the individual species pseudopotential files from a data base, making sure the species are in the same order as in the POSCAR file. The information contained in this file are the atomic masses, the required cutoff energies, the number of valance electron of each species, and it is used to generate the potential.

3. The KPOINTS file tells how many k-points are needed to sample the Brillouin zone and what scheme are used.
4. The INCAR file basically steers the entire job. It specifies what approximations and what level of theory to use.
5. Additionally there are computer architecture dependent script files that one needs to create and run.

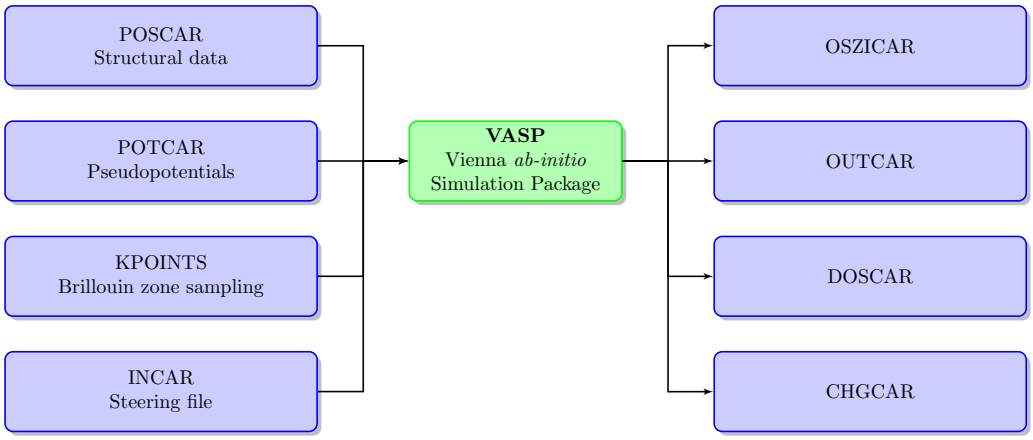

Figure 4.1: The input files necessary to run the VASP program and four of the output files generated by it.

The code generates a large number of output files, among them the most relevant ones for my work are the OSZICAR, OUTCAR, DOSCAR, and CHGCAR files. The OSZICAR file keeps track of the last few iterations of the run in its attempt to arrive at convergence of the total energy. It lists the iteration count N, the total energy E_{Tot}, the change in total energy dE, the change in the eigenvalues $d(eps)$, and the charge density residual vector, among other items. The CHGCAR file contains information such as the lattice vectors, atomic coordinates, and the total charge density multiplied by the volume $\rho(\vec{r}) \times V_{cell}$. The DOSCAR file contains the density of state (DOS) and the integrated DOS in units of "number of states per unit cell". The OUTCAR file is the main output file. The type and volume of information in it is controlled by the tags that we put in the INCAR file. It keeps detailed track of all the calculations.

4.2 Methodology

In this work all calculations were performed using the VASP code by carrying out the spin-polarized calculations within the generalized gradient approximation (GGA) to density functional theory (DFT) [69] with the Perdew-Burke-Ernzerhof (PBE) exchange-correlation functional [76]. The PBE is one of the widely used non-empirical GGA functionals. It is a "hybrid" functional that mixes the exact results for the exchange part of the functional with approximations of the correlation part and it is useful for DFT calculations of spatially localized basis functions (atomic orbitals).

Strong Coulomb correlation of the localized Ce $4f$ electrons preclude standard DFT methods using GGA or local density approximation to adequately predict the electronic structure [16, 39, 43, 109–116]. To address this we have applied the rotationally invariant form of GGA+U, which is a combination of the standard GGA and a Hubbard Hamiltonian for the Coulomb repulsion and exchange interaction as formulated by Dudarev et al. [84] to account for the strong on-site Coulomb repulsion amid the localized Ce $4f$ electrons. In the GGA+U method, if the $4f$ levels are partially filled, the potential is attractive and promotes the on-site $4f$ electrons to be localized and the material is then properly identified as insulating instead of metallic [113, 117, 118]. In the DFT+U method as formulated by Dudarev et al. [84], a correction to the DFT energy is introduced to correct for the electron self-interaction. This is done by introducing a single numerical parameter $U_{eff} = U - J$ where U is the Coulomb self-interacting (repulsive) term and and J is the exchange self-interaction term. We reiterate that U and J do not enter separately, but only the difference U_{eff} is meaningful. The choice of U_{eff} is decided and usually fitted to recover the experimentally measured parameters, for instance, band gap, magnetic moment, and structural properties. For example, the bulk modulus of a perfect crystal can be calculated and the value of $U - J$ that gives the best fit to the known bulk modulus is determined.

In order to determine the optimal value of the parameter U_{eff}, we performed static bulk calculations by varying U_{eff} from 0 to 6 eV. For different U_{eff} values, we compared

the bulk modulus (B_o), lattice constant (a_o), and electronic band gap (E_{gap}) with the experimental values. $U_{eff} = 0$ represents the GGA limit. We found that with increasing U_{eff} the lattice parameter a_o deviates further from the experimental value, but the B_o and E_{gap} approaches the experimental limit. Others have reported similar behavior of these parameters [16, 119]. For reduced ceria, which is the focus of the current work, we find using Bader analysis [120] that for U_{eff} = 5 eV, the $4f$ electrons are completely localized on two Ce ions near the oxygen vacancy and the electronic structure is converged. This is reasonable because then the material can properly be identified as insulating instead of metallic. As pointed out by Dholabhai et al. [8] this shows a significant improvement in the description of Ce $4f$ electrons as GGA ($U_{eff} = 0$) applied to reduced ceria shows that the Ce $4f$ electrons are delocalized over all the cerium ions [16, 39, 43, 109–116]. Also, this value of U_{eff} = 5 eV has been used within the GGA+U formalism by others for studying ceria and doped ceria [43, 44, 111, 121–123]. Therefore, the chosen U_{eff} value of 5 eV is optimal in modeling ceria related materials in the GGA+U formalism and we expect the total energies obtained for these materials to be very accurate.

The strongly oscillating wavefunctions were solved using a plane wave basis set using the projected augmented wave (PAW) approach [124, 125]. The PAW method reproduces the effect of the core electrons on the valence electrons, with [He] core for oxygen and [Xe] cores for cerium and neodymium. For neodymium, the $4f$ electrons were treated as part of the core (core state model), therefore, no empirical U_{eff} parameter for the $4f$ electrons of Nd was necessary. The Broyden mixing scheme [126] was used to calculate energies and charge densities self-consistently. We used a plane-wave cutoff energy of 400 eV, which converged the energies to approximately 0.01 meV. Block Davidson [127] minimization algorithm was used that led to a convergence in total energies of the order of 0.01 meV/atom or better. Ground state geometries of different systems were obtained by minimizing the Hellman-Feynman [128, 129] forces until the total forces on each atom were less than 0.02 eV/Å. The irreducible Brillouin-zone integrations were performed using Monkhorst-Pack (MP) [92] grids with a Gaussian smearing of 0.1 eV. We conducted a convergence test for pure ceria to determine the viability of the chosen MP grid. A MP

grid of $2 \times 2 \times 2$ was deemed to be optimal for maintaining a balance between accuracy and computing efficiency.

4.3 VASP Calculations for Pure Ceria

In order to verify the validity of the methodology before carrying out simulations on doped ceria, calculations were carried out using VASP to determine the equilibrium lattice constant for pure ceria.

To create the bulk structure, I created a new ceria structure with space group $Fm\bar{3}m$ using the experimental lattice constant of 5.411 Å in the CrystalMaker software. I placed the Ce and O atoms in the following sites as in Table 4.1. This created a structure whose 12

Table 4.1: CeO structure. Spacegroup = $Fm\bar{3}m$. Lattice constant = 5.411 Å.

Species	Site occupancy	x	y	z
Ce	Ce 1	0	0	0
O	O 1	0.25	0.25	0.25

fcc sites are occupied by cerium (Ce) atoms and 8 tetrahedral sites are occupied by oxygen (O) atoms. This gives us the fluorite structure. Since the fcc structure has 4 atoms within the unit cell and we have 8 extra atoms in the tetrahedral sites, the CeO_2 fluorite structure has 12 atoms in each unit cell (Fig. 1.3 and 1.4).

In VASP we used a $1 \times 1 \times 1$ CeO_2 supercell consisting of 12 atoms (4 Ce and 8 O atoms). In order to get good convergence (of 0.01 meV or better) a $12 \times 12 \times 12$ K-points grid was used. The optimized $U_{eff} = 5$ eV was used for the calculations. The atomic positions of the twelve atoms was calculated by hand and verified using the CrystalMaker software. The resulting POSCAR file for VASP is given below and the INCAR file is given in the appendix.

```
1 fcc CeO2 supercell
2 5.44
3 1.0 0.0 0.0
4 0.0 1.0 0.0
```

```
5 0.0 0.0 1.0
6 4 8
7 direct
8 0.5000  0.5000  0.0000
9 0.5000  0.0000  0.5000
10 0.0000  0.5000  0.5000
11 0.0000  0.0000  0.0000
12 0.7500  0.2500  0.7500
13 0.2500  0.2500  0.7500
14 0.2500  0.7500  0.2500
15 0.7500  0.7500  0.7500
16 0.7500  0.2500  0.2500
17 0.2500  0.2500  0.2500
18 0.2500  0.7500  0.7500
19 0.7500  0.7500  0.2500
```

In this file the first line is the comments line, the second line gives an initial lattice parameter. This parameter was systematically varied from 5.40 to 5.58 Å in increments of 0.01 Å. The third through fifth lines are the three Bravais lattice vectors. Line 6 declares the number of cerium and oxygen atoms in the supercell. Line 7 tells VASP that the coordinates in the following lines are given in direct (Cartesian) coordinates that are to be scaled by the lattice parameter declared in line 2. The coordinates of lines 8–11 are for the four cerium atoms and lines 12–19 are for the oxygen atoms. It is important that the order of these species be the same as those in the pseudopotentials POTCAR file. Our simulations with a U_{eff} value of 5 eV resulted in a structure with a lattice constant of $a_o = 5.494$ Å (Fig. 4.2), bulk modulus of 185.2 GPa, $E_{gap}[\mathrm{O}(2p) \rightarrow \mathrm{Ce}(4f)] = 2.06$ eV (experimental value is ~ 3 eV), and $E_{gap}[\mathrm{O}(2p) \rightarrow \mathrm{Ce}(5d)] = 4.99$ eV (Fig. 4.3). Our lattice constant value is in reasonable agreement with the measured value of $a_o = 5.411$ Å by Eyring [130]. Our Bulk modulus is also in good agreement with the room temperature value of $B_o = 187$ GPa calculated by Gerward et al. [131] obtained by X-ray diffraction. These latter authors also report a computed value of $B_o = 176.8$ GPa using self-interaction corrected local spin density (SIC-LSD) approximation, a value very close to our DFT+U value. These calculated values are in reasonable agreement with the measured values of $a_o = 5.411$ Å [130] and B_o = 220 GPa at room temperature [131]. In the projected density of states

(Fig. 4.3) the band found between -20 eV and -10 eV below the valence band is a result of the interactions between cerium $5p$ and oxygen $2s$ states. The valence band is composed of oxygen $2p$ states with some contributions from Ce $5d$ and $4f$. Above the valence band we find a narrow unoccupied band from Ce 4f and the conduction band that is made up of Ce $5d$ states. This projected density of states reproduces the one reported using DFT+U by Dholabhai et al. [8] and by Nolan et al. [111]. It is also similar to that reported by by Hill and Catlow [132] who used the restricted Hartree-Fock method using the CRYSTAL software. For CeO_2 increasing U primarily pushes up the unoccupied f band and slightly decrease the band gap, as was also observed by Jiang et al. [16]. We conclude that a U_{eff} value of 5 eV represents a good fit for reproducing the experimental data.

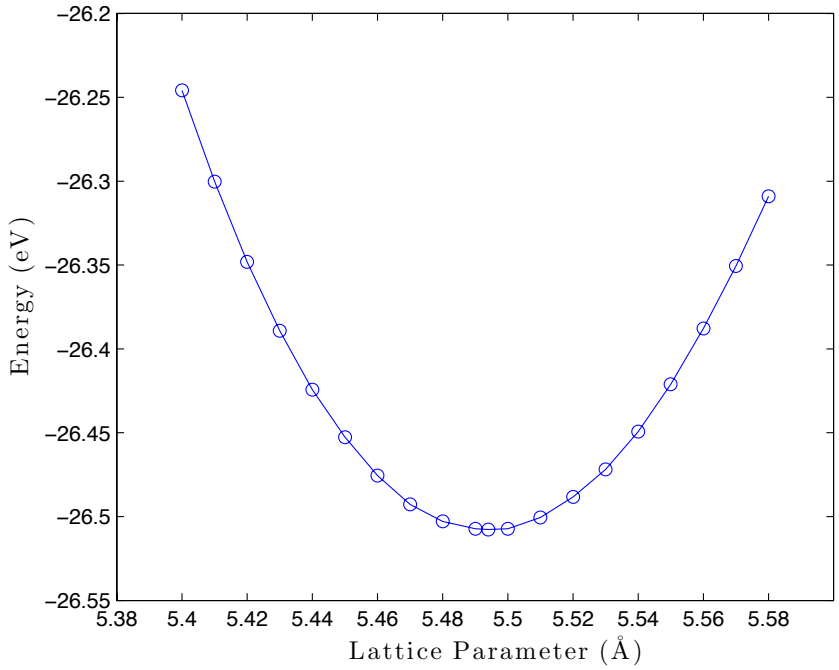

Figure 4.2: Optimization of the lattice parameter of pure ceria using a Birch-Murnaghan fit for data obtained by carrying out DFT+U calculations on pure ceria with and effective U parameter of 5 eV. The optimized lattice parameter calculated for CeO_2 is 5.494 Å.

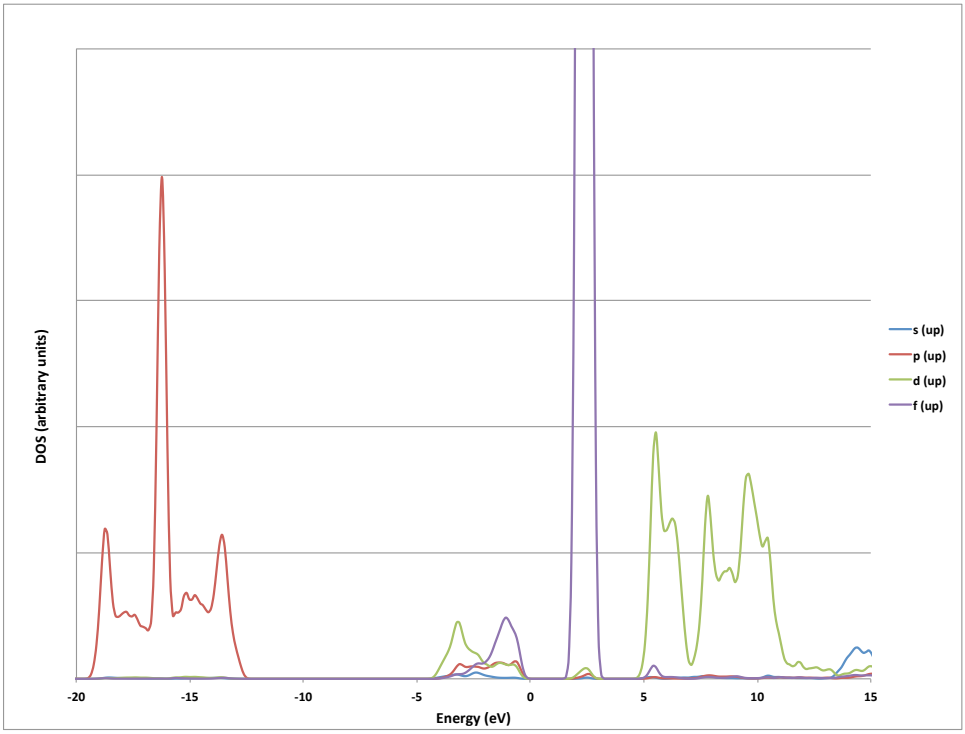

Figure 4.3: Projected density of states for CeO_2 obtained with GGA+U for $U_{eff} = 5$ eV. The low-lying Ce 5s states found at energy of -33 eV are not included in the plot. Only spin-up channel is shown. The zero of energy is set to the top of the valence band.

4.4 VASP Calculations for Nd-doped Ceria

As mentioned earlier we found that a Monkhorst-Pack grid of $2 \times 2 \times 2$ was optimal for maintaining a balance between accuracy and computing efficiency. Therefore, I created a $2 \times 2 \times 2$ slab (supercell) of pure ceria (CeO_2) consisting of 96 atoms in CrystalMaker and used it to create the POSCAR file for VASP (included in the Appendix). We used a periodic supercell model [133]. In this model, periodic boundary conditions are applied and all interactions are periodic with the periodicity of the supercell. The 96-atom supercell consists of 32 cerium and 64 oxygen atoms consisting of eight elementary unit cells of CeO_2) with a $2 \times 2 \times 2$ periodicity built from a conventional 12-atom cubic unit cell of ceria. We used the theoretically optimized lattice constant of 5.494 Å for bulk ceria to construct the supercell. In this 96-atom supercell, the vacancy-vacancy and the dopant-

dopant interactions are small. This type of supercell has also been previously used by others to simulate ceria, reduced ceria, and reduced ceria with dopants [1,16,43,44,109,121,134].

Care must be used when creating the supercell in CrystalMaker. From the Transform menu of CrystalMaker we defined a $2 \times 2 \times 2$ super cell consisting of 8 unit cells. This should consist of 96 ($= 8 \times 12$) atoms in the super cell. However, CrystalMaker lists 127 coordinates because it also lists the equivalent coordinates at the edges. To get the correct number of atomic coordinates within the super cell we reduced the range of the cells slightly (by setting the three axial range limits from 0 to 0.99) in order to remove the edge atoms. This gave us the correct 96 atoms *in* the super cell. Selecting "List Coordinates" from the Transform menu gives us both the fractional and orthogonal coordinates of the the 96 atoms. We copied the fractional coordinates to our POSCAR file in VASP. It is important to note here that since we are now expressing each of the lattice coordinates we are not using the crystal symmetry any more. In VASP we need to explicitly define the fractional atomic coordinates along with the lattice parameter.

We optimized the pure ceria supercell with respect to the lattice parameter and atomic positions. The pure ceria system after optimization did not show any signs of relaxation and the 96 atoms retained their positions in the supercell. The neodymium doped ceria (NDC) was simulated by substituting two Ce ions with two trivalent Nd ions, corresponding to a dopant concentration of 6.25% (2 of 32 atoms). Reduced ceria and reduced NDC was simulated by removing an oxygen ion to create an oxygen vacancy concentration of approximately 1.56% (1 of 64 atoms).

Two Nd^{3+} ions compensate for each oxygen vacancy thus maintaining the charge neutrality of the slab. The doped systems were optimized with respect to cell parameter as well as atomic positions. We first calculated the total energy of the system before the migration of an oxygen ion and then calculated the total energy after placing an oxygen atom at the saddle point. The difference of these two energies yielded the activation energy.

The saddle point position is the midpoint between the initial and final position after migration. After placing the ion at the saddle point we allowed it to relax in the plane

perpendicular to the migration path. We then used small variations to the saddle point position in order to ascertain that the midpoint was indeed the true maximum energy point.

4.5 Nd-doped Ceria Results

In doped ceria we can place the oxygen vacancy in several possible sites. These sites that are of interest to us are the first nearest neighbor (1NN), second nearest neighbor (2NN), and the third nearest neighbor (3NN) sites as shown in Fig. 4.4. We have determined that the contribution of sites further away has negligible contribution to the activation energies. In order to retain charge neutrality we have to introduce two Nd^{3+} ions for each oxygen vacancy created. Once the oxygen vacancy position was selected, we then placed a second dopant atom far away from the first one and more than 3NN distance from the oxygen vacancy so that we could investigate the effect of a single dopant toward the vacancy migration energy. We will later investigate the effect of placing two dopant atoms in nearby sites.

There are nine different migration paths for an oxygen vacancy located in 1NN, 2NN, or 3NN sites in neodymium doped ceria. These paths are (1NN $\rightarrow$ 1NN), (1NN $\leftrightarrow$ 2NN), (1NN $\leftrightarrow$ 3NN), (2NN $\rightarrow$ 2NN), (2NN $\leftrightarrow$ 3NN), (3NN $\rightarrow$ 3NN). We have studied oxygen vacancy migration for these nine different paths in the $< 100 >$, $< 110 >$, and $< 111 >$ directions. We have only reported the first and second nearest neighbor migration paths since they have the lowest energy barriers. The results for oxygen vacancy migration along different pathways in neodymium doped ceria (NDC) are tabulated in Table 4.2.

Oxygen vacancies were introduced in the pure ceria structure by removing the relevant oxygen coordinates lines of the POSCAR file in VASP. We created the vacancies at the 1NN, 2NN , and 3NN positions (with respect to the dopant) in Nd-doped ceria. We found that the 1NN position is the most favorable. This is consistent with the reported values in Ref. [1]. It is important to note here that the ionic radius definitely plays a role in determining the most favorable vacancy formation site. Dholabhai et al. [8] had reported that for praseodymium doped ceria the 2NN site was the favored vacancy formation site since

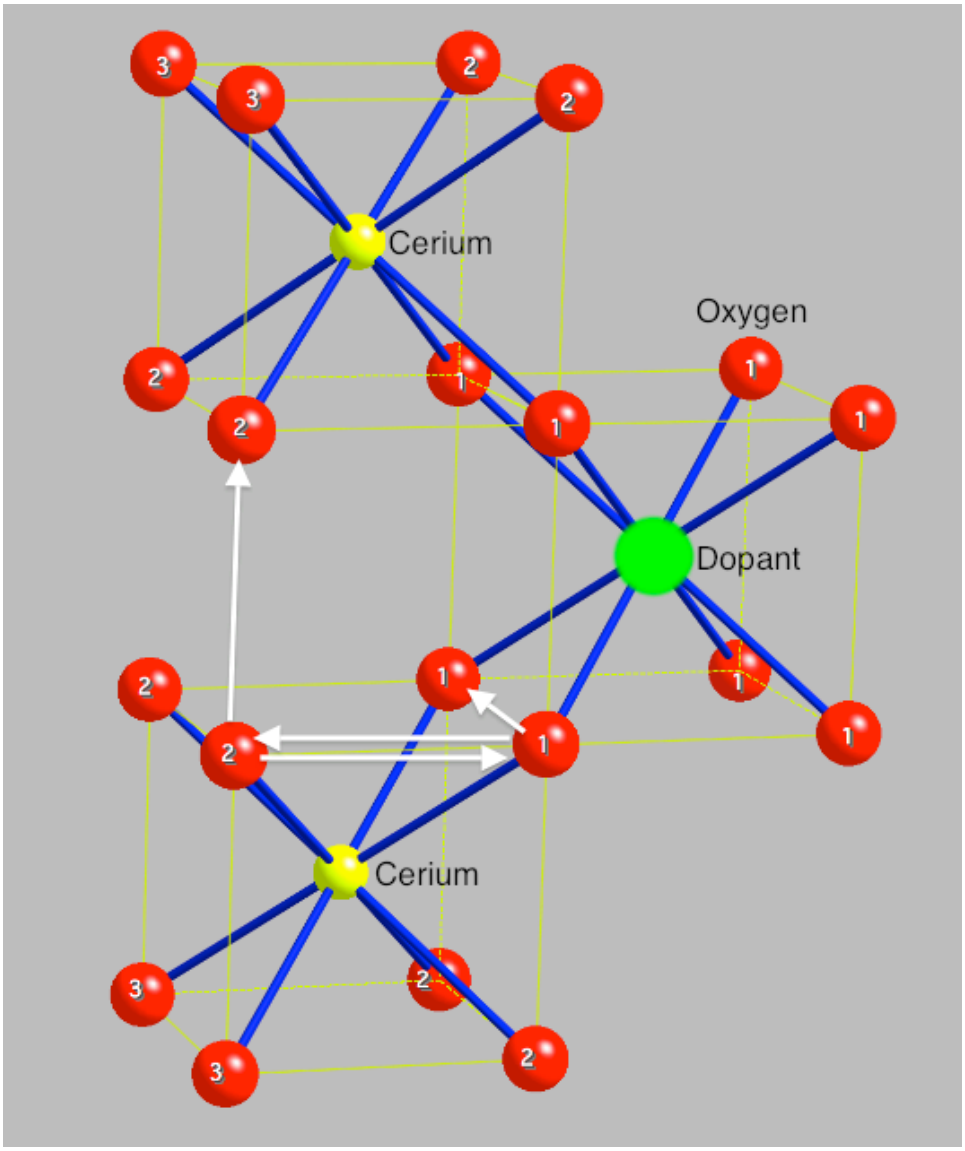

Figure 4.4: Nearest neighbor sites to a neodymium dopant. The yellow balls represent the cerium atoms, the red balls the oxygen atoms, and the green ball the neodymium atom. The oxygen atomic sites are labelled according to their distance from the Nd site. The oxygen ion from the different sites are shown with the white arrows and labelled accordingly. Some jumps, such as the (3,1) and (1,3) jumps, are not shown for clarity.

Table 4.2: Activation energies (E_a) for oxygen vacancy migration in ceria and for different pathways in neodymium doped ceria (NDC). E_{Bulk} is the activation energy for bulk diffusion in ceria and $E_{(m,n)}$ is the activation energy of an oxygen atom to migrate from a site mNN to a site nNN in the doped ceria. NN $\equiv$ nearest neighbor. $< hkl >$ is the vector direction between the initial and final positions of a migrating vacancy. Activation energies quoted correspond to the vector direction for oxygen vacancy.

Migration pathway	Oxygen vacancy migration direction	E_a (eV)
$E_{(\text{Bulk})}$	$<$ **100** $>$	0.47
$E_{(1,1)}$	$<$ **100** $>$	0.73
$E_{(1,2)}$	$<$ **100** $>$	0.44
$E_{(1,3)}$	$<$ **110** $>$	2.77
$E_{(2,1)}$	$<$ **100** $>$	0.43
$E_{(2,2)}$	$<$ **100** $>$	0.47
$E_{(2,3)}$	$<$ **100** $>$	0.55
$E_{(3,1)}$	$<$ **110** $>$	2.66
$E_{(3,2)}$	$<$ **100** $>$	0.45
$E_{(3,3)}$	$<$ **100** $>$	0.47

the large Pr^{3+} ionic radius (1.266 Å) makes it unfavorable for an oxygen vacancy to form at the 1NN site. On the other hand, in another paper [7] they reported that for gadolinium doped ceria the 1NN site is favored because the Gd^{3+} ionic radius (1.193 Å) is much closer to that of the Ce^{4+} ion (1.110 Å). The Shannon ionic radius of Nd^{3+} (1.249 Å) is closer to Ce^{4+} than Pr^{3+} thus making the 1NN site more favorable.

We created an oxygen vacancy in undoped ceria in order to calculate the bulk activation energy. Then the migrating oxygen ion was placed midway between two lattice sites (the saddle point). This oxygen ion was then restricted in its motion by removing one of the degrees of freedom of motion and the cell was relaxed. The difference in energy between this saddle point configuration and the unrestricted configuration was then calculated. We calculated this to be 0.47 eV and it is the bulk diffusion energy $E_{(\text{Bulk})}$. This value is in reasonable agreement with other theoretical calculations [1, 5, 8, 19, 42, 135–137]. It also compares well with the experimental value of 0.52 eV obtained by Steele and Floyd [38] and of 0.49 eV obtained by Adler et al. [36]. Our calculations yielded activation energies for vacancy migration along the paths 1NN $\rightarrow$ 1NN, 2NN $\rightarrow$ 2NN, and 3NN $\rightarrow$ 3NN to be

0.73 eV, 0.47 eV, and 0.47 eV, respectively. The reason that migration along the 1NN $\rightarrow$ 1NN is more difficult is because of the presence of the large Ce^{3+} ion near this migration path. As can be seen in Fig. 4.4 the 2NN $\rightarrow$ 2NN, and 3NN $\rightarrow$ 3NN these paths are far enough removed from the dopant atom so that their environment can be considered to be similar to that of the undoped ceria.Thus, the migration energies along these paths are also similar to that of the bulk.

We found that the most favorable migration path is the $E_{(2,1)}$ path with an energy barrier of 0.428 eV, while that of the $E_{(1,2)}$ is slightly larger at 0.437 eV. But, given the small difference (of only 0.009 eV) between $E_{(2,1)} = 0.428$ eV and $E_{(1,2)} = 0.437$ eV for neodymium doped ceria we can expect to find oxygen vacancies being facilitated by both the 1NN and 2NN sites. This suggests that NDC has higher ionic conductivity than undoped ceria, so it can be more easily reduced. Migration along the 1NN $\rightarrow$ 3NN and 3NN $\rightarrow$ 1NN has an activation barrier of 2.77 eV and 2.66 eV. This means that these jump events will be extremely rare and are unimportant pathways for vacancy diffusion. Table 4.3 compares the results of the Nd-doped ceria with those of Pr-doped and Gd-doped ones carried out by Dholabhai et al. [7,8]. So far our group has calculated the oxygen migration energies by the DFT+U method in ceria doped with four of the elements of the Lanthanide series (Fig. 4.5).

4.6 Conclusion

In this chapter we have discussed the DFT+U calculations for neodymium doped ceria to investigate oxygen vacancy migration. We have verified the known bulk properties of pure ceria and have calculated the energy barriers along different migration pathways. We have found that the first nearest site to Nd^{3+} is the most favorable for vacancy formation and that the 2NN $\rightarrow$ 1NN to be the most favorable. Our calculations validate experimental results that the inclusion of dopants in pure ceria reduces the activation barrier to vacancy migration—thus diffusion and ionic conductivity is increased. We can expect that adding more dopants would further lower the activation barrier. In order to explore the variation of diffusion (and hence the ionic conductivity) as a function of dopant concentration, and also

Element	La Lanthanum	Ce Cerium	Pr Praseodymium	Nd Neodymium	Pm Promethium	Sm Samarium	Eu Europium	Gd Gadolinium	Tb Terbium
Atomic No.	**57**	**58**	**59**	**60**	**61**	**62**	**63**	**64**	**65**
Atomic Wt.	138.9055(2)	140.116(1)	140.90765(2)	144.24(3)	[145]	150.36(3)	151.964(1)	157.25(3)	158.92534(2)
Atomic radius (pm)	187.7	182.5	182.8	182.1	181.0	180.2	204.2	180.2	178.2
Ionic radius (pm)	103.2	101.0	99.0	98.3	97.0	95.8	94.7	93.8	92.3
Atomic electron configuration	$[Xe]5d^16s^2$	$[Xe]4f^15d^16s^2$	$[Xe]4f^36s^2$	$[Xe]4f^46s^2$	$[Xe]4f^56s^2$	$[Xe]4f^66s^2$	$[Xe]4f^76s^2$	$[Xe]4f^75d^16s^2$	$[Xe]4f^96s^2$
Ln^{3+} electron configuration	[Xe]	$[Xe]4f^1$	$[Xe]4f^2$	$[Xe]4f^3$	$[Xe]4f^4$	$[Xe]4f^5$	$[Xe]4f^6$	$[Xe]4f^7$	$[Xe]4f^8$

Figure 4.5: The periodic table of the Lanthanide series. The atomic and ionic radiii information are from Cotton [138].

Table 4.3: Activation energies (E_a) oxygen migration in Pr-doped, Gd-doped, Sm-doped and Nd-doped ceria. E_{Bulk} is the activation energy for bulk diffusion in ceria and $E_{(m,n)}$ is the activation energy of an oxygen atom to migrate from a site mNN to a site nNN in the doped ceria. NN $\equiv$ nearest neighbor. All energies are in eV.

Migration pathway	$E_{Pr-doped}$[a]	$E_{Gd-doped}$[b]	$E_{Sm-doped}$[c]	$E_{Nd-doped}$[d]
$E_{(Bulk)}$	0.47	0.47	0.47	0.47
$E_{(1,1)}$	0.78	0.59	0.66	0.73
$E_{(1,2)}$	0.41	0.50	0.47	0.44
$E_{(1,3)}$	2.79	2.61	2.69	2.77
$E_{(2,1)}$	0.43	0.36	0.40	0.43
$E_{(2,2)}$	0.47	0.48	0.48	0.47
$E_{(2,3)}$	0.57	0.49	0.51	0.55
$E_{(3,1)}$	2.69	2.46	2.56	2.66
$E_{(3,2)}$	0.44	0.46	0.45	0.45
$E_{(3,3)}$	0.47	0.47	0.47	0.47

[a] Reference [7]
[b] Reference [8]
[c] Dholabhai (unpublished)
[d] This work

of the temperature, we have used the values reported in this chapter as inputs to the Kinetic Lattice Monte Carlo (KLMC) code that we discuss in the next chapter.

Chapter 5

KINETIC LATTICE MONTE CARLO

Since KLMC methods have proven very useful in the investigation of oxygen diffusion in other oxides, as discussed in Chapter 1, it makes sense to apply this methodology to doped ceria. Previous KLMC models have often suffered from two limitations: 1) very limited data on dopant effects on vacancy migration, often limited to a single binding energy, and 2) a failure to include the effect of repulsion between the oxygen vacancies. In this chapter we discuss the development of a KLMC model that overcomes both of these limitations, and use it to investigate the effects of dopant concentration and temperature on ionic conductivity in the following chapters. This model can be used as a design tool to determine the optimal concentration of dopants for maximizing ionic conductivity.

We have developed[1] a Kinetic Lattice Monte Carlo (KLMC) code to simulate the oxygen vacancy in a doped ceria structure, doped with atoms from the lanthanide series, and have applied it to Gd (gadolinium), Pr (praseodymium), and Nd (neodymium). In the KLMC method we start out by placing the basis atoms and dopants at lattice sites appropriate for the ceria, and then move the atoms from site to site. All atoms are allowed to move subject to a jump frequency and some activation energy that is temperature dependent. The jump events are randomly picked subject to some probability condition [45, 139].

5.1 Computational Methodology

Monte Carlo (MC) techniques were developed originally by Von Neumann, Ulam and Metropolis [140] and broadly refer to diverse approaches to unraveling problems involving the use of random numbers to sample the ensemble. Kinetic Lattice Monte Carlo (KLMC) is one such approach used to model lattice dynamics with the evolution of time. In the KLMC model, all atoms are assumed to occupy lattice sites that coincides with the local potential minimum with a potential barrier, E_{xy}, separating the adjacent lattice sites. The

[1] This code is written in Fortran 90 and was co-developed by Shahriar Anwar and Pratik Dholabhai.

only meaningful events in KLMC simulations are those involving transfer or exchange of atoms from one lattice site to another. In this dissertation we focused on a vacancy diffusion mechanism in order to save computational memory and effort by only tracking the oxygen vacancies, and by assuming all other sites are occupied. In events where $E_{xy} \gg k_B T$, the transition rate of a vacancy moving from lattice site x to y is evaluated by the hopping mechanism governed by the Arrhenius Law:

$$q_{xy} = \nu_{xy} e^{(-E_{xy}/k_B T)} \tag{5.1}$$

Here ν_{xy} represents the attempt frequency for an atom hopping from lattice site x to y. The harmonic approximation of the effective attempt frequency corresponding to the defect vibrations can be expressed using the dynamical matrix theory [141] as:

$$\nu_{xy} = \frac{\prod_{i}^{3N} \nu_i^{min}}{\prod_{i}^{3N-1} \nu_i^{sad}} \tag{5.2}$$

where, ν_i^{min} and ν_i^{sad} represent normal mode frequencies at the minimum and saddle point position of the hopping atom respectively and N is the numbers of ions. The KLMC model requires input rates for various allowable events, such as diffusion and reactions. One key aspect of the KLMC algorithm are these input rates, since if these rates are known then one can accurately simulate time-dependent diffusion of various species. The pros and cons of various approaches for identifying the rate process database in a KLMC simulation are explained by Adams et al. [45]. KLMC simulations based on a set of kinetic atomic-scale processes can describe the evolution of mesoscopic systems up to macroscopic times. In this way, we have developed a 3-D KLMC model of vacancy diffusion in ceria and doped ceria. This model will further enable us to calculate ionic conductivity of various doped materials with respect to the dopant concentration.

The KLMC technique is based on a blend of Monte Carlo approaches and Poisson processes. In the current KLMC model, the material in consideration can consist of various possible events and evolve as a series of independent events occurring in accordance with

the input rates. Assuming Arrhenius dependence, the diffusivity can be expressed as:

$$D = D_o exp\left(\frac{-\Delta E_a}{k_B T}\right) \tag{5.3}$$

where D_o is the pre-exponential factor, T is the absolute temperature and k_B is the Boltzmann constant. The term E_a generally comprises of two contributions: the total migration energy ΔE_m, and the vacancy formation energy ΔE_v. Primarily, most of the vacancies in ceria-related materials are generated to maintain the charge balance due to the addition of aliovalent dopants. For example, the addition of Pr^{+3} to CeO_2 results in an oxygen vacancy for every two ionized dopants (this is the stoichiometric vacancy to dopant ratio of 0.5). Moreover, the vacancy formation energy in ceria and doped ceria is very high; hence the concentration of vacancies created thermally in the electrolyte is extremely small. Consequently, the vacancy formation energy term (ΔE_v) can be neglected and effectively the energy term in Eq. 5.3 consists only of vacancy migration energy ΔE_m. Dholabhai et al. [7] have argued that the activation energy for vacancy migration is actually a complex average of many jump events. Therefore, activation energies of various diffusion pathways for oxygen vacancy migration in doped ceria can be calculated for a vacancy hopping mechanism [7]. These energies are input to the KLMC model.

The average rate of displacement of defects in solids by thermal activation can be calculated using classical rate theory [142]. Accordingly, the hopping rate for the defect can be expressed by Eq. 5.1. The pre-exponential factor (D_o) in Eq. 5.3 mainly consists of the jump distance (for ceria it is half the length of the lattice parameter) and the hopping rate for the migrating vacancy. In the current work, the jump distances for all first neighbor jumps were assumed to be constant for various dopant concentrations as very small changes in O$-$O bond length (~ 0.001 nm) are expected. The attempt frequency (5×10^{12} Hz) was determined from Eq. 5.2. It is the ratio of the product of $3N$ normal frequencies of the entire system at the starting point of the transition to the $3N-1$ frequencies of the system constrained in the saddle point configuration. This value of attempt frequency was assumed constant for different configurations, as the normal mode frequencies are not expected to differ significantly.

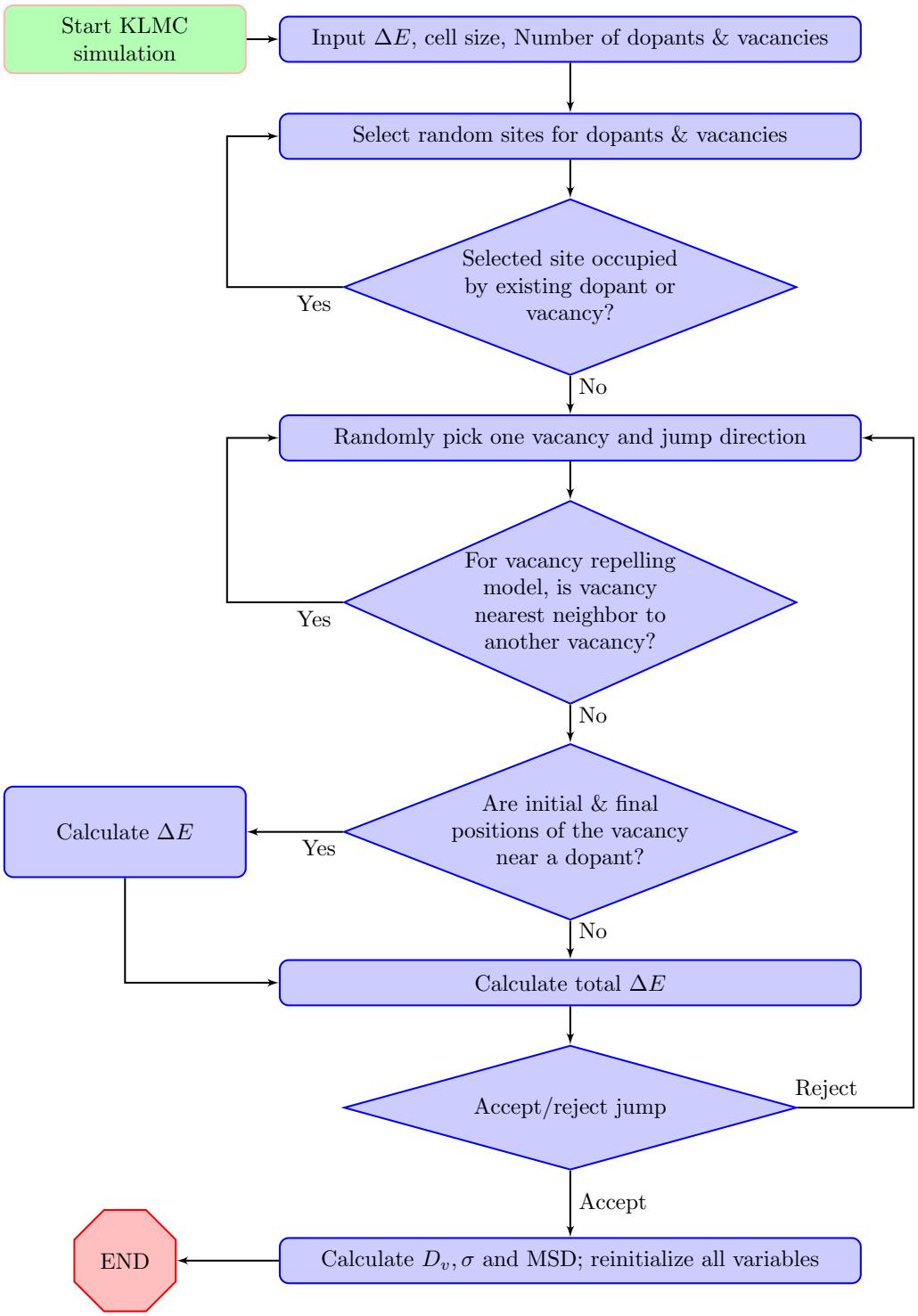

Figure 5.1: Flowchart of the major events involved in a KLMC simulation. NN and MSD represents the next neighbor and mean square displacement, respectively; D_v is the diffusion coefficient and σ is the conductivity.

The KLMC model comprises a number of ordered events which take place in a sequence as given in the flowchart in Fig. 5.1. We computed the mean square displacement of all the vacancies in the simulation cell (accounting for crossing periodic boundaries) and used the results to calculate the diffusion coefficient of oxygen vacancies as follows:

$$D_v = \lim_{t\to\infty} \sum_{i=1}^{N} \frac{|R_i(t) - R_i(0)|^2}{6t} \tag{5.4}$$

where t is the sum of all the time steps Δt, for each jump event and $R_i(t)$ is the position of the i-th vacancy at time t. Following the computation of oxygen vacancy diffusion coefficient, the ionic conductivity was calculated using the Nernst-Einstein relation [14]:

$$\sigma_i = \frac{D_v C_i (qe)^2}{k_B T} \tag{5.5}$$

where σ_i is the ionic conductivity, C_i is the concentration of ionic carriers (vacancies for the present case) and qe their charge.

5.2 The KLMC Code

The KLMC code works by creating a lattice, say $2 \times 2 \times 2$, and by defining the number of vacancies and the number of dopants. Initially we simulate pure ceria by setting the number of dopants to zero, and setting the number of vacancies to 8.

We then specify the basis atom positions. These are the positions where the dopant atoms go. Since we are using the fluorite structure, the possible dopant positions are at 1/4 and 3/4 positions. The dopants are placed randomly, while ascertaining that no dopant site contains more than one dopant. For the pure ceria structure we ignore the random placement of the dopants and fill all the sites with Ce (cerium) atoms.

The specific steps of the code are:

1. Define a lattice (by using CrystalMaker, for example).
2. Specify the number of dopants, and vacancies.
3. Enter the activation energies calculated using DFT+U in the VASP software.
4. Randomly place the dopants in acceptable sites.
5. Randomly place the vacancies in their permitted sites.

6. Randomly select a vacancy.
7. Randomly select a jump direction for the vacancy (from a list of possible jump directions)
8. Accept this jump in one time step (subject to some acceptance criteria).
9. Record the new position of this vacancy, either moved or not.
10. Move on to the next vacancy and repeat for all the vacancies.
11. Repeat the cycle for a total simulation time of $TotalTime$ seconds. The number of times, k, the entire simulation is run is given by $k = TotalTime/\tau$ where τ is a time step that is entered by the user and is selected subject to the criterion that it is a reasonable fraction of the typical or average jump time.
12. Calculate the mean x, y, and z positions, both at the start and at the end of the simulation.
13. Calculate the diffusivity from $D_x = ((\Delta x)^2 \times TotalTime)/4$ (similarly for D_y and D_z).
14. Repeat the simulation at different temperatures and times.

Note that the jump acceptance criteria is a function of the average jump time; average jump time being just the reciprocal of the jump frequency;

$$JumpFrequency = AttemptFrequency \times exp(-\Delta E/(k_B \times Temperature)) \tag{5.6}$$

where ΔE is the activation energy barrier in the jump direction, k_B is the Boltzmann constant, and $Temperature$ is in Kelvins.

Diffusion is happening all the time, dependent on the diffusion coefficient, the temperature, and time. *Net* diffusion in any direction takes place in the presence of some driving mechanism. such as the concentration gradient or a potential gradient. So D_x exists and can be calculated, *even* in the absence of any net diffusion. To calculate D_x we need only keep count of the number of successful jumps in the x-direction. We set $AttemptFrequency = 10^{13}$ [99]. The activation energies ΔE are obtained from density functional theory (DFT) calculations using VASP. They are dependent on the initial and final positions. We use periodic boundary conditions for the cells to keep our cells at a reasonable size while simulating the bulk behavior. We also take into account the constraints

that the dopants and vacancies when they are placed one by one, after some random event, are not placed on an already occupied site. We also take into consideration the possibility that vacancies may repel each other and therefore, in one version of the code we forbid placement of them at adjacent sites.

In the next chapters we present the results of simulations carried out for neodymium, praseodymium, and gadolinium doped ceria for varying dopant concentrations and at different temperatures. We plan to put this KLMC code on the web in the future and perhaps also develop an interactive graphical front end to it.

Chapter 6

PRASEODYMIUM DOPED CERIA

In this chapter we discuss the implementation of the Kinetic Lattice Monte Carlo (KLMC) code that we discussed in the previous chapter to study the oxygen vacancy migration in praseodymium doped ceria (PDC). We use a database of activation energies for oxygen vacancy migration, calculated using first-principles, for various migration pathways in PDC[1].

6.1 Calculation Details

Activation energies of various diffusion pathways for oxygen vacancy migration in praseodymium-doped ceria (PDC) has been calculated using DFT+U by Dholabhai, et al. [7]. The energies from this work, as presented in Table 6.1, are input to the KLMC model. It should be noted that, for PDC, the oxygen prefers a second nearest neighbor (2NN) site, which means that many types of jump events need to be included (1NN $\rightarrow$ 2NN, 2NN $\rightarrow$ 2NN, 2NN $\rightarrow$ 3NN, etc.) to properly model the complexity.

We used a $10 \times 10 \times 10$ cell comprising of 12,000 possible sites to place the respective ion. The periodic cell with a $10 \times 10 \times 10$ periodicity was built from a conventional 12-atom cubic unit cell of ceria using the theoretically optimized lattice constant of 5.494 Å for bulk ceria as reported in Chapter 4. Of these 12,000 positions, 4,000 are available for dopant placement and 8,000 sites for vacancy formation. The vacancies are allowed to hop to adjacent sites, subject to certain constraints. The simulation cell was repeated periodically along the three axes to simulate a lattice of effectively infinite extent. The dopant and vacancy concentration were varied. All the dopant ions are assumed to be trivalent, hence for every two dopant ions, a vacancy was incorporated. For each of the different dopant concentrations, ten simulations were performed, each with a different dopant distribution. Each simulation comprised of approximately 3000,000 or more jump events. This resulted in achieving a statistical average with a precision of $\sim 3\%$ for various dopant con-

[1]The contents of this chapter has been published [7] in the Journal of Solid State Chemistry where I am a coauthor and Pratik Dholabhai is the first author.

centrations. Considering the difference of the order of $\sim 3\%$ in ionic conductivity for the simulations involved, the sampling does not require additional runs for each configuration. The simulations were performed for temperatures ranging from 673 K to 1073 K and approximately equal diffusion distances were used to calculate the final diffusion coefficients. To plot the Arrhenius relationship and facilitate comparison with the available experimental data, some specific configurations were simulated for temperatures ranging from 573 K to 1173 K.

Table 6.1: Activation energies for oxygen vacancy migration along distinctive pathways in PDC calculated using first-principles. $E(X,Y)$ denotes activation energy for a oxygen atom migrating from X-nearest neighbor (XNN) to Y-nearest neighbor (YNN) with respect to the Pr ion in PDC.

Migration pathway	Activation energy (eV)
$E(1,1)$	0.78
$E(1,2)$	0.41
$E(1,3)$	2.79
$E(2,1)$	0.43
$E(2,2)$	0.47
$E(2,3)$	0.57
$E(3,1)$	2.69
$E(3,2)$	0.44
$E(3,3)$	0.47

We have developed two separate models for PDC, a Vacancy Non-Repelling model (VNR) and a Vacancy Repelling model (VR). Calculations using the DFT+U methodology were carried out by Dholabhai et al. [7] to investigate vacancy diffusion in PDC. In that work the calculations were performed for charge neutral supercells. They studied two separate cases for PDC; (i) Vacancies are placed next to the dopant ions (ii) Vacancies are placed far apart from the dopant ions. For case (i), they found that the configuration involving two vacancies separated by a distance larger than the 1NN (nearest-neighbor) distance is more stable by 0.38 eV as compared to the configuration with vacancies placed next to each other. For case (ii), the configuration involving two separated vacancies is more stable by 0.28 eV as compared to the configuration with vacancies placed next to each other. The

observed Coulomb interaction between charged vacancies lead us to develop two separate models; (1) In the VNR model, vacancies are allowed to move anywhere in the simulation cell except into an existing vacancy; (2) In the VR model, the vacancies are not allowed to move adjacent (first nearest neighbor) to any other vacancies in the simulation cell, nor into an existing vacancy. (It would be slightly more accurate to add the repulsion energy. But the repulsion energy is so large (~ 0.35 eV) that it is very rare that vacancies will move adjacent to one another, so this is a very good approximation)[2]. Previous studies have neglected the Coulomb interaction between the anionic species, but we find that this effect is important in correctly characterizing the optimal dopant concentration in ceria related electrolyte materials.

6.2 Effect of Multiple Dopants

The energies given in Table 6.1 correspond to vacancy motion adjacent to one trivalent Pr ion as shown in Fig. 6.1. In the presence of multiple dopant ions, we use an underlying assumption that every additional Pr dopant in the vicinity of the migrating vacancy will have an additive effect towards the activation energy for vacancy migration. For example, for paths 1NN $\rightarrow$ 2NN and 2NN $\rightarrow$ 1NN, we found that the decrease in activation energy for ceria doped with two Pr ions located next to each other was twice as much compared to ceria doped with two Pr ions that are separated. Using first principles calculations Dholabhai et al. [7] found that in the vicinity of two next neighbor Pr dopant ions, the decrease in activation energy relative to the undoped ceria for the migration path 1NN $\rightarrow$ 2NN is 0.13 eV as compared to 0.06 eV in presence of one Pr dopant ion. Similarly, for the migration path 2NN $\rightarrow$ 1NN, the respective numbers are 0.07 eV and 0.04 eV. In the KLMC model, for the migration paths 1NN $\rightarrow$ 2NN and 2NN $\rightarrow$ 1NN in presence of two Pr dopant ions, the decrease in activation energy is calculated to be 0.12 eV and 0.08 eV, respectively. These numbers justify the assumption (additive effect of dopants) incorporated in the KLMC model and provide a reasonable approximation of migration energies

[2]The vacancy repulsive energy was calculated by creating two structures, one structure with two vacancies next to each other and another one with two vacancies farthest from each other, and then calculating the difference in the total energies of each system.

in the presence of multiple dopants. Moreover, this decrease in activation energy for the case where two Pr ions are next to each other is in reasonably good agreement with results reported by Andersson et al. [1]. Using this relationship in the KLMC model, we have simulated diffusion of oxygen vacancies in the presence of multiple dopants. Under the current assumption, the estimated activation energies for multiple dopants are probably valid to about 10 meV at low to moderate concentrations, but may be larger at higher concentrations.

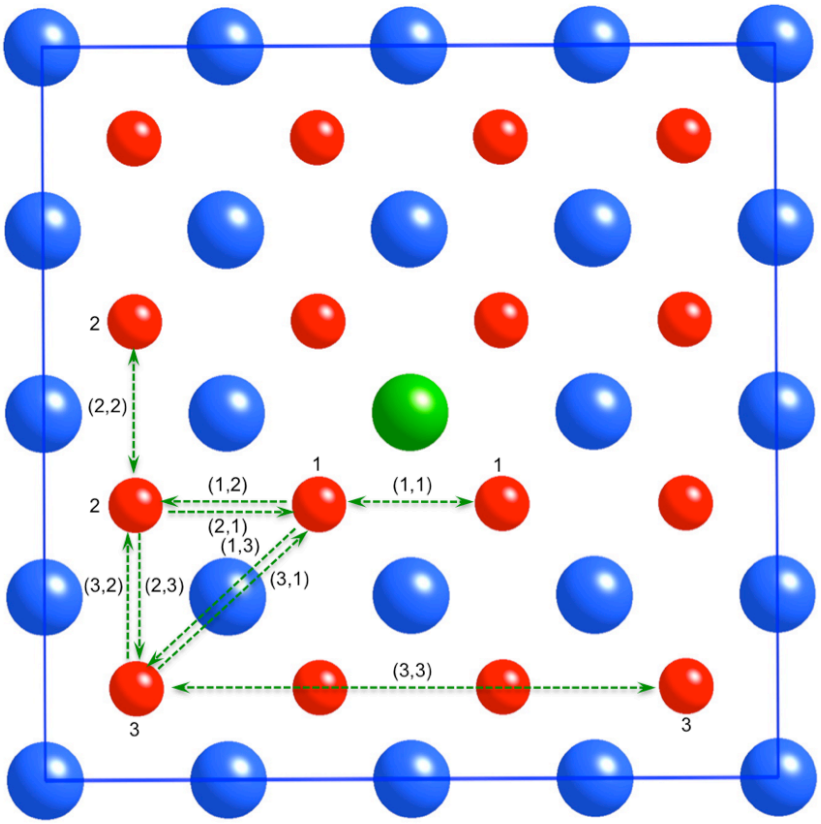

Figure 6.1: Top view of a $2 \times 2 \times 2$ PDC supercell. The blue, green and red balls represent Ce, Pr and O ions, respectively. Numbers 1, 2 and 3 represent 1NN, 2NN and 3NN oxygen ions with respect to the Pr ion, respectively. (X,Y) represents an oxygen ion jump from XNN to YNN. Pr ion closer to the migrating vacancy is only shown. (*Note*: we have represented the ions following the CPK (Corey, Pauling, and Kultun) scheme conventionally used by chemists in most publications. J. C. Slater (1964) *J. Chem. Phys.* 41:3199.)

6.3 Diffusion Results

One of the principal goals of the current effort is to study the variations in ionic conductivity as a function of dopant concentration in PDC and to determine the optimal dopant concentration that exhibits a maximum in ionic conductivity. As mentioned earlier, researchers have previously studied other systems with similar methodology, but have neglected the Coulomb interactions between the charged vacancies. Hence, we also wish to investigate the significance of including these effects. Fig. 6.2 comprises the simulation results for variations in ionic conductivity as a function of dopant concentration in PDC using the KLMC–VNR model for temperatures ranging from 673 K to 1073 K. For the temperatures ranging from 673 K to 873 K, the maximum in ionic conductivity is observed at $\sim 25\%$ dopant concentration, whereas the maxima at temperatures of 973 K and 1073 K are shifted at $\sim 30\%$ dopant concentration. Incorporating the effects of charged vacancies using the VR model significantly changes the results. Plotted in Fig. 6.3 are the variations in ionic conductivity as a function of dopant concentration in PDC using the KLMC-VR model for temperatures ranging from 673 K to 1073 K. The overall effect of the VR model is to reduce vacancy diffusion, especially at higher concentrations, which also results in a shift of the peak conductivity towards lower concentrations. For the temperatures of 673 K and 773 K, the maximum in ionic conductivity is predicted at $\sim 15\%$ dopant concentration, whereas the maximum at temperature ranging 873 K to 1073 K is predicted at $\sim 20\%$ dopant concentration.

Considering all the simulations performed for PDC using KLMC–VNR and VR models, the magnitude of ionic conductivity is larger for the values obtained using the VNR model. This is a consequence of the fewer number of available sites for the vacancies to migrate on the oxygen sublattice for the VR model due to the vacancy-repelling factor, which decreases the diffusion coefficient. The computed maximum in ionic conductivity at around $\sim 25\%$ to $\sim 30\%$ dopant concentration using the KLMC–VNR model agrees well with experiment [30, 143], but does not provide the true picture. Praseodymium is known to have mixed valence at atmospheric pressure, and hence equilibrium between Pr^{4+} and

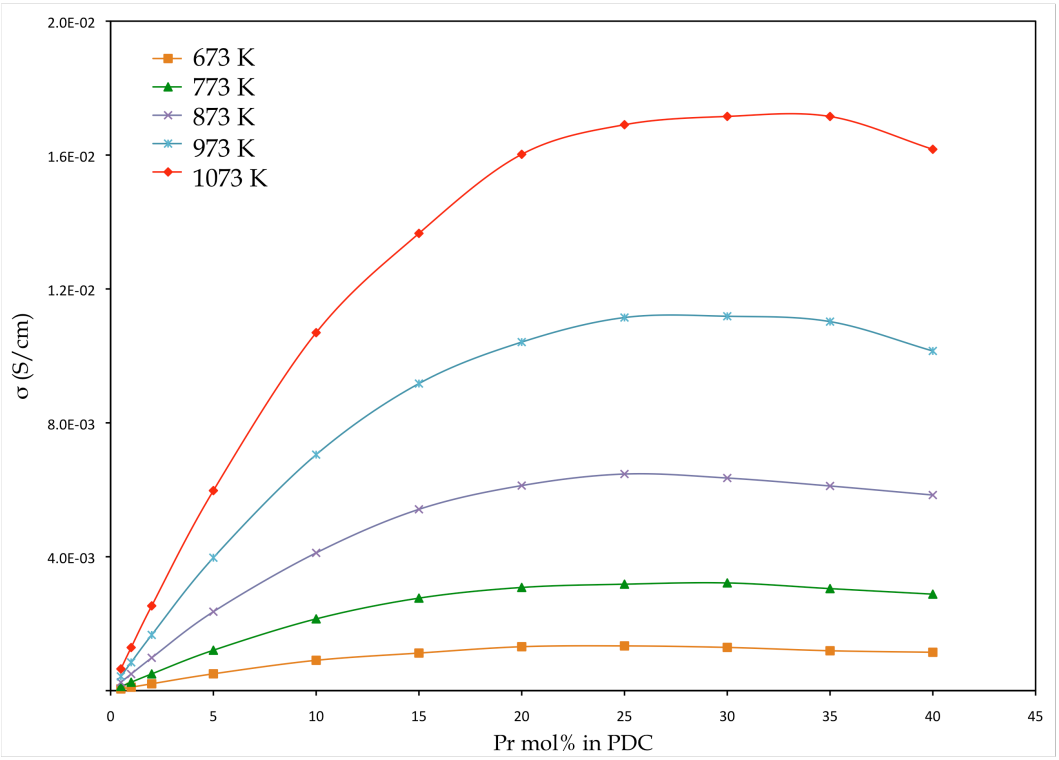

Figure 6.2: Plot of calculated ionic conductivity of PDC as a function of dopant concentration generated using KLMC-VNR model for temperature ranging from 673 K to 1073 K.

Pr^{3+} exists determined by the temperature and oxygen pressure. Hence, only half of the dopant ions are Pr^{3+} [30, 144]. This equilibrium reduces the probable oxygen vacancy concentration upon doping with Pr and hence the ionic conductivity increases more slowly with increase in Pr content as compared to other aliovalent dopants [145]. In the current simulations performed using both VNR and VR models, all the Pr dopant ions are assumed to be trivalent. Hence, the results obtained with the KLMC models should be compared with experimental data plotted vs. ionized dopants, not total dopants. In some cases it has been estimated that only half of the dopants are ionized, so this is a large effect.

Experimental studies by Shuk and Greenblatt [30] and Chen et al. [146] found that the maximum in ionic conductivity occurred at about $\sim$ 30% dopant concentration. If we assume that approximately half of these dopants are trivalent (in the experiment, only half of the dopants are ionized) [30, 143], the optimal concentration of dopants ($\sim$ 15% to $\sim$ 20%)

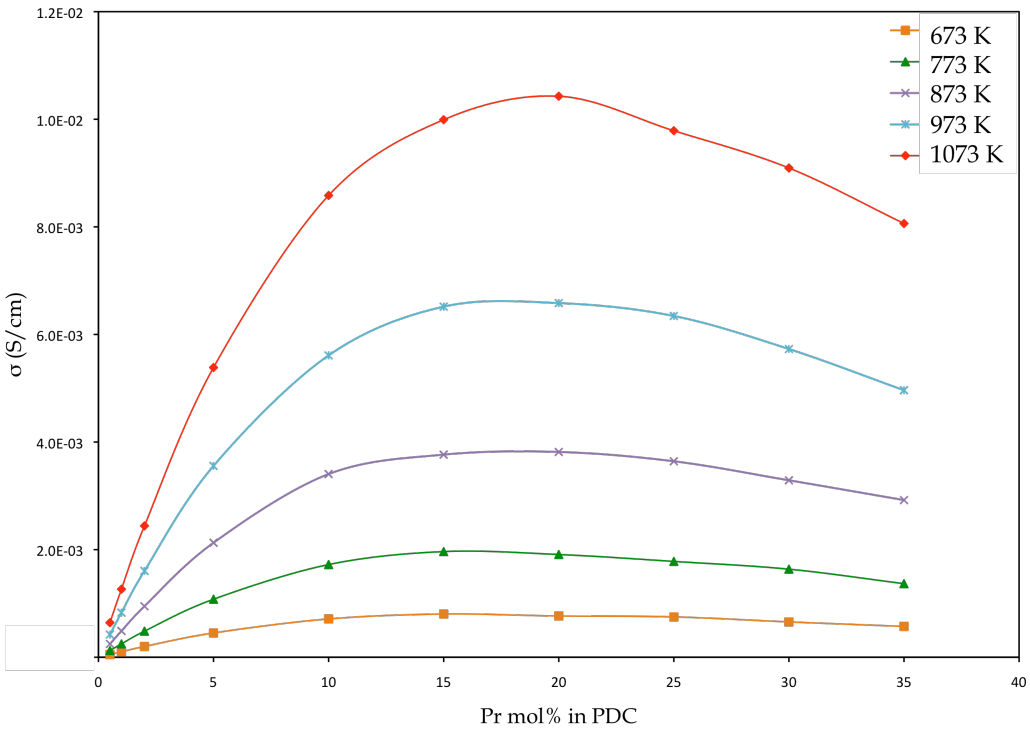

Figure 6.3: Plot of calculated ionic conductivity of PDC as a function of dopant concentration generated using KLMC-VR model for temperature ranging from 673 K to 1073 K.

as predicted by the KLMC–VR model is in reasonably good agreement with the measured values. Moreover, the slight discrepancy in the experimental and theoretical findings can be attributed to the dependence of oxygen vacancy concentration on the temperature and oxygen partial pressure, and also to grain boundary effects, effects that are not included in the KLMC model.

In order to further investigate the origin behind the calculated maximum in the ionic conductivity, we performed additional simulations using the KLMC-VR model at 873 K. Fig. 6.4 shows two different scenarios, (i) the vacancy concentration is increased linearly keeping the dopant concentration fixed at $\sim 20\%$, (ii) increasing the dopant concentration linearly and keeping the vacancy concentration fixed at $\sim 5\%$. For case (i), the ionic conductivity keeps increasing, as shown in the figure. The slight dip in the curve is due to vacancy-vacancy interactions at higher vacancy concentration, but this effect is modest.

Case (ii) results in a steadily decreasing ionic conductivity. The conductivity decreases in case (ii) because a growing fraction of the vacancies get trapped near the dopant ions, decreasing the net diffusion. This effect is significantly larger than the effect of vacancy-vacancy interactions (case (i)), which also decreases ionic conductivity.

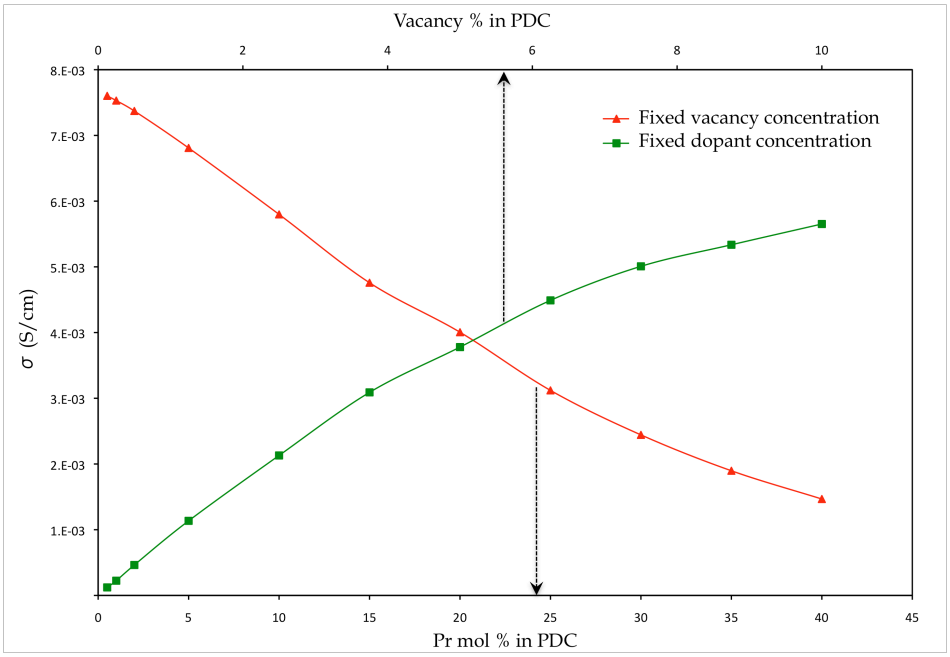

Figure 6.4: Plot of calculated ionic conductivity as a function of fixed dopant concentration and fixed vacancy concentration using the KLMC-VR model at 873 K. For the plot with fixed dopant concentration, the *x*-axis represents the varying vacancy concentration.

Overall, these two investigations explain the increase and then decrease in ionic conductivity with increasing dopant concentration. Initially, the ionic conductivity increases at lower dopant concentration due to the increase in vacancy concentration, but after reaching a maximum, it decreases due to increasing interactions between the dopant ions and vacancies that serves as a bottleneck, decreasing the number of minimum energy pathways for a vacancy to diffuse.

Nauer et al. [29] reported that the total conductivity of PDC increases until a dopant concentration of $\sim 40\%$ to $\sim 50\%$ is reached. This is due to the fact that for PDC, beyond $\sim 25\%$ to $\sim 30\%$ dopant concentration, the electronic conductivity exceeds the ionic con-

ductivity [30] and hence explains the higher dopant concentration for attaining a maximum in electrical conductivity. Fig. 6.5 shows the plot of ionic conductivity versus dopant concentration at 973 K using the KLMC–VNR and VR model. Fig. 6.6 shows data obtained by experimental measurements performed by Shuk and Greenblatt [30] and Chen et al. [146]. The primary reason for the discrepancy in the absolute magnitude of the conductivity as observed from the experimental measurements, as shown in Fig. 6.6, is probably due to the difference in synthesis methods of the respective samples [30, 143]. Depending on the fraction of dopants that are trivalent, the graph obtained using the KLMC–VR simulations should be shifted somewhat towards the right. This is in reasonable agreement with experimental data if the vacancy concentration is half (in the experiment, only half of the dopants are ionized) of what should be expected after the addition of Pr dopant [30, 143]. Overall, Fig. 6.5 shows that the trend of increased conductivity in PDC can be reasonably predicted using KLMC–VR model if the fraction of ionized dopants is known.

The primary reason for the decrease in the ionic conductivity with increasing dopant concentration is the increase in average activation energy for vacancy migration and the percent increase of Pr ions near the migrating vacancy. The increasing number of Pr ions often tends to bind the neighboring oxygen vacancy more strongly and decrease the diffusion coefficient, which in turn decreases the oxide ion conductivity. At low dopant concentration, the number of available minimum energy diffusion pathways is higher. For PDC, the formation of an oxygen vacancy is found to be most favorable at the 2NN position [7] to the Pr dopant and hence the available minimum energy pathways keep decreasing with increasing of dopant ion concentration leading to this behavior. Thus the simulations results, obtained using the KLMC–VR model, show reasonable agreement with the experimental data and highlight the importance of including the Coulomb interactions between the anionic species. Hence, the current methodology serves as a fundamental tool for predicting the optimal dopant concentration in PDC.

Fig. 6.7 and Fig. 6.8 show values of ionic conductivity as a function of inverse temperature for $Ce_{0.90}Pr_{0.10}O_{2-x}$ and $Ce_{0.80}Pr_{0.20}O_{2-x}$ respectively, obtained from KLMC

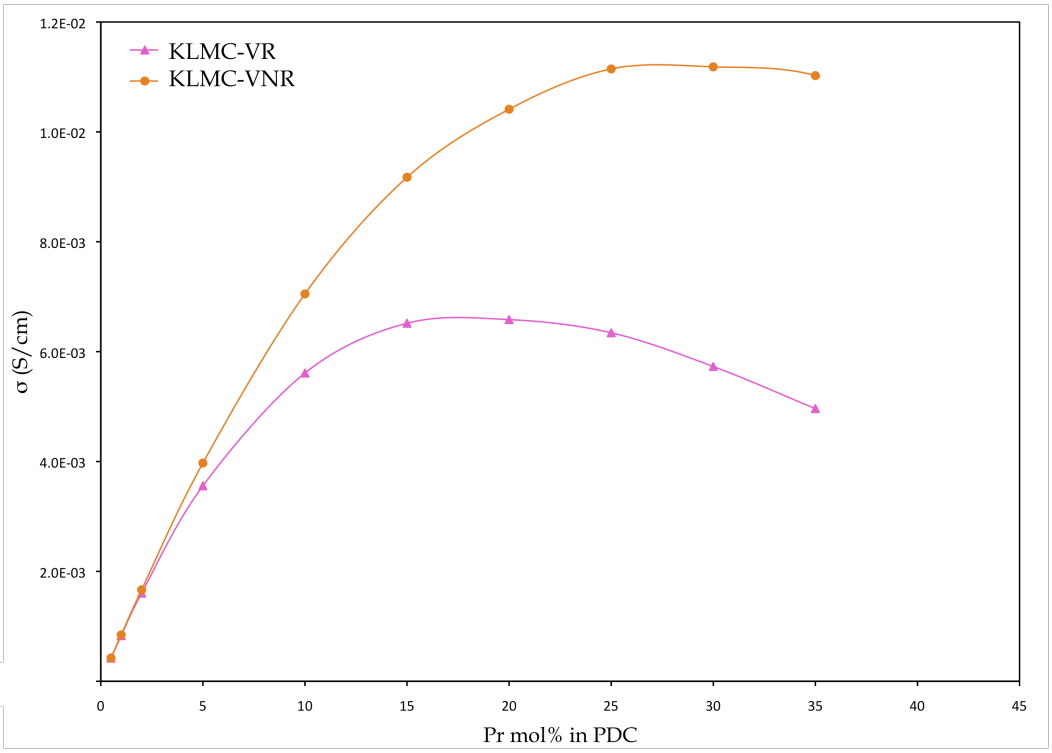

Figure 6.5: Ionic conductivity data calculated for PDC obtained using KLMC-VNR and VR models for simulations performed at 973 K. In both KLMC models, we assume that all the dopants are ionized.

simulations and experimentally measured values [29, 30]. The Arrhenius type behavior of the ionic conductivity for this particular configuration is visible with all the simulation data points for KLMC-VNR and VR models lying on straight lines. The simulation results agree reasonably well with the experiments with some discrepancy in the magnitude of ionic conductivity, but this could be due to the reasons mentioned above. For Fig. 6.8, our theoretical results are in the middle of two sets of experimental measurements, and the trends with temperature are very similar. Nauer [29] is the total conductivity, whereas our model and Shuk [30] included only the ionic contribution to the conductivity. Several other plots for different compositions have been studied and the general trends and conclusions that can be drawn are analogous.

A vacancy can move through a number of distinctive diffusion pathways before finally diffusing across an ionic conductor such as PDC. Determination of the rate-limiting

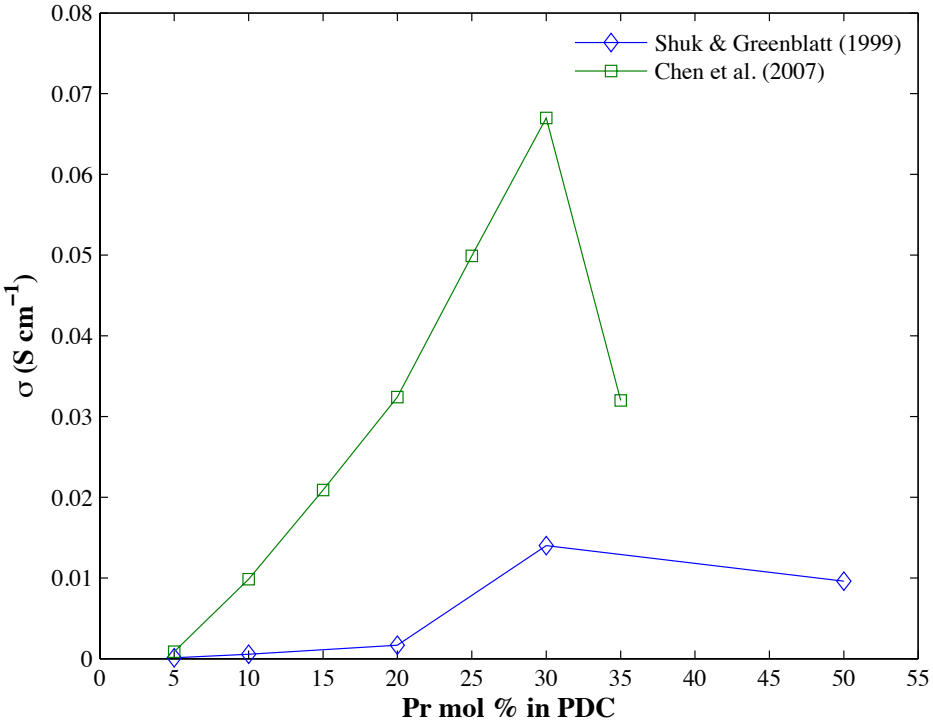

Figure 6.6: Ionic conductivity data for PDC obtained by experimental measurements performed at 973 K. □: Ref. [30] and ⋄: Ref. [146]. Only half of the dopants are ionized. The lines are provided only to guide the eye.

step for a path is complex, because it depends on the dopant concentration and arrangement. The input rates used for the KLMC simulations were evaluated using the DFT+U calculations [7] and provide a very reasonable initial assumption, but the migration energy for a complete diffusion path cannot be associated with a single migration event. It has to be averaged using a statistical model that takes into account the distinct pathways involved during diffusion. Moreover, the migration energies generated using first-principles are applicable for processes occurring at 0 K. Hence we have compared the statistically averaged migration energies elucidating the temperature dependence with the experimentally measured values. Fig. 6.9 shows averaged activation energy for vacancy migration as a function of dopant concentrations. The activation energies presented in Fig. 6.9 are computed from the slopes of similar Arrhenius plots as seen in Fig. 6.7 and Fig. 6.8.

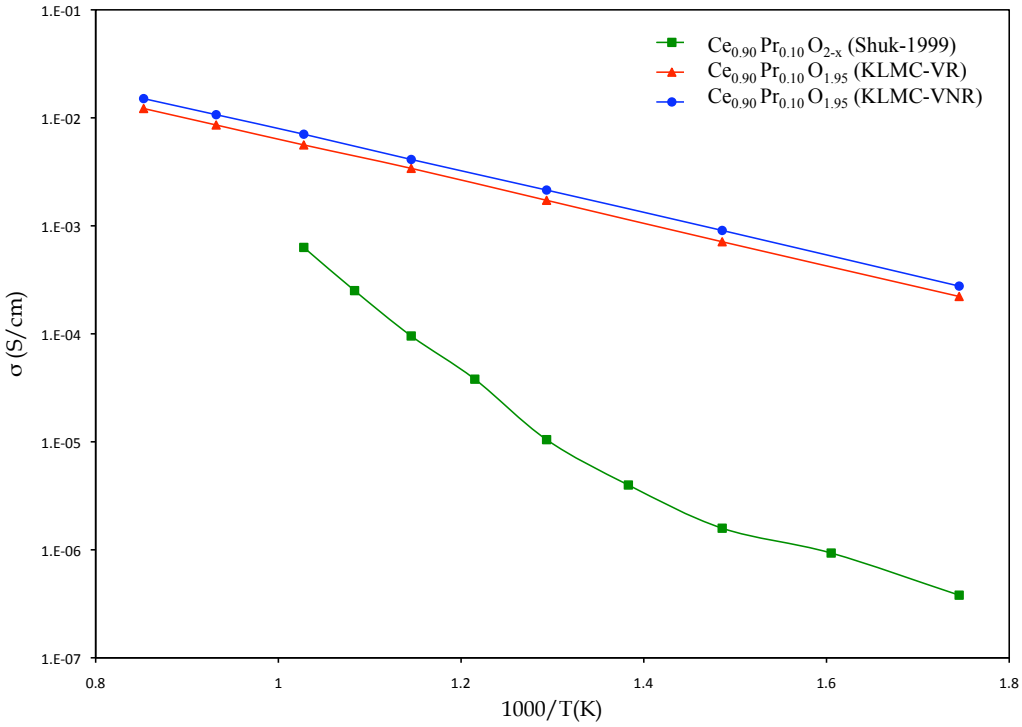

Figure 6.7: Arrhenius plot of ionic conductivity of 10 mol% PDC as a function of temperature ranging from 573 K to 1173 K for the KLMC simulations and 573 K to 973 K for experimental data (Shuk & Greenblatt [30]).

The plots of average activation energy as a function of dopant concentration generated using KLMC–VNR and KLMC–VR simulations show similar behavior with the former having slightly lower magnitude. The experimental values taken from the measurements performed by Shuk et al. [30] are compared with those obtained from simulations in Fig. 6.8. The experimental and theoretical values are in good agreement at low dopant concentrations, and both increase with increasing dopant concentration, but the effect is larger for the experimental data, although there are significant error bars. The small increase in the activation energy for vacancy migration at dopant concentrations ranging from $\sim 5\%$ to $\sim 15\%$ as seen in Fig. 6.8 from simulations is primarily due to negligible interactions between oxygen vacancies and dopant ions. At higher dopant concentrations, the increase in average activation energy for migration is due to the increased likelihood of finding two next neighbors Pr−Pr or Pr−Ce ions pairs near an oxygen vacancy, where a higher energy

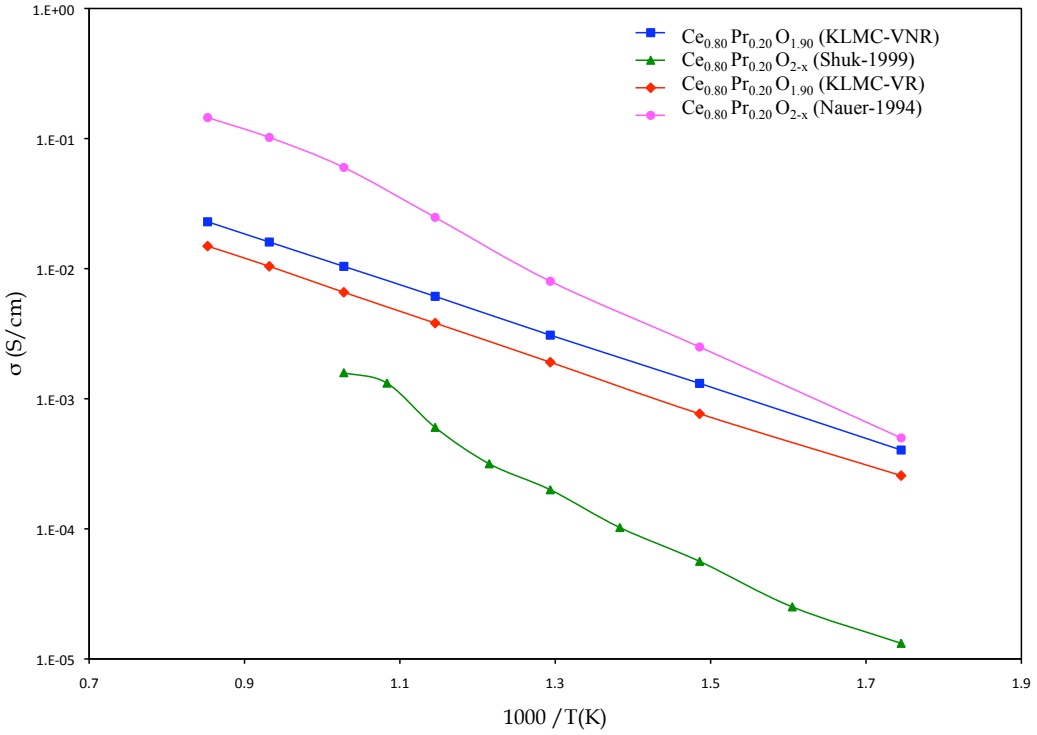

Figure 6.8: Arrhenius plot of ionic conductivity of 20 mol% PDC as a function of temperature ranging from 573 K to 1173 K for the KLMC simulations and 573 K to 973 K for experimental data (Shuk & Greenblatt [30]) and Nauer et al. [29]).

is needed to overcome these barriers. Any further increase in the Pr ions can eventually trap the vacancy and form a bottleneck for diffusion. This is also evident from the earlier explanation and Fig. 6.4, where the increase in dopant concentration is found to be primarily responsible for the decrease in ionic conductivity after attaining a maximum. The differences between theory and experiment may partly be due to 1) limitations in the DFT data used as input, 2) assumptions involved in the KLMC model regarding activation energies, 3) the large uncertainty of the order of 50 meV in measured values, 4) the experimental samples are polycrystalline, so grain boundaries may have a small effect, and 5) variations in sintering temperature may affect the level of reduction of the experimental samples. Nauer et al. [29] reported an experimentally measured value of activation energy ranging between 0.42–0.53 eV for $\sim$ 20% dopant concentration for PDC as compared to the average activation energy value 0.39 eV obtained for similar dopant concentration by KLMC simulations.

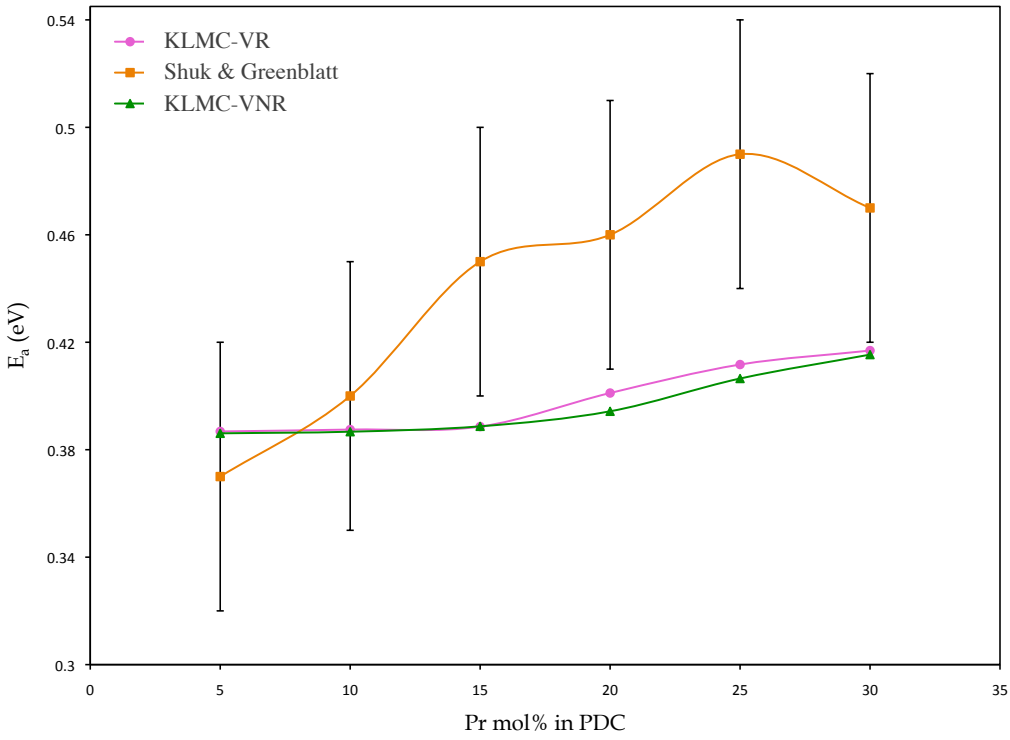

Figure 6.9: Average activation energy as a function of dopant concentration for PDC compared with the available experimental data. The experimental data involves error bars of 50 meV.

Keeping this in mind, the averaged activation energies obtained from KLMC simulations are in reasonable agreement with the measured values.

6.4 Conclusions

We have used KLMC simulations in conjunction with previously published activation energies calculated using density functional theory method to investigate oxygen vacancy diffusion in PDC. The increase in average activation energy for vacancy migration as a function of dopant concentration is due to the increase in Pr–Pr dopant pairs that hinder further motion of the oxygen vacancies. Our findings follow similar trends as compared with previously measured values. A dopant concentration of approximately $\sim 15\%$ to $\sim 20\%$ is found to be optimal for achieving maximum ionic conductivity in PDC. The KLMC simulations are in reasonably good agreement with the available experimental data, when we

take into account that only about half of the dopants are ionized. The decrease in ionic conductivity with increasing dopant concentration is correlated with the increase in average activation energy for vacancy migration from the vicinity of the dopant pairs and the subsequent decrease in availability of minimum energy pathways for the vacancy diffusion. Based on the reasonable agreement with experimental measurements, we believe that the current model can be used as a design tool to predict the optimal dopant concentration for attaining maximum ionic conductivity.

Chapter 7

GADOLINIUM DOPED CERIA

7.1 Introduction

Gadolinium doped ceria (GDC) is one of the ceria-based materials that has been studied extensively over the years by measurement and calculation of oxide ion conductivity as a function of temperature and dopant concentration. In this chapter we discuss the implementation of the Kinetic Lattice Monte Carlo (KLMC) code to study the oxygen vacancy migration in GDC.

Among reported results for ceria doped with different aliovalent dopants, GDC is considered to be one of the most promising solid electrolyte materials for operation of SOFC below 600 °C [3, 4]. Activation energies for gadolinium doped ceria have been calculated by Dholabhai et al. [7] using first-principles (DFT+U) methodology to study defect migration in doped ceria. The results of those first-principle calculations are ideally suited for input into kinetic lattice Monte Carlo (KLMC) models of vacancy diffusion. In the previous chapter on praseodymium doped ceria we have employed a systematic approach of inputting the activation energies calculated by first-principles to the KLMC model to study time-dependent vacancy diffusion in doped ceria [147]. There we have presented the results and methodologies of several studies with similar approach employing Monte Carlo simulations in conjunction with first-principles calculations.

Determination of the optimal dopant concentration that exhibits maximum conductivity is critical for the use of doped ceria as an electrolyte material in SOFC. For GDC, there are often inconsistent and sometimes contradictory experimental reports on the best composition that exhibits maxima in conductivity, including 10%, 15% , and 20% Gd (i.e., $Ce_{0.90}Gd_{0.10}O_{2\text{-}x}$ [4, 148], $Ce_{0.85}Gd_{0.15}O_{2\text{-}x}$ [149–152] and $Ce_{0.80}Gd_{0.20}O_{2\text{-}x}$ [153–157]). A few reports suggest that the best compositions for GDC were temperature dependent with the dopant concentration shifting towards a higher value with increasing temperature. For example, shifts from 15% to 21% dopant concentration with a temperature increase from

773 K to 1073 K [152]], from 20% to 24% dopant concentration with a temperature increase from 973 K to 1073 K [157], and from 15% dopant concentration below 673 K to 20% above 673 K [155] were reported. Steele [4] reported that a GDC sample with 10% dopant concentration exhibited the maximum conductivity, but after summarizing other authors work indicated that at 773 K, the total conductivity peaks at around 25% dopant concentration. The scatter in the measured data for best compositions of GDC showing peak conductivity can be attributed mainly to the divergences in sample preparation, variations in sintering temperature, and variations in the level of reduction in the samples. Moreover, the level of the purity of the ceramic sample also affects the conductivity as impure samples exhibit considerable grain boundary resistivity. SiO_2, one of the predominant impurities at the grain boundary in ceria related materials, reportedly affects the conductivity [56] and is introduced in the sample through the precursor chemicals and sample preparation [4, 158, 159].

Reported computational studies for predicting the compositional dependence of the oxygen vacancy diffusion constant in GDC are limited to molecular dynamics simulations. Hayashi et al. [55] used ab-initio ACDvb vmolecular dynamics simulations to investigate oxygen diffusion and the microscopic structure of ceria-based solid electrolytes with different dopant radii. Inaba et al. [56] studied oxygen diffusion in Gd-doped ceria using classical molecular dynamics simulations. They reported that the diffusion constant shows maxima at the gadolinia content of 10 mol% and decreases at higher gadolinia contents. They attributed the formation of Gd−vacancy−Gd clusters and long-range interactions between the oxygen vacancies to be the possible mechanisms for decrease in diffusion constant at higher gadolinia content. These molecular dynamics simulations were carried out at 1273 K, higher than the effective temperature ranges for the operation of SOFC. Hence, knowledge of various compositions of GDC showing peak conductivities at lower temperatures will be very insightful towards selecting the appropriate electrolyte materials for SOFC. Moreover, an issue with the molecular dynamics simulations is that they are performed over a very short time frame that can lead to insufficient statistical sampling of various configurations.

7.2 Computational Methodology

The activation energies of various diffusion pathways for oxygen vacancy migration in GDC for a vacancy hopping mechanism have been calculated by Dholabhai et al. [7] and is presented in Table 7.1. These energies are inputted to our KLMC model, where every event occurs independently in accordance with the statistically averaged activation energy corresponding to the local environment. For GDC, the oxygen prefers a first nearest neighbor (1NN) site [7], which means that many types of jump events need to be included (1NN $\rightarrow$ 2NN, 2NN $\rightarrow$ 1NN, 2NN $\rightarrow$ 2NN, 2NN $\rightarrow$ 3NN, etc.) to properly model the complexity.

Table 7.1: Activation energies (E_a) for oxygen vacancy migration along various diffusion pathways in GDC calculated using DFT+U. The nearest neighbor positions are given with respect to the Gd ion. Data from Ref. [7].

Migration pathway	Activation energy, E_a (eV)
1NN $\rightarrow$ 1NN	0.59
1NN $\rightarrow$ 2NN	0.50
1NN $\rightarrow$ 3NN	2.61
2NN $\rightarrow$ 1NN	0.36
2NN $\rightarrow$ 2NN	0.48
2NN $\rightarrow$ 3NN	0.49
3NN $\rightarrow$ 1NN	2.46
3NN $\rightarrow$ 2NN	0.46
3NN $\rightarrow$ 3NN	0.47

For GDC, we used a $10 \times 10 \times 10$ cell (consisting of 12,000 sites) built from a conventional 12-atom cubic unit cell of ceria using the theoretically optimized lattice constant of 0.5494 nm for bulk ceria [7, 8]. Among these 12,000 positions, 4,000 are available for Gd dopant placement, which are assumed to be immobile. The vacancies are formed on the oxygen sublattice consisting of 8,000 sites, and are allowed to hop to adjacent sites, subject to certain constraints. The simulation cell was repeated periodically along the three axes to simulate a lattice of effectively infinite extent. The dopant and vacancy concentration were varied in order to maintain a stoichiometric vacancy to dopant ratio of 0.5, as all the dopant ions are assumed to be trivalent. For each of the different dopant concentrations, ten

simulations were performed, each with a different dopant distribution, with approximately 300,000 or more jump events for each configuration. This resulted in achieving a statistical average with a precision of $\sim 3\%$ for various dopant concentrations. Considering the difference of the order of $\sim 3\%$ in ionic conductivity for the simulations involved, the sampling did not require additional runs for each configuration. The simulations were performed for temperatures ranging from 673 K to 1073 K and approximately equal diffusion distances were used to calculate the final diffusion coefficients.

We have developed two separate models, a Vacancy Non-Repelling model (VNR) and a Vacancy Repelling model (VR) [147]. In the VNR model, vacancies are allowed to move anywhere in the simulation cell except into an existing vacancy site. In the VR model, the vacancies are not allowed to move adjacent (1NN) to any other vacancies in the simulation cell, nor into an existing vacancy site (It would be slightly more accurate to add the repulsion energy, but the repulsion energy is so large (~ 5 eV) that it is very rare that vacancies will move adjacent to one another, so this is a very good approximation). These models were developed in order to incorporate the effect of vacancy repelling in ceria related materials. This effect was verified using DFT+U methodology, where we found that the configuration involving two vacancies separated by a distance larger than the 1NN (nearest-neighbor) distance is energetically more stable as compared to the configuration with vacancies placed next to each other [147]. This was also found to be true for GDC. For instance, we studied two separate cases for GDC; (i) Vacancies are placed next to the dopant ions (ii) Vacancies are placed far apart from the dopant ions. For both the cases, (i) and (ii), the configuration involving two vacancies separated by a distance larger than the 1NN (nearest-neighbor) distance is more stable by 0.32 eV and 0.15 eV respectively, as compared to the configuration with vacancies placed next to each other. In this paper we only report results for KLMC-VR, which assumes that vacancies cannot move next to one-another, which is a reasonable approximation for GDC. We also wish to mention that previous studies [36, 40, 47–50] have not included the Coulomb interaction between the anionic species, but we have highlighted the importance of including this effect for correctly characterizing the optimal dopant concentration in ceria related electrolyte materials [147].

Previously, Inaba and co-workers [55, 56] have reported, using molecular dynamics simulations, that the atomic arrangement with the randomly distributed Gd−Gd pairs in GDC is more stable than the arrangement where isolated Gd atoms are distributed randomly. They reached this conclusion based on the closer agreement between experimental measurements and calculated values of lattice parameters and the calculation of the enthalpy of formation. To understand this behavior, we have performed calculations using the DFT+U methodology [7, 8] to investigate the effect of Gd−Gd dopant pairs in GDC. All the calculations were performed for charge neutral supercells. Similar to the reported results [55, 56], we found that the atomic arrangement with Gd−Gd dopant pairs is more stable by 0.17 eV as compared to the arrangement with Gd atoms placed in isolation. In order to incorporate these results from first-principles in the KLMC model and to investigate the effect of Gd−Gd dopant pairs in maximizing the conductivity in GDC, we have developed a separate model called Vacancy-repelling Dopant Pairs (VRDP) model. In the KLMC-VRDP model, the dopants are randomly distributed in Gd−Gd pairs, with the rest of the algorithm being same as the KLMC-VR model. In reality, only a fraction of the Gd ions will exist as pairs, depending on the processing conditions and thermal history of the sample. The KLMC–VRDP model is an approximation of the extreme case where all the dopant ions are assumed to exist in pairs, and serves as an upper-bound on the effect of pairing.

7.3 Results

Vacancy Mobility

In the presence of multiple dopant ions, a common physical scenario encountered in electrolyte materials and the current KLMC model, we use an underlying assumption that every additional Gd dopant ion in the vicinity of the migrating vacancy will have an additive effect towards the activation energy for vacancy migration. Earlier, we have tested this relationship using the first-principles calculations [7, 8] and, justified and explained its use in the working of the KLMC model [147]. Andersson et al. also reported a similar decrease in activation energy for the case where two Gd ions are next to each other [1]. Incorporat-

ing this assumption in the KLMC model, we have simulated diffusion of oxygen vacancies in the presence of multiple dopants. Under the current assumption, the estimated activation energies for multiple dopants are probably valid to about 10 meV at low to moderate concentrations, but may be larger at higher concentrations.

Ionic Conductivity Calculation Using KLMC-VR Model

The primary goal of the current effort is to study various compositions of GDC within the temperature range 673 K to 1073 K and identify the compositions exhibiting peak conductivities at different temperatures. As cited earlier, researchers have previously studied other systems with similar methodology, but have failed to include the Coulomb interactions between the charged vacancies. Moreover, no literature data is available of the Monte Carlo study of various compositions of GDC. Including the effect of vacancy repelling, the simulations results in Fig. 7.1 correspond to the variations in ionic conductivity as a function of dopant concentration in GDC using the KLMC-VR model for temperatures ranging from 673 K to 1073 K. For the temperatures ranging from 673 K to 873 K, the conductivity steadily increases as a function of dopant concentration and exhibits a broad maximum at $\sim 20\%$ dopant content. At higher temperatures, 973 K and 1073 K, the conductivity increases steadily as a function of dopant concentration as observed for the temperature range 673 K to 873 K, but the maximum in conductivity is shifted to higher dopant content with a well-defined peak observed at $\sim 25\%$ dopant content.

Ionic Conductivity Calculation Using KLMC-VRDP Model

Simulation results presented in Fig. 7.2 are generated using the KLMC-VRDP model at temperatures 673 K, 873 K and, 1073 K and compared with the results obtained using the KLMC-VR model. As mentioned earlier, the $\mathrm{Gd}-\mathrm{Gd}$ dopant pairs are randomly distributed in the cationic sites for the VRDP model. For all the temperatures studied, the conductivity increases as a function of dopant concentration and exhibits maxima at $\sim 20\%$ dopant content, but the conductivity for temperatures 873 K and 1073 K shows a broad maximum whereas that for 673 K exhibits a finer peak. Considering all the simulations performed for

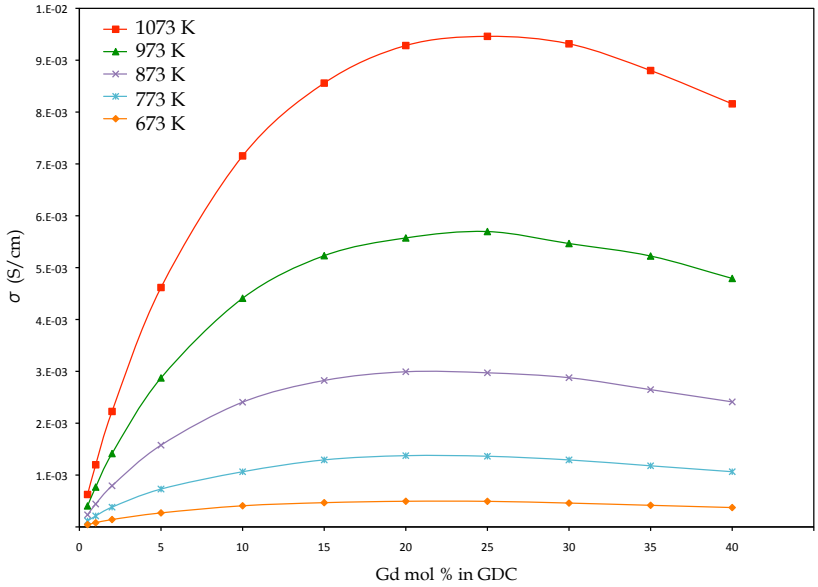

Figure 7.1: Calculated ionic conductivity in GDC as a function of dopant content generated using KLMC–VR model for temperature ranging from 673 K–1073 K.

GDC using KLMC-VR and VRDP models, the magnitude of ionic conductivity is larger for the values obtained using the VR model. This is a consequence of the formation of Gd−vacancy−Gd clusters in the VRDP model, which effectively traps the vacancy and decreases the net diffusion. The Gd−vacancy−Gd cluster can be thought of as a same vacancy having two 1NN Gd dopant ions. The difference in magnitude of conductivity calculated using the VR and VRDP models is smaller at lower dopant concentrations and steadily increases until it reaches a dopant concentration of $\sim$ 30%, after which the difference remains roughly constant. This could be due to the fact that above $\sim$ 30% dopant concentration, even in the VR model, a fraction of dopant ions that are placed randomly might form pairs and have an effect similar to the VRDP model.

For results pertaining to both the models, VR and VRDP, the decrease in ionic conductivity after reaching a maximum can be attributed to (a) growing interactions betweens the vacancies and dopants, and as the number of vacancies increases as a function of increasing dopant concentration, (b) fewer number of available sites for the vacancies to migrate on the oxygen sublattice due to the vacancy-repelling factor. To further substanti-

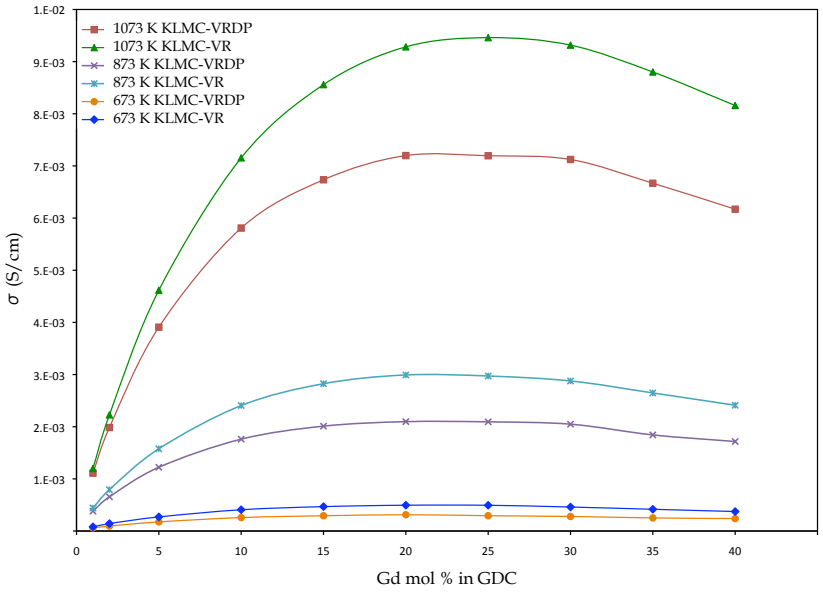

Figure 7.2: Calculated ionic conductivity in GDC as a function of dopant content generated using KLMC–VRDP model for temperatures 673 K, 873 K and 1073 K. Data generated using KLMC-VR model for the same temperatures are also shown for comparison.

ate the origin behind the decrease in conductivity after reaching a maximum, we performed additional simulations using the VR model. We studied two different cases; (i) linearly increasing the vacancy concentration while keeping the dopant concentration fixed, and (ii) increasing the dopant concentration linearly and keeping the vacancy concentration fixed.

For case (i), the ionic conductivity keeps increasing, with a slight dip due to vacancy-vacancy interactions at higher vacancy concentration, but this effect is modest. Simulations for case (ii) results in a steadily decreasing ionic conductivity due to a growing fraction of the vacancies getting trapped near the dopant ions, decreasing the diffusion coefficient. This effect is considerably larger than the effect of vacancy-vacancy interactions as seen in case (i), which also decreases ionic conductivity. Overall, the additive results of these two effects explain the increase and then decrease in ionic conductivity with increasing dopant concentration. A similar behavior was also found to be true for Pr-doped ceria and was reported in our previous effort [147].

Comparison of the Predicted Optimal GDC Composition with Experimental Data

Experimental reports for the best GDC compositions that exhibit maximum conductivity lie on a wide spectrum with varied dopant content. As mentioned in the introduction, best compositions for GDC with a Gd dopant content of 10% [4, 148], 15% [149–152] and 20% [153–157, 160] have been reported. Moreover, the compositions were found to be temperature dependent [152, 155, 157]. Reasons for the scatter in the measured data for best GDC compositions are explained earlier. Fig. 7.3 shows the various trends of increase in ionic conductivity as a function Gd dopant concentration at 973 K for experimentally measured data available from literature. Also included in Fig. 7.3 is a plot of ionic conductivity data generated using the KLMC-VR model at 973K. At 973 K, the GDC composition with $\sim 25\%$ dopant concentration showing peak conductivity using KLMC-VR model is in reasonable agreement with experimental measurements [152–157] reporting samples with $\sim 20\%$ Gd as the best compositions. A few other results predict an optimal dopant concentration of $\sim 15\%$ [149–152]. Two other measurements [4, 148] predict $\sim 10\%$ optimal dopant concentration, but the measurements were not performed for intermediate concentration (i.e 15%, 25%), so there is a possibility of the true maximum being masked. Overall, majority of the experimental work predicts an optimal dopant concentration ranging from 15% to 20% in GDC between the temperature ranges 673 K to 973 K, with some reports claiming the optimal content to be above 20% for higher temperatures [152, 157]. For instance, at 873 K, a few of the experimental measurements [153, 155, 157] reported an optimal dopant concentration of $\sim 20\%$, which is exactly the same concentration as predicted by the current KLMC-VR model.

The above results show that at higher temperatures, the KLMC-VR model predicts a slightly higher optimal dopant concentration for GDC as compared with experiment, but is in reasonable agreement at lower temperatures. The discrepancy between the experimental and theoretical findings may be attributed to the dependence of oxygen vacancy concentration on the temperature and oxygen partial pressure. Moreover, the experimental

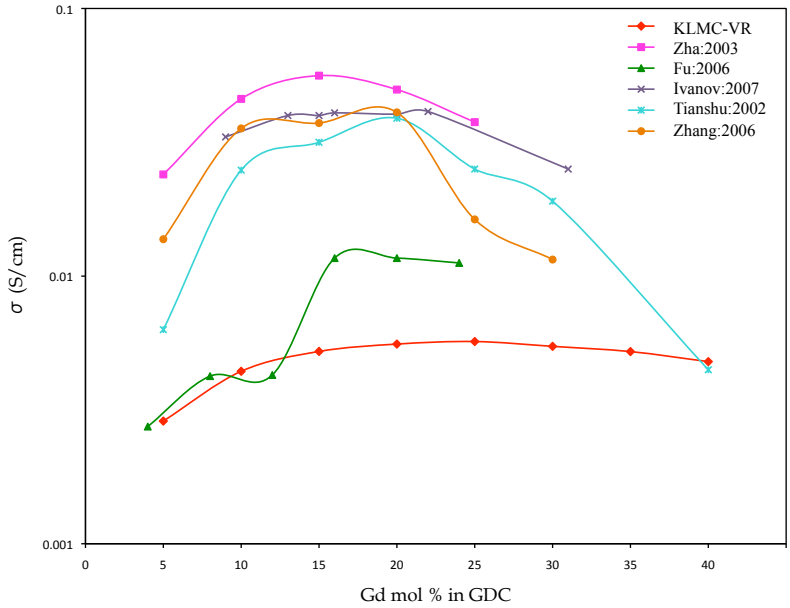

Figure 7.3: Calculated (using KLMC–VR model) and measured ionic conductivity in GDC as a function of dopant content at 973 K.

samples are polycrystalline, and exhibit significant grain boundary resistance with increasing dopant concentration, which decrease the conductivity at lower dopant concentrations as compared to the current KLMC model that does not incorporate grain boundary effects. Slight discrepancy between the results is also expected due to the approximation involved in estimating the migration energies in presence of multiple dopants. Nevertheless, the agreement between the calculated and measured values is especially good considering that all the input data for the KLMC model was generated exclusively using first-principles calculations (no experimental parameters involved).

At 973 K the KLMC-VRDP model predicts an optimal dopant concentration of $\sim 20\%$ (data not shown in the plot), which is in very good agreement with most of the experimental measurements [152–157, 160]. But a direct comparison of the data generated using the KLMC-VRDP model and experimental measurements is not appropriate as no experimental data are available that claim that all the dopants are present in the form of Gd−Gd pairs in GDC. It was reported using MD simulations [55] carried out at 1273

K that the oxygen diffusion coefficient of GDC show maxima at about 20% dopant content. These calculations involved the initial placement of Gd−Gd dopant pairs in GDC similar to the KLMC-VRDP model. The result is similar to the one obtained with the current KLMC-VRDP model that predicts an optimal dopant concentration of $\sim 20\%$, but at a lower simulation temperature of 1073 K. The current simulations for GDC using KLMC-VRDP model were limited to temperatures at and below 1073 K due to its applications as an electrolyte material in SOFC. At 1273 K, we expect a slight shift to higher dopant concentration as compared to the reported optimal concentration of 20% [55]. At this point, further experimental information on the arrangement of dopants with respect to their placement in GDC, whether in isolation, pairs or the approximate fraction of dopants that form pairs, at specific concentrations and temperatures is welcome. In future, the KLMC model can be modified to incorporate these experimental findings to enable an improved and more suitable comparison.

Fig. 7.4 shows values of ionic conductivity as a function of inverse temperature for low Gd concentration ($Ce_{0.05}Gd_{0.20}O_{2-x}$) and one of the most widely used composition of GDC ($Ce_{0.80}Gd_{0.20}O_{2-x}$) obtained from KLMC-VR model and experimentally measured values [149, 151, 152, 155, 157, 160]. The Arrhenius type behavior of the ionic conductivity for this particular configuration is visible with all the simulation data points for KLMC-VR model lying on a straight line. At low dopant concentration, the simulation results at lower temperatures agree reasonably well with the experiments. As can be seen in Fig. 7.4, the simulated data points lie in the center of the various experimental measurements. At higher temperatures the scatter between experiment and simulations increases.

Effect of Dopant Concentration on Lattice Parameter

One effect not included in the KLMC–VR model is the effect of dopants on lattice parameter. Several experiments have demonstrated that the addition of Gd dopants to ceria significantly increases the lattice parameter; for example, at 20% Gd content, the lattice parameter increases by ~ 0.015 Å [149–152, 155, 157]. This small expansion is enough to significantly change activation energies. To investigate this effect, we recalculated acti-

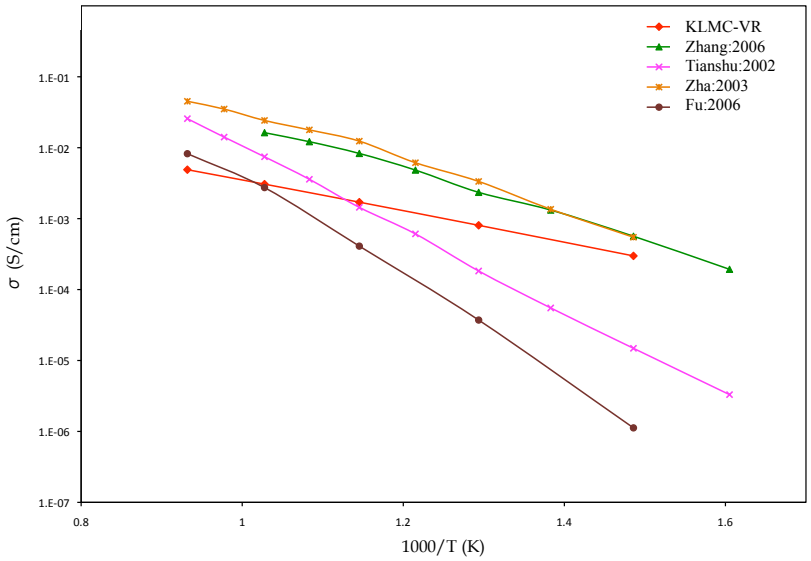

Figure 7.4: Arrhenius plot of ionic conductivity of $Ce_{0.95}Gd_{0.05}O_{2-x}$ as a function of temperature calculated using the KLMC–VR model and compared with the available experimental data. For Fu:2006 [157], the data is plotted for $Ce_{0.96}Gd_{0.04}O_{2-x}$.

vation energies for diffusion of oxygen vacancies in GDC using the experimental percent increase in lattice parameter for 20% dopant concentration to build an expanded 96-atom GDC supercell. The activation energies decreased slightly, as shown in Table 7.2. A small decrease in activation energy has an exponential effect on diffusion and conductivity. The revised activation energies for an expanded cell were input into the KLMC model (now referred to as KLMC-VR,X), and the results are shown in Fig. 7.5.

For 20 mol% GDC, the KLMC–VR,X model yields conductivities that are approximately an order of magnitude higher than for the KLMC–VR model. The observed increase in conductivity is due to the slightly larger space available for the oxygen ion diffusion that decreases the activation energy for vacancy migration. The agreement of the two models with experiment is similar, with the KLMC–VR model having better agreement at lower temperatures, and the KLMC–VR,X model having better agreement at higher temperatures. However, although the predicted magnitude of ionic conductivity agrees surprisingly well with experimental measurements, the slope of the experimental curves is significantly

Table 7.2: Calculated activation energies (E_a) for oxygen vacancy migration along various diffusion pathways in the expanded GDC supercell built by including the experimental percent increase in lattice parameter as a function of 20% dopant concentration.

Migration pathway	Activation energy, E_a (eV)
1NN $\rightarrow$ 1NN	0.56
1NN $\rightarrow$ 2NN	0.47
1NN $\rightarrow$ 3NN	2.57
2NN $\rightarrow$ 1NN	0.33
2NN $\rightarrow$ 2NN	0.47
2NN $\rightarrow$ 3NN	0.46
3NN $\rightarrow$ 1NN	2.42
3NN $\rightarrow$ 2NN	0.44
3NN $\rightarrow$ 3NN	0.46

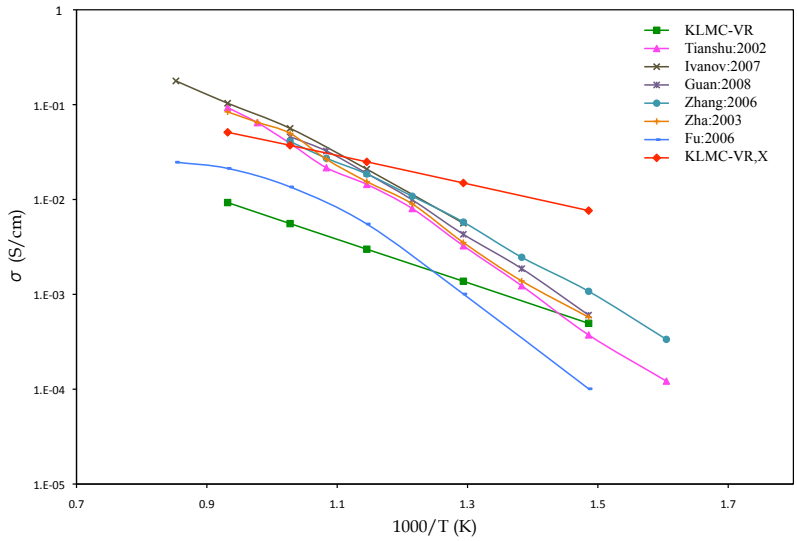

Figure 7.5: Arrhenius plot of ionic conductivity of $Ce_{0.80}Gd_{0.20}O_{2-x}$ as a function of temperature calculated using the KLMC–VR and KLMC–VR,X models and compared with the available experimental data.

higher than the slope of the calculated KLMC curve, and the reasons for that discrepancy are unclear. A few other plots for different compositions (10, 15 and 25 mol% GDC) have been studied as well (not presented here) and the overall trends and conclusions that can be drawn are similar.

Thermal expansion will also have a slight effect on the activation energies, and in fact, the thermal expansion of GDC has been found to increase as a function of dopant content [161, 162]. However, the magnitude of this effect is much smaller than the effect of the dopants, so it is not included here.

The large effect of dopant expansion of the lattice on ionic conductivity suggests that the addition of other dopants that expand the lattice more may be beneficial. This effect may be an important guide in searching for new dopants for ceria.

Average Activation Energy

Dholabhai et al. [7] have argued that the determination of the rate-limiting step for a path is complex, because it depends on the dopant concentration and arrangement. The input rates used for the KLMC simulations were evaluated using the DFT+U calculations [7] and provide a very reasonable initial assumption, but the migration energy for a complete diffusion path cannot be associated with a single migration event. It has to be averaged using a statistical model that takes into account the distinct pathways associated with the particular configuration. The average activation energy for 5% dopant concentration in GDC computed using the results from KLMC-VR model is 0.43 eV. Using DFT+U, we found that for $\sim 6\%$ dopant concentration, activation energy for vacancy migration of a single mobile vacancy along the most favorable path 2NN $\rightarrow$ 1NN is 0.36 eV. This shows that the calculations of a single most favorable migration energy is not sufficient to correctly depict long time diffusion and that a single migration energy does not allow a fitting comparison with the experimentally measured values.

Fig. 7.6 shows averaged activation energy for vacancy migration as a function of increase in dopant concentration computed using the KLMC-VR model and available experimental values [4, 150, 152, 155, 160] to enable comparison with the current simulations. The calculated activation energies presented in Fig. 7.6 are computed from the slopes of similar Arrhenius plots as the one presented in Fig. 7.5. The calculated increase in activation energy with increasing dopant concentration is in good qualitative agreement with the

experimental measurements, but the effect is more pronounced for the experimental data. At higher dopant concentrations, the increase in average activation energy for migration is due to the increased likelihood of finding two next neighbors Gd−Gd pairs near an oxygen vacancy, where a higher energy is needed to overcome these barriers. Any further increase in the Gd ions can eventually trap the vacancy and form a bottleneck for diffusion. This is also evident from the earlier explanation suggesting the increase in dopant concentration to be the primary cause for the decrease in ionic conductivity at very high dopant concentration. The differences between theory and experiment may be partly due to limitations in the DFT data used as input and the assumptions involved in the KLMC model for multiple dopants. In addition, the experimental samples are polycrystalline, so grain boundaries may have a small effect. For example, at 10% dopant concentration, the computed and measured values [150] are in reasonably good agreement, but at higher dopant concentration, the discrepancy increases. Considering the above effects, the averaged activation energies obtained from the KLMC simulations are in reasonable agreement with the measured values.

7.4 Conclusions

We have performed KLMC simulations to predict the optimal dopant composition for GDC that exhibits maximum ionic conductivity. As an input to the KLMC model, we have used the activation energies for vacancy migration along distinct diffusion pathways calculated using DFT+U. Applying the KLMC–VR model for the temperature ranges 673 K to 1073 K, a dopant concentration of $\sim$ 20% to 25% is found to be optimal for achieving maximum ionic conductivity in GDC. The current findings are found to follow similar trends as compared with the previously measured values. The linear increase in ionic conductivity at low dopant concentration and its gradual decrease at higher dopant concentration after reaching a maxima can be explained due to the combined effect of (i) increasing interactions between the dopant ions and vacancies that block further diffusion of vacancies; (ii) fewer sites being available for vacancies to migrate due to the vacancy-repelling effect; and (iii) the increase in average activation energy as a function of the increase in dopant concentration.

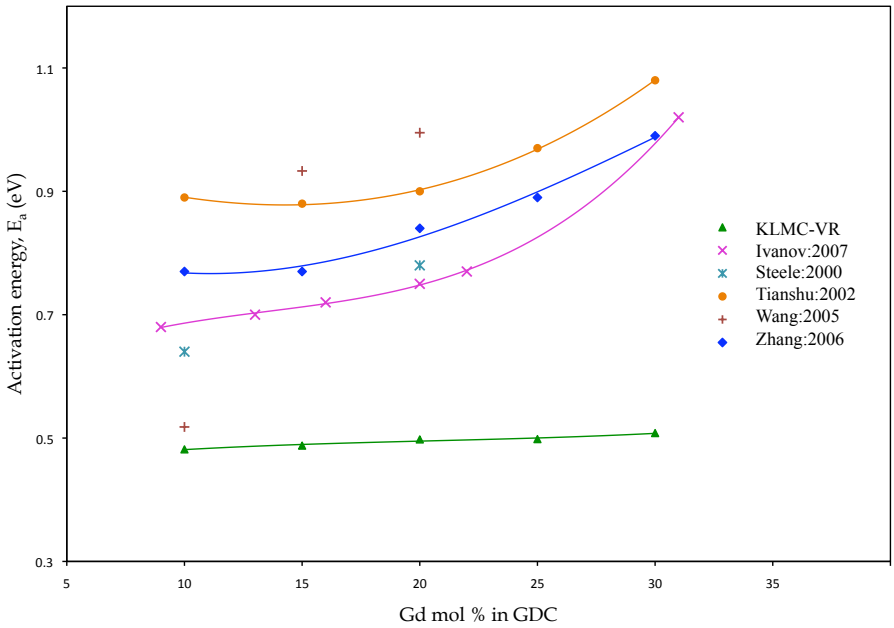

Figure 7.6: Average activation energy as a function of dopant concentration for GDC calculated using the KLMC–VR model and compared with the available experimental data.

We also present an alternative KLMC–VRDP model, which assumes that all the dopants are placed in Gd−Gd pairs. The KLMC–VRDP model results in slightly lower conductivities, and shifts the peak to somewhat lower dopant concentrations.

To include the effect of lattice parameter expansion due to dopant addition, we developed a KLMC–VR,X model, which uses the activation energies calculated in an expanded GDC lattice. For 20 mol% GDC, KLMC–VR,X model yields conductivities that are approximately an order of magnitude higher than for the KLMC-VR model. The agreement of the two models with experiment is similar, with the KLMC–VR model having better agreement at lower temperatures, and the KLMC–VR,X model having better agreement at higher temperatures. Based on the agreement with experimental measurements, the KLMC model in conjunction with first-principles calculations can be used as a design tool to predict the optimal dopant concentration in ceria related materials for electrolyte applications.

Chapter 8

NEODYMIUM DOPED CERIA

In the last two chapters we have discussed the utilization of the Kinetic Lattice Monte Carlo (KLMC) code that we developed to praseodymium and gadolinium doped ceria electrolytes in order to determine the effect of dopant concentrations and temperatures on the ionic conductivity. In this chapter we apply the code to study neodymium doped ceria (NDC) using similar techniques. We use the same technique as in the last two chapters by utilizing a database of activation energies for oxygen vacancy migration, calculated using first-principles, for various migration pathways in neodymium-doped ceria.

8.1 Calculation Details

In Chapter 4 we reported the density functional theory calculations of the activation energies of various diffusion pathways for oxygen vacancy migration in neodymium-doped ceria (NDC). The energies from those calculations, as presented in Table 8.1, are input to the KLMC model. It should be noted that, for NDC, the oxygen prefers a first nearest neighbor (1NN) site, which means that many types of jump events, such as 1NN $\rightarrow$ 2NN, 2NN $\rightarrow$ 1NN, 2NN $\rightarrow$ 3NN, need to be included to properly model the complexity.

Table 8.1: Activation energies for oxygen vacancy migration along distinctive pathways in NDC calculated using first-principles. $E_{(m,n)}$ denotes activation energy for a oxygen atom migrating from m-nearest neighbor (mNN) to n-nearest neighbor (nNN) with respect to the Nd ion in NDC.

Migration pathway	E_a (eV)
$E_{(1,1)}$	0.73
$E_{(1,2)}$	0.44
$E_{(1,3)}$	2.77
$E_{(2,1)}$	0.43
$E_{(2,2)}$	0.47
$E_{(2,3)}$	0.55
$E_{(3,1)}$	2.66
$E_{(3,2)}$	0.45
$E_{(3,3)}$	0.47

For the KLMC simulation for NDC we used a $10 \times 10 \times 10$ supercell consisting of 12,000 possible sites to place the respective ion. The periodic cell with a $10 \times 10 \times 10$ periodicity was built from a conventional 12-atom cubic unit cell of ceria using the theoretically optimized lattice constant of 5.494 Å for bulk ceria as reported in Chapter 4. Of these 12,000 positions, 4,000 are available for dopant placement and 8,000 sites are available for vacancy formation. The vacancies are allowed to hop to adjacent sites, subject to certain constraints. The simulation cell was repeated periodically along the three axes to simulate a lattice of effectively infinite extent. The dopant and vacancy concentration were varied. All the dopant ions are assumed to be trivalent, hence for every two dopant ions, an oxygen vacancy was introduced. For each of the different dopant concentrations, seven to fourteen simulations were performed, each with a different dopant distribution. Each simulation comprised of approximately 3000,000 or more jump events. This resulted in achieving a statistical average with a precision of $\sim 3\%$ for various dopant concentrations. Considering the difference of the order of $\sim 3\%$ in ionic conductivity for the simulations involved, the sampling does not require additional runs for each configuration. The simulations were performed for temperatures ranging from 673 K to 1073 K and approximately equal diffusion distances were used to calculate the final diffusion coefficients. To plot the Arrhenius relationship and for comparison with available experimental data, some specific configurations were simulated for temperatures ranging from 573 K to 1173 K.

We have simulated the NDC calculations using two separate models for NDC, a Vacancy Non-Repelling model (VNR) and a Vacancy Repelling model (VR). We performed preliminary calculations using the DFT+U methodology, discussed in Chapter 4, to investigate vacancy diffusion in NDC. All the calculations were performed for charge neutral supercells. The observed Coulomb interaction between charged vacancies lead us to develop two separate models; (1) In the VNR model, vacancies are allowed to move anywhere in the simulation cell except into an existing vacancy; (2) In the VR model, the vacancies are not allowed to move adjacent (first nearest neighbor) to any other vacancies in the simulation cell, nor into an existing vacancy. (It would be slightly more accurate to add the repulsion energy. But the repulsion energy is so large (~ 5 eV) that it is very rare that vacancies will

move adjacent to one another, so this is a very good approximation). Previous studies have neglected the Coulomb interaction between the anionic species, but we find that this effect is important in correctly characterizing the optimal dopant concentration in ceria related electrolyte materials.

8.2 Calculation of Error Bars

Computer simulations do not produce identical results each time a simulation is run. This is because of round-off errors and the randomness of the random number generator. We observed this in our calculations. For a small number of runs the scatter in the data was quite large resulting in large error bars for our data points. As the number of runs were increased the scatter (error bars) got smaller. In order to determine the number of runs needed to produce an acceptable error (at 95% confidence level) in our calculations we used the equation

$$\text{StandardError}(x) = \frac{abs(t_{n-1})}{\sqrt{n}} \times \text{StandardDeviation}(x) \tag{8.1}$$

where $n-1$ is the degrees of freedom and t is obtained from the t-table for one-tailed distribution at a 95% confidence level. We conducted a number of test runs to determine the standard deviation of our data, and once we had decided upon what standard error to accept, we were able to settle on the number of runs n. we decided that we needed about ten runs for desirable extent of our error bars.

We ran the KLMC simulation for each dopant concentration at each temperature for fifteen times. However, due to server bottlenecks we did not get the results of all these runs. We obtained results for seven to fourteen runs for the VNR model.

8.3 Results and Discussion

In this chapter we study the variations in ionic conductivity as a function of dopant concentration in NDC and explore the optimal dopant concentration that maximizes the ionic conductivity. As mentioned earlier, researchers have previously studied other systems with similar methodology, but have neglected the Coulomb interactions between the charged va-

cancies. We also investigate the significance of including these effect by using the vacancy repelling (VR) and the vacancy non-repelling (VNR) versions of our code.

The results of the KLMC-VNR model for 0-40% dopant concentrations at temperatures of 673 K, 723 K and 773 K are shown in Fig. 8.1. We also show a representative data in Table 8.2 to show the standard error calculations using Eq. 8.1. We see that for this non-repelling model the ionic conductivity for neodymium doped ceria reaches a maximum between 25%–30%. Now, if we we instead use the vacancy repelling model, the ionic conductivity reaches a maximum at around 17.5% dopant concentration at all temperatures, as can be seen in Fig. 8.2. We have also plotted the log of the conductivity vs. 1/T in Fig. 8.5 that shows that the ionic conductivity rises from 5% dopant concentration to about 17.5% dopant concentration and then decreases as the Nd concentration rises to 40%. The reduction in the dopant concentration needed to reach maximum conductivity is significant. However, we note that the VNR model yields a higher ionic conductivity compared to the VR model. This is because there are fewer number of available sites for the vacancies to migrate on the oxygen sublattice for the VR model due to the vacancy-repelling factor, which decreases the diffusion coefficient.

Table 8.2: Neodymium-doped Ceria—Non-repelling KLMC model at 500 °C.

% Dopant	Number of Runs	Mean Diffusion Coefficient	Standard Error	Mean Ionic Conductivity	Standard Error
0.005	13	5.46e-07	3.27e-09	1.27e-05	7.56e-08
5	13	4.84e-07	2.50e-09	1.12e-03	5.84e-06
10	24	4.17e-07	2.48e-09	1.93e-03	1.15e-05
15	14	3.51e-07	4.79e-09	2.44e-03	3.34e-05
20	6	2.94e-07	6.19e-09	2.73e-03	5.75e-05
25	6	2.42e-07	5.68e-09	2.81e-03	6.58e-05
30	7	1.98e-07	3.59e-09	2.76e-03	5.00e-05
35	8	1.64e-07	2.60e-09	2.67e-03	4.22e-05
40	8	1.41e-07	2.18e-09	2.62e-03	4.06e-05

Our calculated values for a maximum in ionic conductivity for Nd doped ceria at $\sim$ 17.5% dopant concentration is in the range of 15–20% experimental values plotted

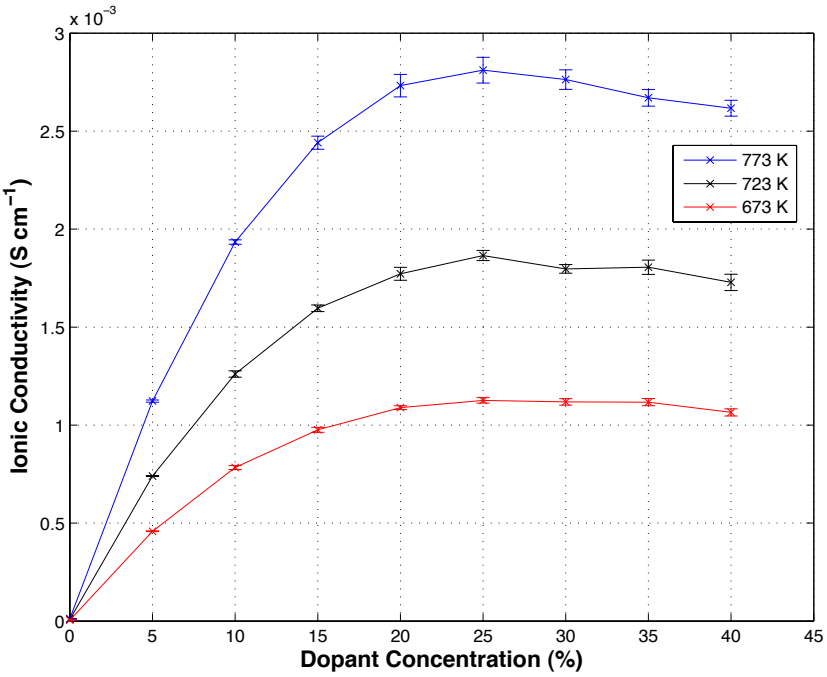

Figure 8.1: Diffusion coefficient for Nd doped ceria vs. dopant concentration for the vacancy non-repelling model. The extent of the error bars as calculated using Eq. 8.1 can clearly be seen as dependent on the number of sampling of each data point as presented in Table 8.2.

by Stephens and Kilner [33] using data from Aneflous et al. [163] (Fig. 8.3, and Fu et al. [164] (Fig. 8.4. As in the other two cases we observe the increase and then decrease in ionic conductivity with increasing dopant concentration. Initially, the ionic conductivity increases at lower dopant concentration due to the increase in vacancy concentration, but after reaching a maximum, it decreases due to increasing interactions between the dopant ions and vacancies that serves as a bottleneck, decreasing the number of minimum energy pathways for a vacancy to diffuse.

Ionic conductivity decreases with increasing dopant concentration because of the increase in average activation energy for vacancy migration and the percent increase of Nd ions near the migrating vacancy. The increasing number of Nd ions often tends to bind the neighboring oxygen vacancy more strongly and decrease the diffusion coefficient, which in turn decreases the oxide ion conductivity. For NDC, the formation of an oxygen vacancy

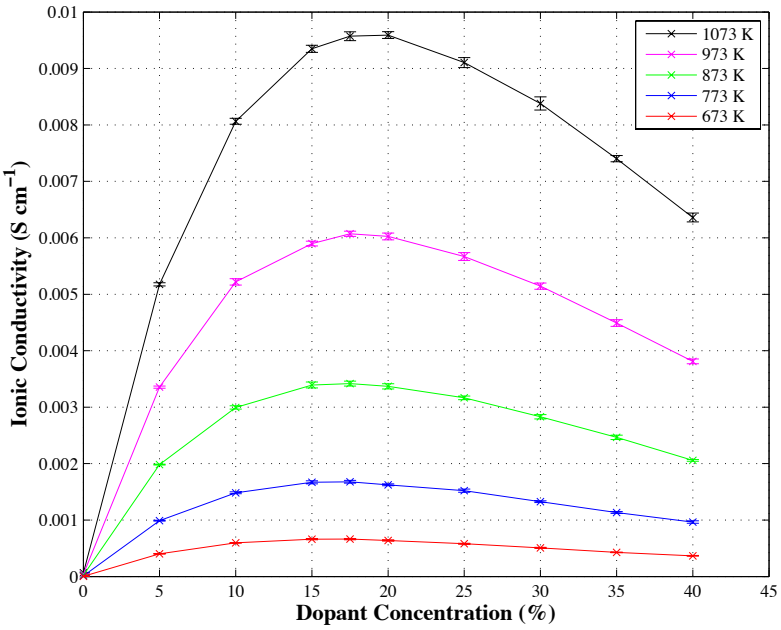

Figure 8.2: Ionic conductivity for Nd doped ceria vs. dopant concentration (vacancy repelling model).

is found to be most favorable at the 1NN as we have pointed out in Chapter 4. However, the difference between $E_{2,1}$ (0.437 eV) and $E_{1,2}$ (0.428 eV) is only 0.009 eV. This value compares well with that reported by Nakayama and Martin [165] ($\sim$ 0.01 eV), using spin-polarization calculations in VASP. For Pr doped ceria this difference is 0.06 eV and for Gd doped ceria it is 0.14 eV. So, while for PDC the 1NN $\rightarrow$ 2NN migration path is more favorable and for GDC the 2NN $\rightarrow$ 1NN migration path is clearly preferred, for Nd doped ceria the preference between the first and second nearest neighbor sites is a little ambiguous. At low dopant concentration, the number of available minimum energy diffusion pathways is higher and as the dopant concentration goes up the available minimum energy pathways decreases leading to lower ionic conductivity. Our results agree well with the few experimental results, therefore we feel that our methodology can serve as a fundamental tool for predicting the optimal dopant concentration in neodymium doped ceria. Our work is also important because, as far we know, no one else has used Monte Carlo simulation to explore the effect of dopant concentration and temperature on the ionic conductivity of NDC.

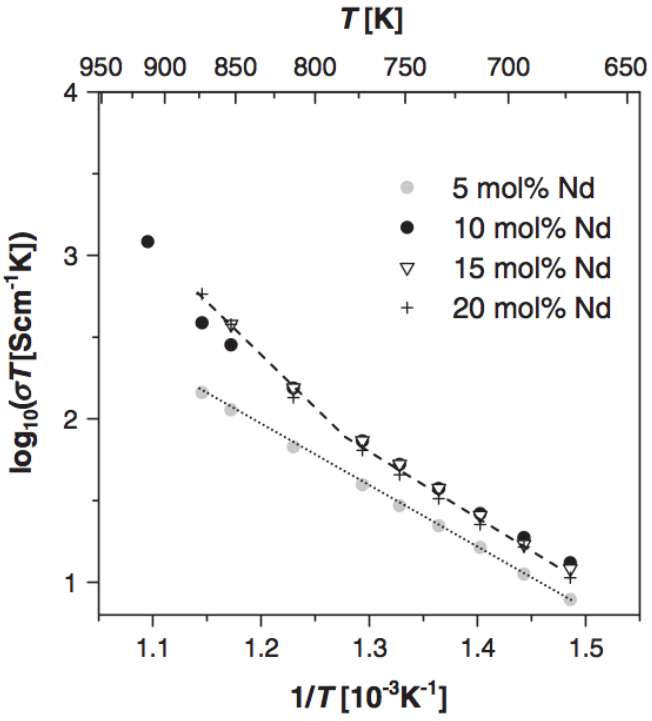

Figure 8.3: Ionic conductivity for Nd doped ceria vs. dopant concentration. Figure from Stephens and Kilner [33] who plotted it with data extracted from Aneflous et al. [163].

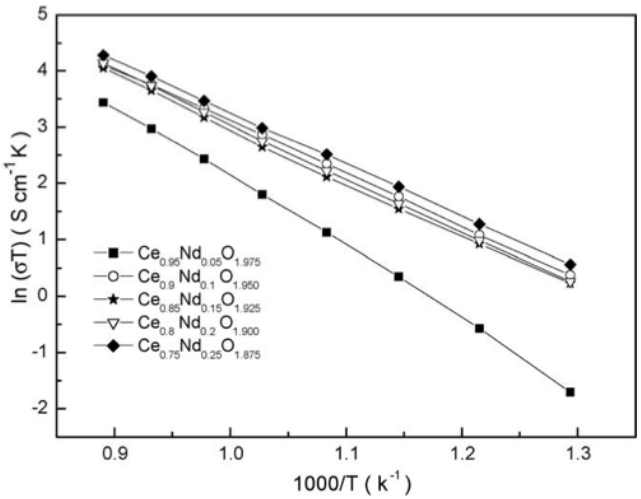

Figure 8.4: Ionic conductivity for Nd doped ceria vs. dopant concentration. Figure from Fu et al. [164].

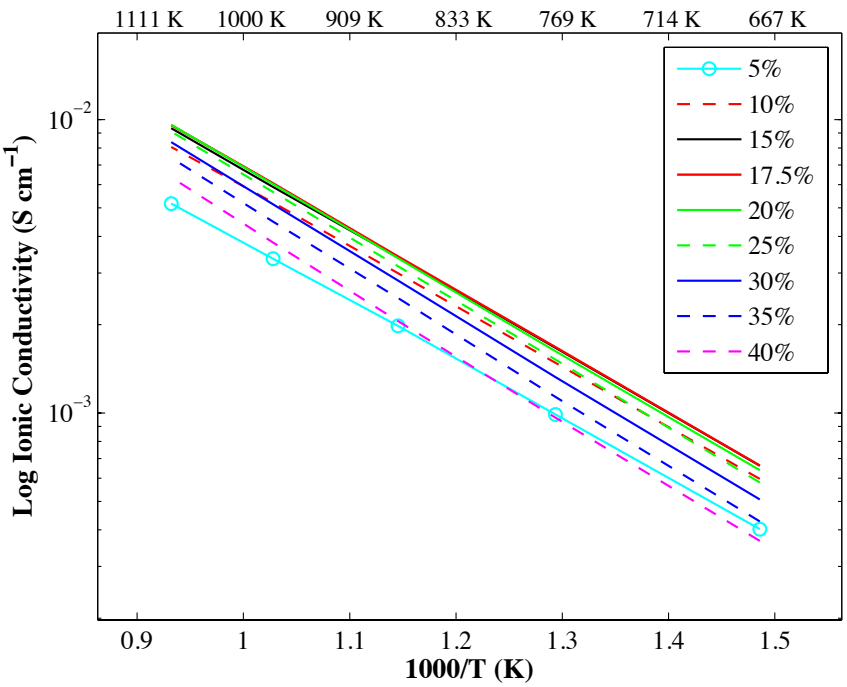

Figure 8.5: Log Ionic conductivity for Nd doped ceria (vacancy repelling model).

It is interesting to compare the ionic conductivities of the three dopants. Fig.8.6 shows the ionic conductivities of Nd, Gd, and Pr calculated by KLMC-VR model at different temperatures. We see that Pr, has the highest ionic conductivity with the maximum near 20% dopant concentration, followed by Nd. However, Nd crests at a slightly lower dopant concentration (17.5%). Gd has similar maximum as Nd, but at a much higher dopant concentration ($\sim\ 25--30\%$) for the VR model. But, we know that running Gd with another model (KLMC-VRDP) gives us a maximum for Gd ionic conductivity for a lower dopant concentration of $\sim 22\%$. We can clearly see that these trends hold at different temperatures. I feel that we can attribute the differences in this plot to the size effect of the ionic radius. Dopant size plays a role in attracting oxygen vacancies and strong associations occur between Ce^{4+} and an oxygen vacancy for large dopants as observed by Nakayama and Martin [165].

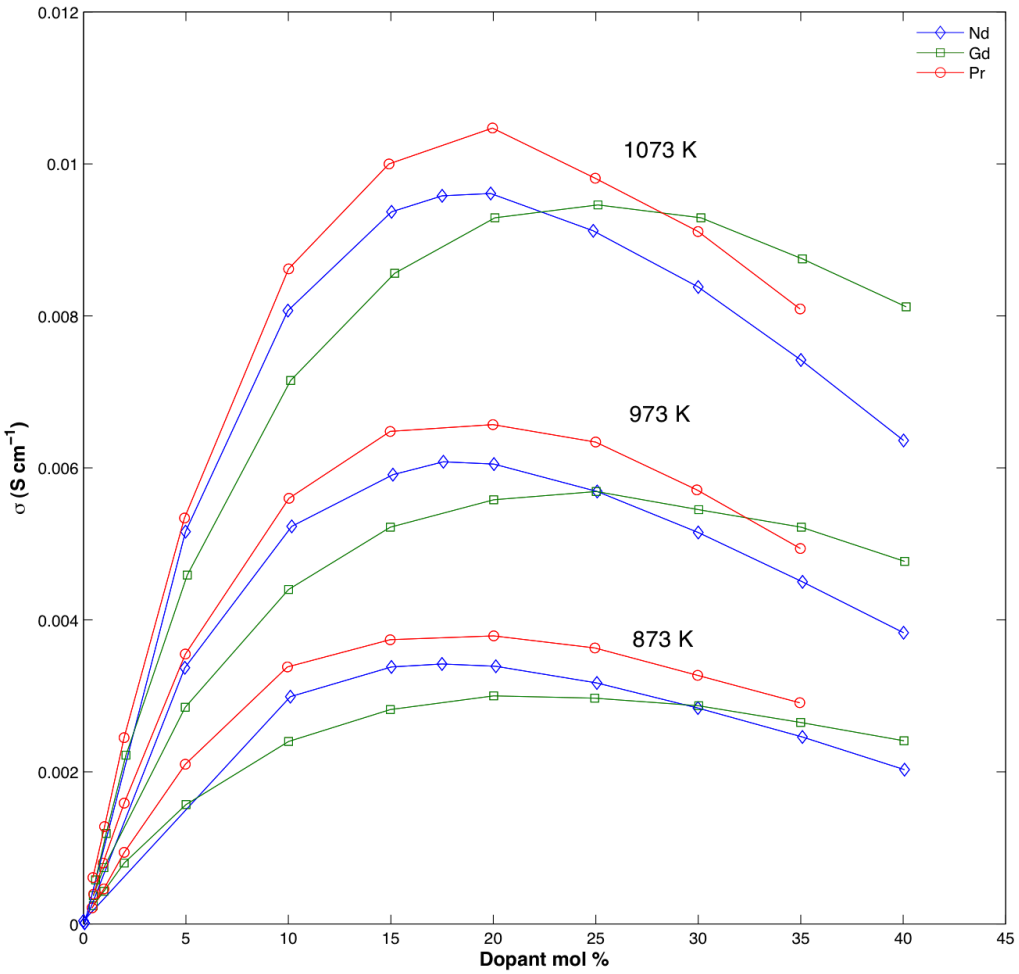

Figure 8.6: Log Ionic conductivity for Nd, Gd, and Pr doped ceria (vacancy repelling model) at three different temperatures (873 K, 973 K, and 1073 K).

8.4 Conclusion

We have simulated vacancy diffusion in neodymium doped ceria (NDC) using the Kinetic Lattice Monte Carlo code that we have developed, using the activation energies calculated using density functional theory, for the vacancy repelling and vacancy non-repelling cases. Our findings are in good agreement with experimental ones. We have not found any simulation results by other to compare against our findings. Compared to our calculations for PDC and GDC we find that NDC reaches a maximum in ionic conductivity at slightly less dopant concentrations.

Chapter 9

CONCLUSIONS

9.1 Summary

In this dissertation work we have conducted a theoretical investigation of the ionic conductivity in doped ceria. Doped ceria is important because it is used as an electrolyte in solid oxide fuel cells (SOFCs). SOFCs have not gained widespread deployment because they need to be operated at high temperatures ($\sim 1000\ ^{\circ}$C). Therefore, one of the goals of this research was to systematically explore how dopant types and dopant concentrations influence the ionic conduction and to understand the mechanisms of diffusion in doped ceria.

Although vigorous efforts are underway to experimentally characterize ionic diffusion and to develop optimal doped ceria electrolytes, experimental studies do not lend to an understanding of the mechanism of ionic conduction at the atomic level. This understanding is important in order to develop better ionic conductors. Therefore,the thrust of this dissertation was to develop a fundamental understanding of oxygen vacancy migration at the atomic level for both doped and pure ceria. In this research we have considered several elements of the lanthanide series (neodymium, praseodymium and gadolinium) as dopants. We have explored the different pathways for oxygen vacancy migration in doped ceria via vacancy hopping mechanisms for varying dopant concentrations and temperatures. Since the introduction of the dopants affects vacancy formation and migration we have investigated the effects on the first three nearest neighbors, having determined that the effects on more distant neighbors are negligible. We have used density functional theory (DFT+U) calculations to calculate the energies and have chosen the *ab initio* total-energy program VASP (Vienna *ab initio* simulation program) to carry out our calculations. To model the diffusion mechanism of the transport of the charge carriers. We have developed a novel random events code, the Kinetic Lattice Monte Carlo (KLMC) program, to carry out simulations of oxygen vacancy diffusion, using the density functional theory (DFT) activation energies as input.

Using DFT and KLMC we can predict optimal design of materials rather than conducting expensive and time consuming trial and error experimental procedures. DFT has also been used by other researchers to find bulk properties of ceria in good agreement with experimental data. Density functional theory (DFT) is also a very good first principles tool for calculating oxygen vacancy formation and migration in doped ceria because it yields results that are better than those employing, say, empirical potentials and aspects of it has been been explored by others.

We have used DFT+U calculations for neodymium doped ceria to investigate oxygen vacancy migration. We have verified the known bulk properties of pure ceria and have calculated the energy barriers along different migration pathways. We have found that the first nearest site to Nd^{3+} is the most favorable for vacancy formation and that the 2NN $\rightarrow$ 1NN to be the most favorable. Our calculations validate experimental results that the inclusion of dopants in pure ceria reduces the activation barrier to vacancy migration—thus diffusion and ionic conductivity is increased. We can expect that adding more dopants would further lower the activation barrier. In order to explore the variation of diffusion (and hence the ionic conductivity) as a function of dopant concentration, and also of the temperature, we have used the activation energies calculated using DFT+U as inputs to the Kinetic Lattice Monte Carlo (KLMC) code that we have developed to study neodymium doped ceria. For praseodymium and gadolinium doped ceria we have used the activation energies calculated by first principles method by Dholabhai et al.

I have co-developed a KLMC code to model oxygen vacancy diffusion in ceria. We have used different versions of the KLMC code in which we either allow vacancies to be placed next to each other (vacancy repelling KLMC (VR model)) or the vacancy non-repelling KLMC (VNR model)).

We have used KLMC simulations using previously published activation energies calculated using density functional theory method to investigate oxygen vacancy diffusion in praseodymium doped ceria (PDC). We have found that a dopant concentration of approximately $\sim 15\%$ to $\sim 20\%$ to be optimal for achieving maximum ionic conductivity in

PDC. The KLMC simulations are in reasonably good agreement with the available experimental data, when we take into account that only about half of the dopants are ionized. The decrease in ionic conductivity with increasing dopant concentration is correlated with the increase in average activation energy for vacancy migration from the vicinity of the dopant pairs and the subsequent decrease in availability of minimum energy pathways for the vacancy diffusion.

We next conducted KLMC simulations to predict the optimal dopant composition for gadolinium doped ceria (GDC) using the activation energies for vacancy migration along distinct diffusion pathways calculated using DFT+U by Dholabhai, et al. Applying the KLMC–VR model for the temperature ranges 673 K to 1073 K, a dopant concentration of $\sim 20\%$ to 25% is found to be optimal for achieving maximum ionic conductivity in GDC. The linear increase in ionic conductivity at low dopant concentration and its gradual decrease at higher dopant concentration after reaching a maxima can be explained by the combined effect of (i) increasing interactions between the dopant ions and vacancies that block further diffusion of vacancies; (ii) fewer sites being available for vacancies to migrate due to the vacancy-repelling effect; and (iii) the increase in average activation energy as a function of the increase in dopant concentration.

We also presented an alternative KLMC–VRDP model, which assumes that all the dopants are placed in Gd$-$Gd pairs. The KLMC–VRDP model results in slightly lower conductivities, and shifts the peak to somewhat lower dopant concentrations. To include the effect of lattice parameter expansion due to dopant addition, we developed a KLMC–VR,X model, which uses the activation energies calculated in an expanded GDC lattice. For 20 mol% GDC, KLMC–VR,X model yields conductivities that are approximately an order of magnitude higher than for the KLMC-VR model. The agreement of the two models with experiment is similar, with the KLMC–VR model having better agreement at lower temperatures, and the KLMC–VR,X model having better agreement at higher temperatures.

For neodymium doped ceria (NDC), we found that an oxygen vacancy was more likely to be formed at the 1NN site. This is similar to the Gd doped case, but contrasts with

the Pr doped case in which the second nearest neighbor was the more favorable site. This has to do with the ionic radii of the dopants as compared with that of the host cerium ions. We have simulated vacancy diffusion in NDC using our Kinetic Lattice Monte Carlo code for both the vacancy repelling and vacancy non-repelling cases, using the activation energies calculated using density functional theory. Our findings are in good agreement with experimental ones and that the vacancy repelling case gives more realistic results. We have not found any simulation results by other to compare against our findings. Compared to our calculations for PDC and GDC we find that NDC reaches a maximum in ionic conductivity at slightly less ($\sim 17.5\%$) dopant concentrations.

Since the KLMC results are in reasonable agreement with experimental measurements, we can assert that the KLMC model in conjunction with first-principles calculations can be used as a design tool to predict the optimal dopant concentration for attaining maximum ionic conductivity in ceria related materials for electrolyte applications.

9.2 Future Work

In the future we plan to expand this work to investigate the effect of some other dopants from the lanthanide series. The large effect of dopant expansion of the lattice on ionic conductivity that we have seen suggests we should explore lattice expansion by the addition of other dopants, and this effect may be an important guide in searching for new dopants for ceria. We also plan to investigate the effect of codopants on ionic conductivity and for creating new electrolyte material for operation at lower temperatures. In this study we have restricted ourselves only to the study of bulk and doped bulk ceria. It would also be interesting to extend our study to those of the surfaces. We could, for example, compute surface energies of Ce_2O_3 for different surface orientations and compute O vs. Ce termination. This can lead to different faceting. We could also study hydrogen adsorption on Ce_2O_3 surfaces by calculating the binding energies and H coverage.It would also be very interesting to investigate cerium and oxygen vacancy diffusion on Ce_2O_3 surfaces. Last, but not least we plan to modularize our KLMC code and place it on the web for others to use and develop a graphical user interface front end.

REFERENCES

[1] Andersson, D. A., Simak, S. I., Skorodumova, N. V., Abrikosov, I. A., and Johansson, B. Optimization of ionic conductivity in doped ceria. *Proceedings of the National Academy of Sciences of the United States of America* **103**(10), 3518–3521, 03 (2006).

[2] Carrette, L., Friedrich, K. A., and Stimming, U. Fuel cells: Principles, types, fuels, and applications. *ChemPhysChem* **1**, 162–193 (2000).

[3] Steele, B. C. H. and Heinzel, A. Materials for fuel-cell technologies. *Nature* **414**(6861), 345–352, 11 (2001).

[4] Steele, B. C. H. Appraisal of $Ce_{1-y}Gd_yO_{2-y/2}$ electrolytes for IT-SOFC operation at 500C. *Solid State Ionics* **129**, 95–110 (2000).

[5] Frayret, C., Villesuzanne, A., Pouchard, M., and Matar, S. Density functional theory calculations on microscopic aspects of oxygen diffusion in ceria-based materials. *International Journal of Quantum Chemistry* **101**, 826–839 (2005).

[6] Trovarelli, A. Catalytic properties of ceria and CeO_2-containing materials. *Catalysis Reviews: Science and Engineering* **38**(4), 439 – 520 (1996).

[7] Dholabhai, P. P., Adams, J. B., Crozier, P., and Sharma, R. A density functional study of defect migration in gadolinium doped ceria. *Physical Chemistry Chemical Physics* **12**(28), 7904–7910 (2010).

[8] Dholabhai, P. P., Adams, J. B., Crozier, P., and Sharma, R. Oxygen vacancy migration in ceria and Pr-doped ceria: A DFT+U study. *Journal of Chemical Physics* **132**(9), 094104 (2010).

[9] Inaba, H. and Tagawa, H. Ceria-based solid electrolytes. *Solid State Ionics* **83**(1-2), 1 – 16 (1996).

[10] Kilner, J. A. and Steele, B. C. H. Physics of electrolytes. Academic Press, New York (1981).

[11] Mogensen, M., Sammes, N. M., and Tompsett, G. A. Physical, chemical and electrochemical properties of pure and doped ceria. *Solid State Ionics* **129**(1-4), 63 – 94 (2000).

[12] Sharma, S., Hilaire, S., Vohs, J. M., Gorte, R. J., and Jen, H. W. Evidence for oxidation of ceria by CO_2. *Journal of Catalysis* **190**(1), 199 – 204 (2000).

[13] Steele, B. C. H. High Conductivity Solid State Ionic Conductors. World Scientific, Singapore (1989).

[14] Trovarelli, A. Structural properties and nonstoichiometric behavior of CeO_2. In Catalysis by Ceria and Related Materials, Trovarelli, A., editor, 15–50. Imperial College Press, London, GBR (2002).

[15] Tuller, H. L. Oxygen ion conduction and structural disorder in conductive oxides. *Journal of Physics and Chemistry of Solids* **55**(12), 1393 – 1404 (1994). Special Symposium in Honor of Professor Arthur S. Nowick.

[16] Jiang, Y., Adams, J. B., and van Schilfgaarde, M. Density-functional calculation of CeO_2 surfaces and prediction of effects of oxygen partial pressure and temperature on stabilities. *Journal of Chemical Physics* **123**(6), 08 (2005).

[17] Sayle, T., Parker, S., and Catlow, C. The role of oxygen vacancies on ceria surfaces in the oxidation of carbon monoxide. *Surface Science* **316**(3), 329 – 336 (1994).

[18] Sayle, T. X. T., Parker, S. C., and Catlow, C. R. A. Surface segregation of metal ions in cerium dioxide. *J. Phys. Chem.* **98**(51), 13625–13630 (1994).

[19] Conesa, J. C. Computer modeling of surfaces and defects on cerium dioxide. *Surface Science* **339**, 337–352 (1995).

[20] Gennard, S., Cor'a, F., and Catlow, C. R. A. Comparison of the bulk and surface properties of ceria and zirconia by ab initio investigations. *J. Phys. Chem. B* **103**, 10158–10170 (1999).

[21] Skorodumova, N. V., Baudin, M., and Hermansson, K. Surface properties of CeO_2 from first principles. *Phys. Rev. B* **69**(7), 075401, Feb (2004).

[22] Yang, Z., Woo, T. K., Baudin, M., and Hermansson, K. Atomic and electronic structure of unreduced and reduced CeO_2 surfaces: A first-principles study. *Journal of Chemical Physics* **120**(16), 7741–7749 (2004).

[23] Herschend, B., Baudin, M., and Hermansson, K. Electronic structure of the CeO_2 (1 1 0) surface oxygen vacancy. *Surface Science* **599**(1-3), 173 – 186 (2005).

[24] Nolan, M., Parker, S. C., and Watson, G. W. The electronic structure of oxygen vacancy defects at the low index surfaces of ceria. *Surface Science* **595**(1-3), 223–232, 12 (2005).

[25] Tuller, H. L. and Nowick, A. S. Doped ceria as a solid oxide electrolyte. *Journal of the Electrochemical Society: Solid State Science and Technology* **122**(2), 255–259, February (1975).

[26] Tuller, H. L. and Nowick, A. S. Small polaron electron transport in reduced CeO_2 single crystals. *Journal of Physics and Chemistry of Solids* **38**(8), 859–867 (1977).

[27] Eguchi, K., Setoguchi, T., Inoue, T., and Arai, H. Electrical properties of ceria-based oxides and their application to solid oxide fuel cells. *Solid State Ionics* **52**(1-3), 165 – 172 (1992).

[28] Takasu, Y., Sugino, T., and Matsuda, Y. Electrical conductivity of praseodymia doped ceria. *Journal of Applied Electrochemistry* **14**(1), 79–81 (1984).

[29] Nauer, M., Ftikos, C., and Steele, B. C. H. An Evaluation of Ce-Pr Oxides and Ce-Pr-Nb Oxides Mixed Conductors for Cathodes of Solid Oxide Fuel Cells: Structure, Thermal Expansion and Electrical Conductivity. *Journal of the European Ceramic Society* **14**, 493–499 (1994).

[30] Shuk, P. and Greenblatt, M. Hydrothermal synthesis and properties of mixed conductors based on $Ce_{1-x}Pr_xO_{2-\delta}$ solid solutions. *Solid State Ionics* **116**(3-4), 217 – 223 (1999).

[31] Catlow, C. R. A. Atomistic mechanisms of ionic transport in fast-ion conductors. *Journal of the Chemical Society, Faraday Transactions* **86**, 1167–1176 (1990).

[32] Boureau, G. and Carniato, S. Apparent discrepancies between thermodynamic data and theoretical calculations of the formation energy of an oxygen vacancy in silica. *Solid State Communications* **98**(6), 485 – 487 (1996).

[33] Stephens, I. E. and Kilner, J. A. Ionic conductivity of $Ce_{1x}Nd_xO_{2-x/2}$. *Solid State Ionics* **177**(7-8), 669 – 676 (2006).

[34] Dell, R. M. and Hooper, A. In Solid Electrolytes, Hagenmuller, P. and Gool, W. V., editors, 291. Academic Press, New York (1978).

[35] Kamiyaa, M., Shimadaa, E., Ikumaa, Y., Komatsua, M., Hanedaa, H., Sameshimaa, S., and Hirata, Y. Oxygen self-diffusion in cerium oxide doped with Nd. *Journal of Materials Research* **16**(01), 179–184 (2001).

[36] Adler, S. B. and Smith, J. W. Effects of long-range forces on oxygen transport in yttria-doped ceria: simulation and theory. *J. Chem. Soc., Faraday Trans.* **89**, 3123–3128 (1993).

[37] Kharton, V. V., Viskup, A. P., Figueiredo, F. M., Naumovich, E. N., Shaulo, A. L., and Marques, F. M. B. Electrochemical properties of pr-doped $Ce(Gd)O_{2\delta}$. *Materials Letters* **53**, 160 (2002).

[38] Steele, B. C. H. and Floyd, J. M. *Proceedings of the British Ceram. Trans.* **72**, 55–76 (1971).

[39] Skorodumova, N. V., Ahuja, R., Simak, S. I., Abrikosov, I. A., Johansson, B., and Lundqvist, B. I. Electronic, bonding, and optical properties of CeO_2 and Ce_2O_3 from first principles. *Phys. Rev. B* **64**(11), 115108, Aug (2001).

[40] Pornprasertsuk, R., Ramanarayanan, P., Musgrave, C. B., and Prinz, F. B. Predicting ionic conductivity of solid oxide fuel cell electrolyte from first principles. *Journal of Applied Physics* **98**(10), 103513 (2005).

[41] Kilner, J. and Brook, R. A study of oxygen ion conductivity in doped non-stoichiometric oxides. *Solid State Ionics* **6**(3), 237 – 252 (1982).

[42] Butler, V., Catlow, C. R. A., Fender, B. E. F., and Harding, J. H. Dopant ion radius and ionic conductivity in cerium dioxide. *Solid State Ionics* **8**(2), 109–113, April (1983).

[43] Andersson, D., Simak, S. I., Johansson, B., Abrikosov, I., and Skorodumova, N. V. Modeling of CeO_2, Ce_2O_3, and CeO_{2-x} in the LDA+U formalism. *Phys. Rev. B* **75**(3), 035109, Jan (2007).

[44] Yang, Z., Luo, G., and Lu, Z. Oxygen vacancy formation energy in Pd-doped ceria: A DFT+U study. *J. Chem Phys.* **127**, 074704, August (2007).

[45] Adams, J. B., Wang, Z., and Li, Y. Modeling Cu thin film growth. *Thin Solid Films* **365**(2), 201 – 210 (2000).

[46] Adams, J. B., Rockett, A., Kieffer, J., Xu, W., Nomura, M., Kilian, K. A., Richards, D. F., and Ramprasad, R. Atomic-level computer simulation. *Journal of Nuclear Materials* **216**, 265 – 274 (1994).

[47] Murray, A., Murch, G., and Catlow, C. A new hybrid scheme of computer simulation based on Hades and Monte Carlo: Application to ionic conductivity in Y^{3+} doped CeO_2. *Solid State Ionics* **18-19**(Part 1), 196 – 202 (1986).

[48] Pornprasertsuk, R., Holme, T., and Prinz, F. B. Kinetic monte carlo simulations of solid oxide fuel cell. *Journal of The Electrochemical Society* **156**(12), B1406–B1416 (2009).

[49] Adler, S. B., Smith, J. W., and Reimer, J. A. Dynamic monte carlo simulation of spin-lattice relaxation of quadrupolar nuclei in solids. oxygen-17 in yttria-doped ceria. *The Journal of Chemical Physics* **98**(9), 7613–7620 (1993).

[50] Krishnamurthy, R., Yoon, Y.-G., Srolovitz, D. J., and Car, R. Oxygen diffusion in yttria-stabilized zirconia: A new simulation model. *Journal of the American Ceramic Society* **87**(10), 1821–1830 (2004).

[51] Meyer, M., Nicoloso, N., and Jaenisch, V. Percolation model for the anomalous conductivity of fluorite-related oxides. *Phys. Rev. B* **56**(10), 5961–5966, Sep (1997).

[52] Efremov, D., Pinaeva, L., Sadykov, V., and Mirodatos, C. Original monte carlo method for analysis of oxygen mobility in complex oxides by simulation of oxygen isotope exchange data. *Solid State Ionics* **179**(21-26), 847 – 850 (2008). Solid State

Ionics 16: Proceedings of the 16th International Conference on Solid State Ionics (SSI-16), Part I.

[53] van de Walle, A. and Ellis, D. E. First-principles thermodynamics of coherent interfaces in samarium-doped ceria nanoscale superlattices. *Phys. Rev. Lett.* **98**(26), 266101, Jun (2007).

[54] Hull, S., Norberg, S., Ahmed, I., Eriksson, S., Marrocchelli, D., and Madden, P. Oxygen vacancy ordering within anion-deficient ceria. *Journal of Solid State Chemistry* **182**(10), 2815 – 2821 (2009).

[55] Hayashi, H., Sagawa, R., Inaba, H., and Kawamura, K. Molecular dynamics calculations on ceria-based solid electrolytes with different radius dopants. *Solid State Ionics* **131**(3-4), 281 – 290 (2000).

[56] Inaba, H., Sagawa, R., Hayashi, H., and Kawamura, K. Molecular dynamics simulation of gadolinia-doped ceria. *Solid State Ionics* **122**(1-4), 95 – 103 (1999).

[57] Schrödinger, E. An undulatory theory of the mechanics of atoms and molecules. *Phys. Rev.* **28**(6), 1049–1070, Dec (1926).

[58] Dirac, P. A. M. Quantum mechanics of many-electron systems. *Proceedings of the Royal Society of London. Series A, Containing Papers of a Mathematical and Physical Character* **123**(792), 714–733, April (1929).

[59] Kohn, W. Nobel lecture: Electronic structure of matter—wave functions and density functionals. *Rev. Mod. Phys.* **71**(5), 1253–1266, October (1999).

[60] Kaxiras, E. *Atomic and Electronic Structure of Solids*. Cambridge University Press, Cambridge, UK, (2003).

[61] Born, M. and Huang, K. *Dynamical Theory of Crystal Lattices*. Oxford University Press, New York, (1985).

[62] Hartree, D. R. The wave mechanics of an atom with non-coulombic central field: parts i, ii, iii. *Proc. Cambridge Phil. Soc.* **24**, 89, 111,426 (1928).

[63] Sholl, D. and Steckel, J. A. *Density Functional Theory : A Practical Introduction*. Wiley, (2009).

[64] Slater, J. C. The theory of complex spectra. *Phys. Rev.*. **34**, 1293 (1929).

[65] Dirac, P. A. M. On the theory of quantum mechanics. *Proceedings of the Royal Society of London. Series A, Containing Papers of a Mathematical and Physical Character* **112**(762), 661–677 (1926).

[66] Martin, R. M. *Electronic Structure: Basic Theory and Practical Methods*. Cambridge University Press, (2004).

[67] Parr, R. G. and Yang, W. *Density-Functional Theory of Atoms and Molecules*. Oxford University Press, New York, (1989).

[68] Sutton, A. P. *Electronics Structure of Materials*. Oxford University Press, New York, (1993).

[69] Hohenberg, P. and Kohn, W. Inhomogeneous electron gas. *Phys. Rev.* **136**(3B), B864–B871, Nov (1964).

[70] Kohn, W. and Sham, L. J. Self-consistent equations including exchange and correlation effects. *Physical Review* **140**(4A), A1133–A1138, Nov (1965).

[71] Levy, M. Universal variational functionals of electron densities, first-order density matrices, and natural spin-orbitals and solution of the v-representability problem. *Proceedings of the National Academy of Sciences of the United States of America* **76**(12), 6062–6065 (1979).

[72] Jones, R. O. and Gunnarsson, O. The density functional formalism, its applications and prospects. *Rev. Mod. Phys.* **61**(3), 689–746, Jul (1989).

[73] Hafner, J. Atomic-scale computational materials science. *Acta Metallurgica* **48**, 71–92 (2000).

[74] Perdew, J., Chevary, J., Vosko, S., Jackson, K., Pederson, M., Singh, D., and Fiolhais, C. Atoms, molecules, solids, and surfaces: Applications of the generalized gradient approximation for exchange and correlation. *Phys. Rev. B* **46**, 6671 (1992).

[75] Perdew, J., Chevary, J., Vosko, S., Jackson, K., Pederson, M., Singh, D., and Fiolhais, C. Erratum: Atoms, molecules, solids, and surfaces: Applications of the generalized gradient approximation for exchange and correlation. *Phys. Rev. B* **48**, 4978 (1993).

[76] Perdew, J. P., Burke, K., and Ernzerhof, M. Generalized gradient approximation made simple. *Phys. Rev. Lett.* **77**(18), 3865–3868, Oct (1996).

[77] Perdew, J. P., Burke, K., and Ernzerhof, M. Erratum: Generalized gradient approximation made simple. *Phys. Rev. Lett.* **78**, 1396 (1997).

[78] Singh, D. J. and Nordstrom, L. *Planewaves, Pseudopotentials and the LAPW Method*. Springer, 2nd edition, (2006). ID: 63435.

[79] Seminario, J. M. An introduction to density functional theory in chemistry. In Modern Density Functional Theory, Seminario, J. M. and Politzer, P., editors, volume 2. Elsevier Science, Amsterdam, The Netherlands (1995).

[80] Becke, A. D. Density-functional thermochemistry. iii. the role of exact exchange. *The Journal of Chemical Physics* **98**(7), 5648–5652 (1993).

[81] Lee, C., Yang, W., and Parr, R. G. Development of the colle-salvetti correlation-energy formula into a functional of the electron density. *Phys. Rev. B* **37**(2), 785–789, Jan (1988).

[82] Baranek, P., Gauthier, L., and Marrony, M. Theoretical study of sulphur interaction with ceria. *AIP Conference Proceedings* **963**(2), 367–370 (2007).

[83] Kullgren, J., Castleton, C. W. M., Muller, C., Ramo, D. M., and Hermansson, K. B3LYP calculations of cerium oxides. *The Journal of Chemical Physics* **132**(5), 054110 (2010).

[84] Dudarev, S. L., Botton, G. A., Savrasov, S. Y., Humphreys, C. J., and Sutton, A. P. Electron-energy-loss spectra and the structural stability of nickel oxide: An LSDA+U study. *Phys. Rev. B* **57**(3), 1505–1509, Jan (1998).

[85] Mosey, N. J. and Carter, E. A. Ab initio evaluation of coulomb and exchange parameters for dft+u calculations. *Phys. Rev. B* **76**, 155123 (2007).

[86] Anisimov, V. I., Aryasetiawan, F., and Lichtenstein, A. I. First-principles calculations of the electronic structure and spectra of strongly correlated systems: the LDA + U method. *Journal of Physics: Condensed Matter* **9**(4), 767 (1997).

[87] Davidson, E. R. and Feller, D. Basis set selection for molecular calculations. *Chemical Reviews* **86**(4), 681–696 (1986).

[88] Leach, A. R. *Molecular Modelling: Principles and Applications*. Addison Wesley Longman Limited, Singapore, (1996).

[89] Helgakar, T. and Taylor, P. R. Gaussian Basis Sets and Molecular Orbitals. In Modern electronic structure theory, Yarkony, D. R., editor, volume 2. World Scientific, River Edge, NJ (1995).

[90] Chong, D. P. Completeness profiles of one-electron basis sets. *Canadian Journal of Chemistry* **73**, 79–83 (1995).

[91] Ashcroft, N. W. and Mermin, N. D. *Solid Steate Physics*. Holt, Rinehart and Wilson, New York, (1976).

[92] Monkhorst, H. J. and Pack, J. D. Special points for brillouin-zone integrations. *Phys. Rev. B* **13**(12), 5188–5192, Jun (1976).

[93] Kittel, C. *Introduction to Solid State Physics*. John Wiley & Sons, Inc., New York, 6th edition, (1986).

[94] Pickett, W. E. Pseudopotential methods in condensed matter applications. *Computer Physics reports* **9**(3), 115 – 197 (1989).

[95] Topp, W. C. and Hopfield, J. J. Chemically motivated pseudopotential for sodium. *Phys. Rev. B* **7**(4), 1295–1303, Feb (1973).

[96] Starkloff, T. and Joannopoulos, J. D. Local pseudopotential theory for transition metals. *Phys. Rev. B* **16**(12), 5212–5215, Dec (1977).

[97] Kilner, J. A. Fast oxygen transport in acceptor doped oxides. *Solid State Ionics* **129**(1-4), 13–23 (2000).

[98] Kilner, J. A. Defects and conductivity in ceria-based oxides. *Chemistry Letters* **37**(10), 1012–1015 (2008).

[99] Tilley, R. J. D. *Defects in Solids*. John Wiley & Sons, Inc., Hoboken, NJ, (2008).

[100] Kröger, F. A. and Vink, H. J. *Solid State Physics* **3**, 310 (1956).

[101] Minervini, L., Zacate, M. O., and Grimes, R. W. Defect cluster formation in M_2O_3-doped CeO_2. *Solid State Ionics* **116**(3-4), 339–349 (1999).

[102] Faber, J., Geoffroy, C., Roux, A., Sylvestre, A., and Abélard, P. A systematic investigation of the DC electrical conductivity of rare-earth doped ceria. *Applied Physics A: Materials Science and Processing* **49**, 225–232 (1989). 10.1007/BF00616848.

[103] Wang, D. Y., Park, D., Griffith, J., and Nowick, A. Oxygen-ion conductivity and defect interactions in yttria-doped ceria. *Solid State Ionics* **2**(2), 95 – 105 (1981).

[104] Kresse, G. and Hafner, J. Ab initio molecular dynamics for liquid metals. *Phys. Rev. B* **47**, 558 (1993).

[105] Kresse, G. and Hafner, J. Ab initio molecular-dynamics simulation of the liquid-metal-amorphous-semiconductor transition in germanium. *Phys. Rev. B* **49**, 14251 (1994).

[106] Kresse, G. and Furthmüller, J. Efficiency of ab-initio total energy calculations for metals and semiconductors using a plane-wave basis set. *Computational Materials Science* **6**(1), 15 – 50 (1996).

[107] Kresse, G. and Furthmüller, J. Efficient iterative schemes for ab initio total-energy calculations using a plane-wave basis set. *Phys. Rev. B* **54**, 11169 (1996).

[108] Kresse, G. and Hafner, J. Norm-conserving and ultrasoft pseudopotentials for first-row and transition-elements. *J. Phys.: Condens. Matter* **6**, 8245 (1994).

[109] Yang, Z., Woo, T. K., and Hermansson, K. Effects of zr doping on stoichiometric and reduced ceria: A first-principles study. *Journal of Physical Chemistry* **124**, 224704 (2006).

[110] Sevik, C. and Cagin, T. Mechanical and electronic properties of CeO_2, ThO_2, and (ce,th)O_2 alloys. *Phys. Rev. B* **80**(1), 014108 (2009).

[111] Nolan, M., Grigoleit, S., Sayle, D. C., Parker, S. C., and Watson, G. W. Density functional theory studies of the structure and electronic structure of pure and defective low index surfaces of ceria. *Surface Science* **576**(1-3), 217 – 229 (2005).

[112] Jiang, Y., Adams, J. B., and van Schilfgaarde, M. Theoretical study of environmental dependence of oxygen vacancy formation in CeO_2. *Applied Physics Letters* **87**, 141917 (2005).

[113] Fabris, S., de Gironcoli, S., Baroni, S., and Balducci, G. Taming multiple valency with density functionals: A case study of defective ceria. *Phys. Rev. B* **71**, 041102 (2005).

[114] Fabris, S., de Gironcoli, S., and Baroni, S. Reply to "comment on 'taming multiple valency with density functionals: A case study of defective ceria' ". *Phys. Rev. B* **72**, 237102 (2005).

[115] Yang, Z., Wei, Y., Fu, Z., Lu, Z., and Hermansson, K. Facilitated vacancy formation at Zr-doped ceria(1 1 1) surfaces. *Surface Science* **602**(6), 1199 – 1206 (2008).

[116] Da Silva, J. L. F., Ganduglia-Pirovano, M. V., Sauer, J., Bayer, V., and Kresse, G. Hybrid functionals applied to rare-earth oxides: The example of ceria. *Phys. Rev. B* **75**(4), 045121, Jan (2007).

[117] Loschen, C., Carrasco, J., Neyman, K. M., and Illas, F. First-principles $lda+u$ and $gga+u$ study of cerium oxides: Dependence on the effective u parameter. *Phys. Rev. B* **75**(3), 035115, Jan (2007).

[118] Kresse, G., Blaha, P., Da Silva, J. L. F., and Ganduglia-Pirovano, M. V. Comment on "taming multiple valency with density functionals: A case study of defective ceria". *Phys. Rev. B* **72**(23), 237101, Dec (2005).

[119] Castleton, C. W. M., Kullgren, J., and Hermansson, K. Tuning lda + u for electron localization and structure at oxygen vacancies in ceria. *The Journal of Chemical Physics* **127**(24), 244704 (2007).

[120] Henkelman, G., Arnaldsson, A., and Jönsson, H. A fast and robust algorithm for bader decomposition of charge density. *Computational Materials Science* **36**(3), 354 – 360 (2006).

[121] Yang, Z., Luo, G., Lu, Z., Woo, T. K., and Hermansson, K. Structural and electronic properties of NM-doped ceria (NM = Pt, Rh): a first-principles study. *J. Phys.: Condens. Matter* **20**, 035210, December (2008).

[122] Nolan, M., Verdugo, V. S., and Metiu, H. Vacancy formation and co adsorption on gold-doped ceria surfaces. *Surface Science* **602**(16), 2734 – 2742 (2008).

[123] Wilson, E. L., Grau-Crespo, R., Pang, C. L., Cabailh, G., Chen, Q., Purton, J. A., Catlow, C. R. A., Brown, W. A., de Leeuw, N. H., and Thornton, G. Redox behavior of the model catalyst Pd/CeO_{2x}/Pt(111). *The Journal of Physical Chemistry C* **112**(29), 10918–10922 (2008).

[124] Blöchl, P. E., Jepsen, O., and Andersen, O. K. Improved tetrahedron method for Brillouin-zone integrations. *Phys. Rev. B* **49**, 16223 (1994).

[125] Kresse, G. and Joubert, D. From ultrasoft pseudopotentials to the projector augmented-wave method. *Phys. Rev. B* **59**(3), 1758–1775, Jan (1999).

[126] Johnson, D. D. Modified broyden's method for accelerating convergence in self-consistent calculations. *Phys. Rev. B* **38**(18), 12807–12813, Dec (1988).

[127] Broyden, C. G. A class of methods for solving nonlinear simultaneous equations. *Mathematics of Computation* **19**, 577–593 (1965).

[128] Hellman, H. *An Introduction to Quantum Chemistry*. Deuticke, Leipzig, (1937).

[129] Feynman, R. P. Forces in molecules. *Phys. Rev.* **56**(4), 340–343, Aug (1939).

[130] Eyring, L. In Handbook on the Physics and Chemistry of Rare Earths, Gschneider, K. A. and Eyring, L., editors, volume 3, 27. North-Holland, Amsterdam (1979).

[131] Gerward, L., Olsen, J. S., Petit, L., Vaitheeswaran, G., Kanchana, V., and Svane, A. Bulk modulus of CeO_2 and PrO_2–an experimental and theoretical study. *Journal of Alloys and Compounds* **400**(1-2), 56 – 61 (2005).

[132] Hill, S. and Catlow, C. A hartree-fock periodic study of bulk ceria. *Journal of Physics and Chemistry of Solids* **54**(4), 411 – 419 (1993).

[133] Payne, M. C., Teter, M. P., Allan, D. C., Arias, T. A., and Joannopoulos, J. D. Iterative minimization techniques for ab initio total-energy calculations: molecular dynamics and conjugate gradients. *Rev. Mod. Phys.* **64**(4), 1045–1097, Oct (1992).

[134] Skorodumova, N. V., Simak, S. I., Lundqvist, B. I., Abrikosov, I. A., and Johansson, B. Quantum origin of the oxygen storage capability of ceria. *Phys. Rev. Lett.* **89**(16), 166601, Sep (2002).

[135] Balducci, G., Kaspar, J., Fornasiero, P., Graziani, M., Islam, M. S., and Gale, J. D. Computer simulation studies of bulk reduction and oxygen migration in CeO_2-ZrO_2 solid solutions. *J. Phys. Chem. B* **101**(10), 1750–1753 (1997).

[136] Bulgakov, N. N., Sadykov, V. A., Lunin, V. V., and Kemmitz, E. Lattice defects and oxygen absorption/migration in ceria/ceria-zirconia solid solutions: Analysis by semiempirical interacting bonds method. *React. Kinet. Catal. Lett.* **76**(1), 103–110 (2002).

[137] Nolan, M., Fearon, J. E., and Watson, G. W. Oxygen vacancy formation and migration in ceria. *Solid State Ionics* **177**(35-36), 3069 – 3074 (2006). Proceedings of the E-MRS Symposium P on Solid State Ionics: Mass and Charge Transport at Various Length Scales.

[138] Cotton, S. *Lanthanide and actinide chemistry*. John Wiley & Sons, Inc., (2006).

[139] Wang, Z., Li, Y., and Adams, J. B. Kinetic lattice Monte Carlo simulation of facet growth rate. *Surface Science* **450**(1-2), 51 – 63 (2000).

[140] Metropolis, N. and Ulam, S. The Monte Carlo method. *Journal of the American Statistical Association* **44**(247), 335–341, September (1949).

[141] El-Mellouhi, F., Mousseau, N., and Ordejón, P. Sampling the diffusion paths of a neutral vacancy in silicon with quantum mechanical calculations. *Phys. Rev. B* **70**(20), 205202, Nov (2004).

[142] Vineyard, G. H. Frequency factors and isotope effects in solid state rate processes. *Journal of Physics & Chemistry of Solids* **3**, 121–127 (1957).

[143] Chen, H.-T., Chang, J.-G., Chen, H.-L., and Ju, S.-P. Identifying the O_2 diffusion and reduction mechanisms on CeO_2 electrolyte in solid oxide fuel cells: A DFT + U study. *Journal of Computational Chemistry* **30**(15), 2433–2442 (2009).

[144] Inaba, H. and Naito, K. Simultaneous measurements of oxygen pressure, composition, and electrical conductivity of praseodymium oxides: I. Pr_7O_{12} and Pr_9O_{16} phases. *Journal of Solid State Chemistry* **50**(1), 100 – 110 (1983).

[145] Huang, W., Shuk, P., and Greenblatt, M. Hydrothermal synthesis and properties of $Ce_{1-x}Sm_xO_{2-x/2}$ and $Ce_{1-x}Ca_xO_{2-x}$ solid solutions. *Chemistry of Materials* **9**(10), 2240–2245 (1997).

[146] Chen, M.-J., Cheng, S., Wang, F.-Y., Lee, J. F., and Tai, Y. L. Study of Pr-doped ceria-based electrolytes for IT-SOFC. *ECS Transactions* **7**(1), 2245–2252 (2007).

[147] Dholabhai, P. P., Anwar, S., Adams, J. B., Crozier, P., and Sharma, R. Kinetic lattice Monte Carlo model for oxygen vacancy diffusion in praseodymium doped ceria: Applications to materials design. *Journal of Solid State Chemistry* **184**, 811–817 (2011).

[148] Chourashiya, M., Patil, J., Pawar, S., and Jadhav, L. Studies on structural, morphological and electrical properties of $Ce_{1-x}Gd_xO_{2-(x/2)}$. *Materials Chemistry and Physics* **109**(1), 39 – 44 (2008).

[149] Zha, S., Xia, C., and Meng, G. Effect of Gd (Sm) doping on properties of ceria electrolyte for solid oxide fuel cells. *Journal of Power Sources* **115**(1), 44 – 48 (2003).

[150] Wang, F.-Y., Wan, B.-Z., and Cheng, S. Study on Gd^{3+} and Sm^{3+} co-doped ceria-based electrolytes. *Journal of Solid State Electrochemistry* **9**, 168–173 (2005).

[151] Guan, X., Zhou, H., Liu, Z., Wang, Y., and Zhang, J. High performance Gd^{3+} and Y^{3+} co-doped ceria-based electrolytes for intermediate temperature solid oxide fuel cells. *Materials Research Bulletin* **43**(4), 1046 – 1054 (2008).

[152] Ivanov, V., Khrustov, V., Kotov, Y., Medvedev, A., Murzakaev, A., Shkerin, S., and Nikonov, A. Conductivity and structure features of $Ce_{1-x}Gd_xO_{2-\delta}$ solid electrolytes fabricated by compaction and sintering of weakly agglomerated nanopowders. *Journal of the European Ceramic Society* **27**(2-3), 1041 – 1046 (2007).

[153] Kudo, T. and Obayashi, H. Mixed electrical conduction in the fluorite-type $Ce_{1-x}Gd_xO_{2-x/2}$. *Journal of The Electrochemical Society* **123**(3), 415–419 (1976).

[154] Peng, C. and Zhang, Z. Nitrate-citrate combustion synthesis of $Ce_{1-x}Gd_xO_{2-x/2}$ powder and its characterization. *Ceramics International* **33**(6), 1133 – 1136 (2007).

[155] Tianshu, Z., Hing, P., Huang, H., and Kilner, J. Ionic conductivity in the $CeO_2-Gd_2O_3$ system (0.05 <=Gd/Ce<= 0.4) prepared by oxalate coprecipitation. *Solid State Ionics* **148**(3-4), 567 – 573 (2002).

[156] Zhang, T. S., Ma, J., Kong, L. B., Chan, S. H., and Kilner, J. A. Aging behavior and ionic conductivity of ceria-based ceramics: a comparative study. *Solid State Ionics* **170**(3-4), 209 – 217 (2004).

[157] Fu, Y.-P., Chang, Y.-S., and Wen, S.-B. Microwave-induced combustion synthesis and electrical conductivity of $Ce_{1-x}Gd_xO_{2-1/2x}$ ceramics. *Materials Research Bulletin* **41**(12), 2260 – 2267 (2006).

[158] van Dijk, T. and Burggraaf, A. J. Grain boundary effects on ionic conductivity in ceramic $Gd_xZr_{1-x}O_{2-(x/2)}$ solid solutions. *physica status solidi (a)* **63**(1), 229–240 (1981).

[159] Gerhardt, R. and Nowick, A. S. Grain-boundary effect in ceria doped with trivalent cations: I, electrical measurements. *Journal of the American Ceramic Society* **69**(9), 641–646 (1986).

[160] Zhang, T., Ma, J., Cheng, H., and Chan, S. Ionic conductivity of high-purity gd-doped ceria solid solutions. *Materials Research Bulletin* **41**(3), 563 – 568 (2006).

[161] Hayashi, H., Kanoh, M., Quan, C. J., Inaba, H., Wang, S., Dokiya, M., and Tagawa, H. Thermal expansion of gd-doped ceria and reduced ceria. *Solid State Ionics* **132**(3-4), 227 – 233 (2000).

[162] Luo, J., Ball, R. J., and Stevens, R. Gadolinia doped ceria/yttria stabilised zirconia electrolytes for solid oxide fuel cell applications. *Journal of Materials Science* **39**, 235–240 (2004). 10.1023/B:JMSC.0000007749.72739.bb.

[163] Aneflous, L., Musso, J. A., Villain, S., Gavarri, J.-R., and Benyaich, H. Effects of temperature and nd composition on non-linear transport properties in substituted ce1-xndxo2-[delta] cerium dioxides. *Journal of Solid State Chemistry* **177**(3), 856 – 865 (2004).

[164] Fu, Y.-P. and Chen, S.-H. Preparation and characterization of neodymium-doped ceria electrolyte materials for solid oxide fuel cells. *Ceramics International* **36**(2), 483 – 490 (2010).

[165] Nakayama, M. and Martin, M. First-principles study on defect chemistry and migration of oxide ions in ceria doped with rare-earth cations. *Physical Chemistry Chemical Physics* **11**(17), 3241–3249 (2009).

Appendix A

POSCAR FILE FOR $1 \times 1 \times 1$ SUPERCELL FOR PURE CERIA

! This is the $1 \times 1 \times 1$ POSCAR file consisting of 4 cerium and 8 oxygen atoms used to calculate the bulk properties of pure ceria.

```
1 fcc CeO2 supercell
2 5.49
3 1.0 0.0 0.0
4 0.0 1.0 0.0
5 0.0 0.0 1.0
6 4 8
7 direct
8 0.5000  0.5000  0.0000
9 0.5000  0.0000  0.5000
10 0.0000  0.5000  0.5000
11 0.0000  0.0000  0.0000
12 0.7500  0.2500  0.7500
13 0.2500  0.2500  0.7500
14 0.2500  0.7500  0.2500
15 0.7500  0.7500  0.7500
16 0.7500  0.2500  0.2500
17 0.2500  0.2500  0.2500
18 0.2500  0.7500  0.7500
19 0.7500  0.7500  0.2500
```

Appendix B

POSCAR FILE FOR $2 \times 2 \times 2$ SUPERCELL FOR PURE CERIA

! This is the $2 \times 2 \times 2$ POSCAR file consisting of 32 cerium and 64 oxygen atoms used to calculate the bulk properties of pure ceria. This is modified by introducing dopants and vacancies to simulate doped ceria.

```
 1 fcc CeO2 supercell
 2 5.494
 3 2.0 0.0 0.0
 4 0.0 2.0 0.0
 5 0.0 0.0 2.0
 6 32 64
 7 direct
 8 0.0000 0.0000 0.0000
 9 0.0000 0.0000 0.5000
10 0.0000 0.5000 0.0000
11 0.0000 0.5000 0.5000
12 0.5000 0.0000 0.0000
13 0.5000 0.0000 0.5000
14 0.5000 0.5000 0.0000
15 0.5000 0.5000 0.5000
16 0.0000 0.2500 0.2500
17 0.0000 0.2500 0.7500
18 0.0000 0.7500 0.2500
19 0.0000 0.7500 0.7500
20 0.5000 0.2500 0.2500
21 0.5000 0.2500 0.7500
22 0.5000 0.7500 0.2500
23 0.5000 0.7500 0.7500
24 0.2500 0.2500 0.0000
25 0.2500 0.2500 0.5000
26 0.2500 0.7500 0.0000
27 0.2500 0.7500 0.5000
28 0.7500 0.2500 0.0000
29 0.7500 0.2500 0.5000
30 0.7500 0.7500 0.0000
31 0.7500 0.7500 0.5000
32 0.2500 0.0000 0.2500
33 0.2500 0.0000 0.7500
34 0.2500 0.5000 0.2500
35 0.2500 0.5000 0.7500
36 0.7500 0.0000 0.2500
37 0.7500 0.0000 0.7500
38 0.7500 0.5000 0.2500
39 0.7500 0.5000 0.7500
40 0.1250 0.1250 0.1250
41 0.1250 0.1250 0.6250
42 0.1250 0.6250 0.1250
```

```
43 0.1250 0.6250 0.6250
44 0.6250 0.1250 0.1250
45 0.6250 0.1250 0.6250
46 0.6250 0.6250 0.1250
47 0.6250 0.6250 0.6250
48 0.1250 0.3750 0.3750
49 0.1250 0.3750 0.8750
50 0.1250 0.8750 0.3750
51 0.1250 0.8750 0.8750
52 0.6250 0.3750 0.3750
53 0.6250 0.3750 0.8750
54 0.6250 0.8750 0.3750
55 0.6250 0.8750 0.8750
56 0.3750 0.3750 0.1250
57 0.3750 0.3750 0.6250
58 0.3750 0.8750 0.1250
59 0.3750 0.8750 0.6250
60 0.8750 0.3750 0.1250
61 0.8750 0.3750 0.6250
62 0.8750 0.8750 0.1250
63 0.8750 0.8750 0.6250
64 0.3750 0.1250 0.3750
65 0.3750 0.1250 0.8750
66 0.3750 0.6250 0.3750
67 0.3750 0.6250 0.8750
68 0.8750 0.1250 0.3750
69 0.8750 0.1250 0.8750
70 0.8750 0.6250 0.3750
71 0.8750 0.6250 0.8750
72 0.1250 0.1250 0.3750
73 0.1250 0.1250 0.8750
74 0.1250 0.6250 0.3750
75 0.1250 0.6250 0.8750
76 0.6250 0.1250 0.3750
77 0.6250 0.1250 0.8750
78 0.6250 0.6250 0.3750
79 0.6250 0.6250 0.8750
80 0.1250 0.3750 0.1250
81 0.1250 0.3750 0.6250
82 0.1250 0.8750 0.1250
83 0.1250 0.8750 0.6250
84 0.6250 0.3750 0.1250
85 0.6250 0.3750 0.6250
86 0.6250 0.8750 0.1250
87 0.6250 0.8750 0.6250
88 0.3750 0.3750 0.3750
89 0.3750 0.3750 0.8750
```

```
 90 0.3750 0.8750 0.3750
 91 0.3750 0.8750 0.8750
 92 0.8750 0.3750 0.3750
 93 0.8750 0.3750 0.8750
 94 0.8750 0.8750 0.3750
 95 0.8750 0.8750 0.8750
 96 0.3750 0.1250 0.1250
 97 0.3750 0.1250 0.6250
 98 0.3750 0.6250 0.1250
 99 0.3750 0.6250 0.6250
100 0.8750 0.1250 0.1250
101 0.8750 0.1250 0.6250
102 0.8750 0.6250 0.1250
103 0.8750 0.6250 0.6250
```

Appendix C

INCAR FILE FOR PURE CERIA

! This is the INCAR file used to calculate the bulk properties of pure ceria and for carrying out the simulations for neodymium doped ceria.

```
 1 SYSTEM = fcc CeO2
 2 ISTART = 0     # job: 0=new
 3 ICHARG = 2     # construct initial charge density with
                  # superposition of atomic charge densities
 4  GGA = PE      # xc-type: PE=Perdew-Burke-Ernzerhof
 5  IALGO = 38    # integer selecting algorithm:  38 (Kosugi)
 6  NSW = 50      # Ionic relaxation; number of steps for
                  # ionic update
 7  IBRION = 1    # Ionic relaxation; 0=MD, 1=quasi-NEW, 2=CG
 8  POTIM = 0.1   # time-step for ion-motion (fs)
 9  ENCUT = 400   # kinetic energy cutoff in eV for
                  # augmented charges
                  # (default from POTCAR file)
10  ISPIN = 2     # spin polarized calculation (2=yes, 1=no)
11
12  LDAU = .TRUE.  # Switches on the L(S)DA+U
13  LDAUTYPE = 2   # Dudarev's approach to LSDA+U
14  LDAUL = 3 -1   # l-quantum # for which the on site interaction
                   # is added. Must specify for all atomic species
15  LDAUU = 6.0 0.0 0.0  # effective on site
                         # Coulomb interaction parameter
16  LDAUJ = 1.0 0.0 0.0  # effective on site
                         #  Exchange interaction parameter
17  LMAXMIX = 6
18  LORBIT = 10
19
20 ISMEAR = 0    # DOS related; method to determine
                 # partial occupancies:
                 # -5=Blochl, -4=tet, -1=fermi, 0=gaus
21 SIGMA = 0.1   # DOS related value; broadening in eV
22 LWAVE = .FALSE.  # LWAVE = .TRUE. generates the WAVECAR file
```

This LaTeX document was generated using the Graduate College Format Advising tool. Please turn a copy of this page in when you submit your document to Graduate College format advising. You may discard this page once you have printed your final document. DO NOT TURN THIS PAGE IN WITH YOUR FINAL DOCUMENT!